

ALMA MATER STUDIORUM · UNIVERSITÀ DI BOLOGNA

---

Scuola di Scienze  
Dipartimento di Fisica e Astronomia  
Corso di Laurea Magistrale in Fisica

# Graph-based analysis of brain structural MRI data in Multiple System Atrophy

**Relatore:**  
Dott.ssa Claudia Testa

**Presentata da:**  
Riccardo Gubellini

**Correlatore:**  
Prof.ssa Paola Fantazzini

Anno Accademico 2015/2016



*Ai miei genitori*



## Abstract

Il lavoro che ho sviluppato presso l'unità di RM funzionale del Policlinico S.Orsola-Malpighi, DIBINEM, è incentrato sull'analisi dei dati strutturali di risonanza magnetica mediante l'utilizzo della graph theory, con lo scopo di valutare eventuali differenze tra un campione di pazienti affetti da Atrofia Multi Sistemica (MSA) e uno di controlli sani (HC).

L'MSA è una patologia neurodegenerativa sporadica e progressiva caratterizzata da disturbi del movimento e dalla disfunzione del sistema nervoso vegetativo. Essa si divide in due sottotipi: MSA-P in cui predominano sintomi parkinsoniani ed MSA-C caratterizzata da deficit cerebellari. Circa un terzo delle persone affette da MSA sperimentano una particolare apnea respiratoria, chiamata Stridor. Questo sintomo può essere particolarmente pericoloso e portare anche alla morte. Nello studio sono stati confrontati tra loro tre coppie di gruppi: HC vs MSA, No-stridor vs Stridor, e MSA-C vs MSA-P.

I grafi sono strutture matematiche definite da nodi e links, che trovano applicazioni in molte discipline diverse tra loro. In campo neurologico, a scopo di ricerca, la graph theory è stata recentemente applicata a dati di functional Magnetic Resonance Imaging (fMRI) e Diffusion Weighted Imaging (DWI) con lo scopo di comprendere il funzionamento del cervello visto come network. I network così costruiti fanno riferimento alla connettività strutturale (DWI) e funzionale (fMRI). Un altro tipo di approccio è quello di considerare un nuovo tipo di connettività, bastato su misure di correlazione anatomiche come la Cortical Thickness, oppure, come per questa tesi, su misure di correlazione volumetriche tra le diverse regioni del cervello.

Per poter costruire un grafo per ogni gruppo il primo step è stato ottenere la parcellizzazione delle immagini strutturali cerebrali, successivamente quello di valutare i volumi delle regioni cerebrali, e in seguito le correlazioni tra esse. Una volta costruiti i grafi è stato possibile calcolare i parametri topologici, globali e locali, che ne caratterizzano struttura ed organizzazione. Nei vari confronti fatti fra gruppi non sono state riscontrate differenze nelle proprietà globali del network. L'analisi regionale invece ha evidenziato un'alterazione del gruppo dei pazienti affetti da MSA rispetto agli HC relativa a regioni che appartengono al network centrale autonomico, particolarmente colpito dalla malattia. Un'alterazione analoga, riguardante specificatamente le misure di Node Betweenness e Node Degree, è stata trovata anche nel confronto fra i soggetti affetti e non affetti da stridor. Sono state inoltre riscontrate alterazioni nella organizzazione modulare dei gruppi presi in esame. E' stata mostrata infatti una segregazione nel network motorio cortico-subcorticale nel gruppo di pazienti MSA rispetto agli HC (senza differenza fra i sottotipi C e P), in linea con la patologia.

Questa analisi ha mostrato la possibilità di indagare la funzionalità dei network cerebrali e della loro architettura modulare con misure strutturali quali la covarianza dei volumi delle varie regioni cerebrali in gruppi di soggetti.



# Contents

<b>1</b>	<b>Magnetic resonance</b>	<b>9</b>
1.1	Theory of nuclear magnetic resonance . . . . .	9
1.2	Spin-echo sequence . . . . .	11
1.3	Relaxation times . . . . .	13
1.4	Spatial position: K-space encoding . . . . .	14
1.5	Gradient echo sequences . . . . .	15
1.5.1	Fast Spoiled Gradient Recalled Echo (FSGRE) . . . . .	17
<b>2</b>	<b>Multiple System Atrophy</b>	<b>18</b>
2.1	Historical background . . . . .	18
2.2	Epidemiology . . . . .	19
2.3	Clinical characteristics . . . . .	19
2.4	Motor involvement . . . . .	19
2.5	Sleep and breathing disorders (Stridor) . . . . .	20
2.6	Cognitive function . . . . .	20
2.7	Pathology and pathogenesis . . . . .	20
2.8	Neuroimaging . . . . .	21
2.9	Diagnostic criteria . . . . .	22
2.10	Neuroimaging criteria . . . . .	22
<b>3</b>	<b>Graph theory</b>	<b>24</b>
3.1	History of graph theory . . . . .	24
3.2	Definitions . . . . .	26
3.2.1	The nature of links . . . . .	26
3.2.2	Multiplicity of links . . . . .	27
3.2.3	Weighted/unweighted graph . . . . .	27
3.3	Applications . . . . .	28
3.3.1	Complex brain networks . . . . .	29
3.4	How to construct a brain graph . . . . .	30
3.4.1	Nodes and links decisions . . . . .	31
3.4.2	Correlations and adjacency matrices . . . . .	31
3.5	Measures . . . . .	31
3.5.1	Node degree and degree distribution . . . . .	32
3.5.2	Shortest path length . . . . .	32

3.5.3	Connected components . . . . .	32
3.5.4	Clustering coefficient . . . . .	33
3.5.5	Path length and Efficiency . . . . .	33
3.5.6	Hubs, centrality and robustness . . . . .	34
3.5.7	Modularity . . . . .	34
3.5.8	Random, scale-free and small-world networks . . . . .	35
<b>4</b>	<b>Materials and methods</b>	<b>37</b>
4.1	Participants . . . . .	37
4.2	MRI data acquisition . . . . .	38
4.3	Data pre-processing . . . . .	38
4.3.1	Brain Extraction Tool (BET) . . . . .	39
4.3.2	Lesion Filling (LF) . . . . .	41
4.3.3	Freesurfer . . . . .	41
4.3.4	Brainstem regions . . . . .	42
4.4	Construction of structural correlation network . . . . .	43
4.4.1	Node decision . . . . .	43
4.4.2	Volume of ROIs . . . . .	47
4.4.3	Definitions of correlations matrices . . . . .	47
4.4.4	Thresholding and Adjacency Matrices . . . . .	48
4.5	Data analysis . . . . .	49
4.5.1	Network analysis . . . . .	49
4.5.2	Statistical analysis . . . . .	50
4.5.2.1	Clinical data . . . . .	50
4.5.2.2	Comparison of correlations matrices between groups	50
4.5.2.3	Comparison of network measures between groups	51
4.6	Network visualization . . . . .	52
<b>5</b>	<b>Results</b>	<b>53</b>
5.1	Clinical variability . . . . .	53
5.2	Comparison of correlations matrices between groups . . . . .	54
5.2.1	Correlation analysis . . . . .	54
5.2.2	False discovery rate matrices . . . . .	63
5.2.3	Z-Statistic . . . . .	67
5.3	Topological parameters and group analysis . . . . .	67
5.3.1	Connected components . . . . .	67
5.3.2	Comparison between groups across density . . . . .	71
5.3.2.1	Healthy controls vs MSA . . . . .	71
5.3.2.2	No-stridor vs Stridor . . . . .	80
5.3.2.3	MSA-C vs MSA-P . . . . .	89
5.3.3	Regional analysis . . . . .	98
5.3.3.1	Healthy controls vs MSA . . . . .	99
5.3.3.2	No-stridor vs Stridor . . . . .	101
5.3.3.3	MSA-C vs MSA-P . . . . .	102
5.3.4	AUC . . . . .	104
5.3.4.1	Healthy controls vs MSA . . . . .	104

*CONTENTS*

5

5.3.4.2	No-stridor vs Stridor . . . . .	106
5.3.4.3	MSA-C vs MSA-P . . . . .	108
5.3.5	Modularity . . . . .	110
5.3.5.1	Healthy controls vs MSA . . . . .	110
5.3.5.2	No-stridor vs Stridor . . . . .	112
5.3.5.3	MSA-C vs MSA-P . . . . .	114
5.3.5.4	Modularity visualization . . . . .	116
<b>6</b>	<b>Discussion</b>	<b>118</b>
<b>7</b>	<b>Conclusions and future directions</b>	<b>120</b>

.

# Introduction

Multiple System Atrophy (MSA) is a neurodegenerative movement disorder characterized by a combination of the following signs and symptoms: autonomic dysfunction, parkinsonism (muscle rigidity, tremor and slow movement), ataxia (poor coordination and unsteady walking). The cause of MSA is unclear and no specific risk factors have been identified. It is divided in two sub-types: MSA-P with a prevalence of parkinsonian symptoms and MSA-C with predominant cerebellar ataxia. Brain MR images in patients with MSA may reveal atrophy in cerebellum and brainstem areas. Approximately one-third of the patients with MSA suffer of a breathing abnormality called Stridor, that is a risk factor for sudden death. In this study we decided to consider the following groups: 36 MSA patients and 27 healthy controls (HC). The MSA group was divided into two sub-types: 20 MSA-C and MSA-P. The MSA group was also divided into two sub-groups: 22 patients without stridor and 14 patients with stridor. All these patients are followed by IRCCS “Istituto delle Scienze Neurologiche, DIBINEM, Bologna”.

A conventional screening to MSA patients includes a volumetric  $T_1$ -weighted ( $T_1$ -w) sequence that allows to have an excellent spacial definition of brain. Furthermore,  $T_1$ -w sequences help the distinction between different brain regions. For these reasons this sequence is used to segment Magnetic Resonance (MR) brain images.

Once brain images were segmented we evaluated volumes of different brain region. A key part of the thesis was the choice of the ROIs for the construction of the network targeted to the study of MSA patients. For this reason we have chosen to add seven ROIs belonging to the the infratentorial area, whose volumes are estimated with a semi-automatically procedure. To our knowledge, this kind of approach has been experienced for the first time by us. Although the procedure requires a manual drafting of infratentorial ROIs, it has been automated by registering on the 3D space of the individual subject.

The present work wants to investigate possible differences between groups using a relatively new methodological approach to investigate neuroimaging data, called graph-based analysis. The graph theory is the study of graphs, which are mathematical structures, made by nodes and edges that connect them. The graph theory is used to model many types of relations and processes and it can be applied in different fields of study. In the present work, we performed a graph theoretical analysis on structural MRI data to construct a network for

each group, with the aim of characterizing the morphometric covariance between brain regions. Using MR structural  $T_1$ -w imaging it is possible to obtain images with high resolution and really good contrast used to perform a detailed segmentation and extract volumes of different brain regions (using automatic software like Freesurfer) in order to create anatomical covariate networks. This objective may be achieved measuring global and regional topological properties and the modular organization from the resulting network derived from anatomical covariance. This kind of graph-based analysis applied on MSA patients and healthy controls has never been done before.

This thesis is organized as follows: the first chapter describes the basic principles of MRI technique, with a detailed explanation of the gradient echo sequences. The second chapter introduces the MSA, talking about clinical characteristics, pathology and pathogenesis. The third chapter goes into the graph theory, starting from the description of what a graph is and how a graph can be generated, and ending with a description of several possible measures that can be performed on these networks. The fourth chapter reports the methods and the materials that we used during the entire analysis and the fifth one shows the obtained results. The sixth chapter provides the discussion and the interpretation of the results, while the seventh chapter analyzes the possible future directions which might be explored.

# Chapter 1

## Magnetic resonance

Nuclear magnetic resonance (NMR) is a physical phenomenon in which nuclei in a magnetic field absorb and re-emit electromagnetic radiation. This energy is at a specific resonance frequency which depends on the strength of the magnetic field and on the magnetic properties of the isotope of the atoms.

Historically, NMR was first described and measured in molecular beams by Isidor Rabi in 1938, by extending the Stern–Gerlach experiment, and in 1944, Rabi was awarded the Nobel Prize in Physics for this work. In 1946, Felix Bloch and Edward Mills Purcell expanded the technique for use on liquids and solids, for which they shared the Nobel Prize in Physics in 1952. Another important contribution was given by Richard Robert Ernst that awarded the 1991 Nobel Prize in chemistry for the development of the method of high-resolution NMR spectroscopy. Paul Christian Lauterbur and Peter Mansfield awarded the 2003 Nobel Prize in Medicine for the production of the first 2D and then 3D MR images.

### 1.1 Theory of nuclear magnetic resonance

Isaac Rabi, thought the atom is a two level system with two possible configurations: ground state and excited state. He proved that if an electromagnetic field (frequency  $\omega$ ) is applied to an atom with the same frequency  $\omega_0 = \frac{(E_e - E_g)}{\hbar}$ , it could change its state from ground state energy  $E_g$ , to and excited state energy  $E_e$ , this phenomenon is known as resonance. In this model the system is approximated with a two possible level configurations and without an external electromagnetic field the probability of transition from one state to the another one is approximately equal to zero. Nuclear Magnetic Resonance uses the fact that nuclei have a magnetization associated with them. All nucleons, that is neutrons and protons, composing any atomic nucleus, have the intrinsic quantum property of spin that can be up or down. In human tissues the most common unpaired proton nucleus is hydrogen,  $^1H$ , it is contained in water molecules  $H_2O$ , and in fat  $-CH_2-$  [1]. If  $^1H$  is considered like a proton,

when a static magnetic field is applied, a splitting of nuclear state occurs. This interaction can form two energetic levels  $E_e$  and  $E_g$  called Zeeman's levels. The energetic gap between the two levels is:

$$\Delta E = \gamma \hbar B_0 \quad (1.1)$$

The proton spins form a magnetization vector  $M_0$  which has the same direction of the external field,  $B_0$ . Spins precess around  $B_0$  (Figure 1.1) with a frequency called Larmor frequency:

$$\omega_L = \gamma B_0 \quad (1.2)$$

where  $\gamma$  is the gyromagnetic ratio characteristic of the nuclei ( $^1H$  :  $\gamma = 42.58 \frac{MHz}{T}$  ).

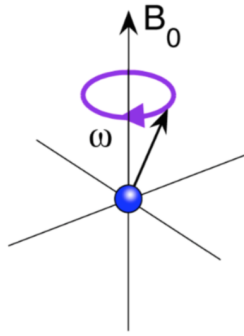


Figure 1.1: Nuclear spin precession respect to a static magnetic field  $B_0$

When a radiofrequency (RF) is applied with a weak magnetic field, the spins will also precess around the new magnetic field  $B_1$ . The net magnetization  $M_0$  has a spiral motion around the  $B_0$  axis, called “nutaton”. We can have the resonance condition of the hydrogen nuclei if the frequency of the RF pulse  $\omega$  is the same of  $\omega_L$ . This condition the RF pulse can give energy to the protons, and we can have an excited state of the atom. Adjusting duration and intensity of the RF pulse, we can flip the net magnetization  $M_0$  nutation angle. Rotation to the desired angle can be obtained by:

$$\theta = \gamma B_1 \tau \quad (1.3)$$

where  $\tau$  is the duration and  $B_1$  represent the strength of the RF pulse. Protons are first excited with the RF pulse, then the magnetization relaxes and returns exponentially aligned with the  $B_0$  axis. Relaxation is defined by two constants:  $T_1$  and  $T_2$  .  $T_1$  is the longitudinal relaxation time and describes the

time by which the magnetization aligns with the  $B_0$  axis ( $z$  axis).  $T_2$  is related to the energy exchange between protons and describes the relaxation in the  $xy$  plane orthogonal to the  $z$  axis.

Relaxation of protons produces a FID (Free Induction Decady) signal that can be detected by a receiver coil (Figure 1.2).  $T_1$  and  $T_2$  can be used to characterize different tissues, for example in liquid they are very similar (few seconds), in solid  $T_1$  is long (few minutes) and  $T_2$  is very short (few microseconds).  $T_2$  is used to be smaller or equal to  $T_1$  and in human tissue the value of  $T_1$  is between 150 and 1000 milliseconds [2].

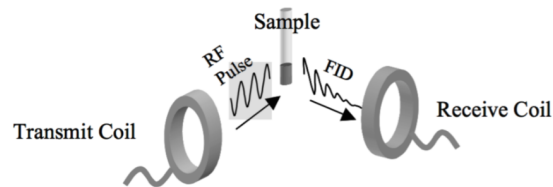


Figure 1.2: RF pulse excitation and FID relaxation.

## 1.2 Spin-echo sequence

Spin-Echo sequence (SE) is used to measure the relaxation signal. First of all protons are excited with a RF pulse (called  $90^\circ$ ) that brings the initial magnetization in the  $xy$  plane. Spins are in spread in the  $xy$  plane, precessing around  $z$  axis with different angular velocities. Erwin Hahn in his 1950 paper, applied a  $180^\circ$  RF pulse to invert the precession of spins, and return them to the beginning position. The phenomenon may be better understood by breaking it down into the following steps (Figure 1.3):

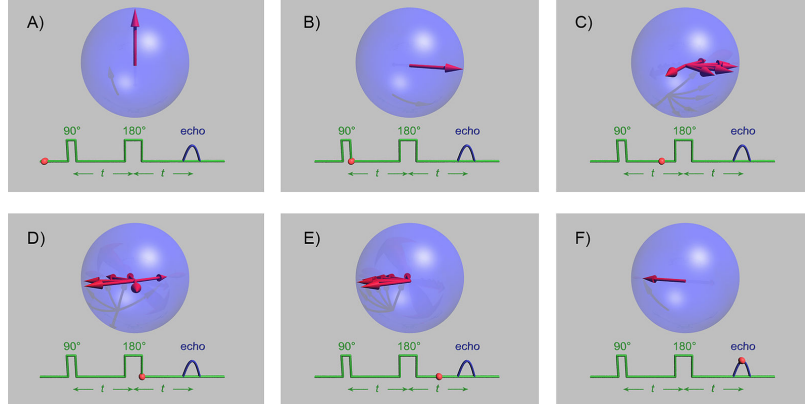


Figure 1.3: **A.** The vertical red arrow is the average magnetic moment of a group of spins, such as protons. All are vertical in the vertical magnetic field and spinning on their long axis, but this illustration is in a rotating reference frame where the spins are stationary on average. **B.** A 90 degree pulse has been applied that flips the arrow into the horizontal (xy) plane. **C.** Due to local magnetic field inhomogeneities (variations in the magnetic field at different parts of the sample that are constant in time), as the net moment precesses, some spins slow down due to lower local field strength (and so begin to progressively trail behind) while some speed up due to higher field strength and start getting ahead of the others. This makes the signal decay. **D.** A 180 degree pulse is now applied so that the slower spins lead ahead of the main moment and the fast ones trail behind. **E.** Progressively, the fast moments catch up with the main moment and the slow moments drift back toward the main moment. **F.** Complete refocusing has occurred and at this time, an accurate  $T_2$  echo can be measured with all  $T_2^*$  effects removed.

The signal acquired for the Spin-Echo sequence is:

$$S = N(H)(e^{-TE/T_2^*}(1 - e^{TR/T_1})) \quad (1.4)$$

where  $N(H)$  is the number of protons and  $M_0\alpha N(H)$ . Which was before flipped in the xy plane by the 90 degree RF pulse, will return aligned to the z axis; this is called  $T_1$  recovery of the relaxation signal.  $T_2^*$  concerns spin-spin interaction and is influenced by magnetic field inhomogeneities:

$$\frac{1}{T_2^*} = \frac{1}{T_2} + \gamma\Delta B \quad (1.5)$$

$M_0$  relaxation curves can be plotted on the same graph as we can see in Figure 1.4.

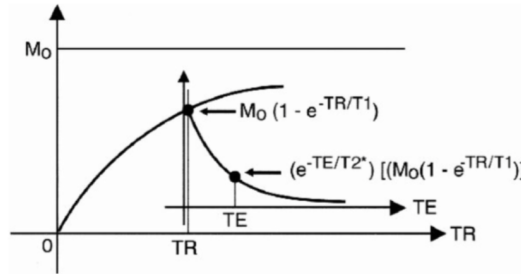


Figure 1.4: Recovery and decay curves plotted on the same graph

### 1.3 Relaxation times

Tissues are composed by different molecules and have different frequencies by which they release energy [3]. It is possible to define a function  $J(\omega)$  that describes the probability of a population to have a certain frequency for thermal motions. In Figure 1.5, we can see different curves for different materials. For example lipids as viscous liquids have the bigger probability of release the Larmor frequency  $\omega_0$  acquired during the excitation so they relax faster in the  $T_1$  dependent sequence.

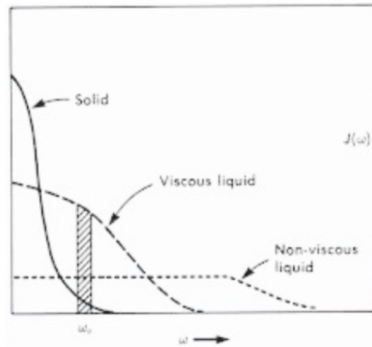


Figure 1.5: Spectrum of tumbling motions for different materials.

Since each material has characteristic relaxation times, we can acquire images from the same tissue with different information, for example  $T_1$  or  $T_2$  weighted images. As we can see in Figure 1.6 White Matter (WM) has a shorter  $T_1$  than Gray Matter (GM) so we can use  $T_1$ -dependent images to show gray-white matter contrast. While white matter acts in a similar way to fat because it is composed by protons of phospholipids, Cerebro Spinal Fluid (CSF) acts like water and it has the longest relaxation times.

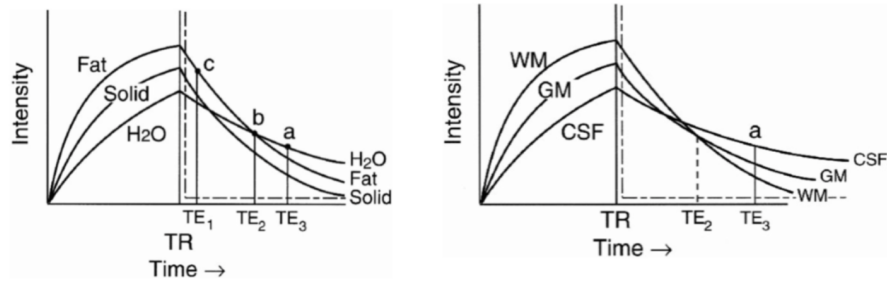


Figure 1.6: In the left panel:  $T_1$  and  $T_2$  decay curves of fat, water and solid tissue. In the right panel:  $T_1$  and  $T_2$  decay curves of CSF, white matter and grey matter.

## 1.4 Spatial position: K-space encoding

It is important to associate a spatial position to the acquired signal; we can do that using magnetic field gradients. Phase and frequency encoding are used to associate the acquired signal with a spatial position. Images are first acquired as a spectrum, that could be represented in a k-space, then the frequency-phase space is transformed back to the spatial coordinates by Fourier transform. As shown in Figure 1.7 a gradient is first applied due to excite a specific slice in a specific direction  $z$  (G slice), then two gradients orthogonal to the direction of the slice are applied in directions  $x$  and  $y$ . The first one characterized the frequency encoding (G freq) and the other the phase encoding (G phase). The gradient to select the slice is applied at the same time of the  $90^\circ$  pulse, while the frequency gradient is applied during the readout of the echo, when all the frequencies are acquired in a selected phase [4].

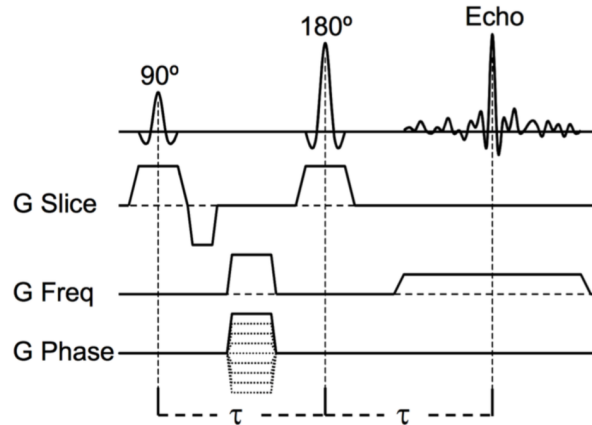


Figure 1.7: Pulse gradient sequence for a 3D spatial sampling.

## 1.5 Gradient echo sequences

Gradient echo sequences (GRE) are alternative techniques to spin echo sequences, differing from them in two principal points:

- utilization of gradient fields to generate transverse magnetization
- flip angles of less than  $90^\circ$

Compared to the spin echo and inversion recovery sequences, GRE sequences are more versatile. It is not only the basic sequence varied by adding dephasing or reshaping gradient at the end of the sequence, but there is a significant extra variable to specify in addition to the usual TR and TE. This is the flip or tip angle of the spins.

In gradient-echo (GE) or gradient recalled echo (GRE), it is used an RF pulse to flip  $M_0$  with an angle  $\alpha < 90^\circ$  [5]. It is not applied the  $180^\circ$  pulse but it is used a gradient to refocus the spins, thus the magnetic field inhomogeneities are even present and there is a weighting on  $T_2^*$  instead of  $T_2$ .

The GE sequences have a low weighting on  $T_1$ , because  $M_z$  does not have time to relax. However to increase the  $T_1$ -weighting is uses the spoiled GRASS (gradient recalled acquisition in the steady state) or SPGR (spoiled GRASS): this sequence “spoils” the steady-state transverse magnetization [6]. The word “spoiling” refers to the elimination or spoiling of the steady-state transverse magnetization. This task can be accomplished in different ways:

- by applying RF spoiling
- by applying variable gradient spoilers

- by lengthening TR

In the Figure 1.8 is represented the spoiled GRE sequence by using gradient spoilers.

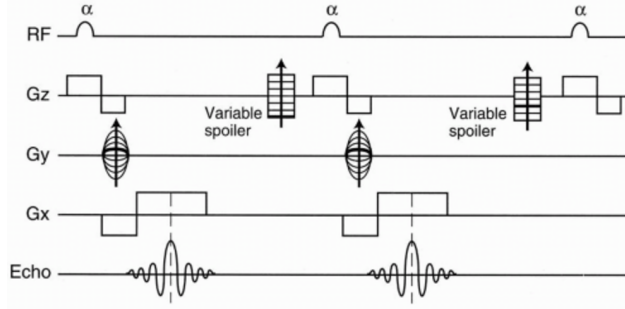


Figure 1.8: Spoiled GRE using gradient spoilers

Because the spoiled-GRE technique is specifically designed to disrupt transverse ( $T_2$ ) coherences, its major benefit and use is in producing  $T_1$ -weighted images. Nevertheless, both spin density- and  $T_2^*$ -weighting can be achieved by appropriate selection of parameters. As a result of this versatility and the ability to acquire images in either 2D or 3D modes, spoiled-GRE sequences are now ubiquitously used for MR imaging of virtually every body part.

The signal from a spoiled-GRE sequence depends on three operator-selectable parameters (TR, TE, and flip angle  $\alpha$ ) plus three intrinsic tissue parameters ( $T_1$ ,  $T_2^*$ , and spin-density [H]). Assuming a longitudinal steady-state has been reached and perfect spoiling, the signal (S) of a spoiled GRE sequence is given by [7]:

$$S = k[H] \frac{\sin\alpha(1 - e^{-TR/T_1})}{(1 - \cos\alpha)e^{-TR/T_1}} e^{-TE/T_2^*} \quad (1.6)$$

where k is a scaling factor. Setting  $dS/d\alpha = 0$  we find that the signal is maximized when  $\alpha = \alpha_E$ , the Ernest angle where  $\alpha_E = \arccos(e^{-TR/T_1})$ . Although the Ernest angle gives the highest signal for a given tissue for a certain  $TR/T_1$  combination, it does not necessarily maximize image contrast between two different tissues.

Discussing the equation 1.6 is important to consider some important things:

- Signal is always proportional to spin density [H], an effect that never be removed.
- TE controls  $T_2^*$ -weighting. The only place  $T_2^*$  appears in the equation is in the term  $e^{-TE/T_2^*}$ . When TE is large, this term dominates. When TE is small, this term approaches unity and the  $T_2^*$  contribution is minimized.

- Flip angle controls  $T_1$ -weighting. A small flip angle minimizes  $T_1$ -weighting because the longitudinal magnetization of various tissues are not different much by such a small angular displacement.
- TR controls  $T_1$ -weighting. Note that all occurrences of TR in the equation are in terms of the form  $e^{(-TR/T_1)}$ . When TR is small, this term becomes large and  $T_1$ -weighting increases. Conversely, when TR is long,  $T_1$ -weighting is minimized.

### 1.5.1 Fast Spoiled Gradient Recalled Echo (FSGRE)

It is true that GRE techniques are generally faster than SE techniques, although the Fast Spin Echo (FSE) technique may be equally fast. However, there are additional methods that can further increase the speed of scanning like the FSGRE technique. In order to make the GRE technique necessary to employ ultra shorts TRs and TEs to reduce the sequence time. This is achieved by the use of the following:

1. Fractional echo
2. Fractional RF
3. Reduction in the sampling time  $T_s$  (by increasing the bandwidth (BW), which is the frequency range between lowest and highest attainable frequency)

Basically, by using a fraction of the echo and a fraction of the pulse, we can in effect decrease TE. Increasing the BW results in a reduction of the sampling time. The trade-off here is a reduction of SNR because it is proportional to  $\frac{1}{\sqrt{BW}}$ . The sequence time is now given by:  $SeqTime = TE + Ts/2 + T_0$  where  $T_0$  is the “overhead” time and  $T_s$  is the total sampling time [8].

## Chapter 2

# Multiple System Atrophy

Multiple system atrophy (MSA) is a neurodegenerative movement disorder characterized by parkinsonism associated with various combinations of autonomic, pyramidal and cerebellar signs.

### 2.1 Historical background

In 1900, Dejerine and Thomas provided the first report of sporadic olivopontocerebellar atrophy (OPCA), a disease that later would have become a part of the spectrum of MSA [9]. Orthostatic hypotension as a manifestation of autonomic failure was described in 1925 [10]. In 1960, Shy and Drager reported patients with autonomic features of orthostatic syncope, impotence, and bladder dysfunction who went on to develop gait abnormalities, tremor, and fasciculations among other symptoms and signs. This disorder became known as the ShyDrager syndrome [11].

Also in 1960, the first cases of a predominantly asymmetric parkinsonian syndrome manifested primarily by akinesia and rigidity were reported. The authors suggested that striatonigral degeneration was the pathologic correlate for these cases.

In 1969, the term "multiple system atrophy" was introduced to encompass all three clinical syndromes: olivopontocerebellar atrophy, ShyDrager syndrome, and striatonigral degeneration. Striatonigral degeneration was later redefined as MSA with predominant parkinsonism (MSA-P), while olivopontocerebellar atrophy was redefined as MSA with predominant cerebellar ataxia (MSA-C) [12]. When autonomic failure predominates, the term ShyDrager syndrome may be used.

The discovery that glial cytoplasmic inclusions with alpha synuclein as a major component are the pathologic hallmark of the three clinical syndromes confirmed the suspicion that they were actually different manifestations of the same disease. Beginning in the 1990s, consensus groups developed guidelines to define MSA [13].

## 2.2 Epidemiology

The estimated prevalence of MSA is between 2 to 5 cases per 100,000 population [14]. In a metaanalysis of 433 pathologically proven cases of MSA, the mean age of onset was 54 years (range 31 to 78) (younger than Parkinson disease). Similarly, European registry studies have reported onset at a mean age of 56 to 60 years [15]. In these registries, MSA affects men and women about equally. However, other studies have reported that men are affected two to nine times more often than women. This finding may be secondary to earlier recognition of impotence as a major diagnostic feature in men. There is no specific racial predilection, and the disease has been reported in Caucasian, African, and Asian populations.

Although MSA is considered a sporadic disease, there are several reports of rare patients with probable or possible familial MSA [16].

## 2.3 Clinical characteristics

The main clinical features of MSA are akineticrigid parkinsonism, autonomic failure including urogenital dysfunction, cerebellar ataxia, and pyramidal signs in varying combinations. The onset of disease is marked by the initial clinical manifestation of any of its characteristic motor or autonomic features. However, the neuropathologic changes probably begin several years before the disease becomes symptomatic [17].

## 2.4 Motor involvement

The motor presentations of MSA are classified into two separate but overlapping clinical subtypes:

- MSA with predominant parkinsonism (MSA-P) subtype
- MSA with predominant cerebellar ataxia (MSA-C) subtype

In most studies from Europe and North America, cases of MSA-P outnumber MSA-C by between two and four to one. This contrasts with studies from Japan, which report MSA-C as more common than MSA-P. The predominant motor feature can change over time with disease progression. Thus, the designation of MSA-P or MSA-C refers to the predominant motor problem at the time the patient is evaluated. As an example, in a European study of 437 patients from 19 centers, the proportion of patients classified as MSA-P and MSA-C was 68 and 32 percent, respectively. However, among the entire cohort, parkinsonism and cerebellar ataxia were present in 87 and 64 percent, respectively [18].

Parkinsonism in MSA-P is characterized by akinesia/bradykinesia, rigidity, postural instability, and an irregular jerky postural and action tremor. Up to two-thirds of patients with MSA have this tremor involving the arms. Although much less common than in idiopathic Parkinson disease, rest tremor occurs in

as many as one-third of patients with MSA-P. Other warning signs that herald parkinsonism in MSA include postural instability and falls (usually within three years of motor onset), pyramidal signs, including extensor plantar responses, and rapid progression regardless of dopaminergic treatment [19]. Additional movement disorders associated with MSA-P may include stimulus-sensitive cortical myoclonus, hemiballism and chorea, and dystonia unrelated to dopaminergic therapy.

In contrast to MSA-P, the motor features of MSA-C involve predominant cerebellar dysfunction that manifests as gait ataxia, limb ataxia, ataxic dysarthria, and cerebellar disturbances of eye movements [20].

## 2.5 Sleep and breathing disorders (Stridor)

Sleep and breathing abnormalities are common in MSA. At least two-thirds of patients have rapid eye movement (REM) sleep behavior disorder. The content of the dreams can be vivid, violent, and frightening. The usual muscle atony in REM sleep is lost, and patients may act out their dreams. For example, patients may talk or shout during sleep and may strike out at their bed partner. This feature of MSA often precedes the motor manifestations, sometimes by decades. It tends to improve as the disease progresses .

Nocturnal or diurnal laryngeal stridor occurs in approximately one-third of patients with MSA [21]. It is a risk factor for sudden death in MSA. The sound of stridor is high pitched and occurs with inspiration. Patients may also experience sleep apnea and involuntary sighs or gasps during the day. Snoring may increase from premorbid level or may be new onset. These abnormalities of breathing are uncommon in idiopathic Parkinson disease and in other atypical parkinsonian syndromes. However, REM sleep behavior disorder and obstructive sleep apnea are not specific to MSA. REM sleep behavior disorder is frequently present in idiopathic Parkinson disease and some forms of spinocerebellar ataxia [22].

## 2.6 Cognitive function

Cognitive function in MSA tends to be relatively well preserved compared with idiopathic Parkinson disease and other atypical parkinsonian syndromes, possibly reflecting a lesser degree of cortical involvement in MSA and the younger age of onset. Nevertheless, although cognitive impairment in MSA is uncommon, it does occur and its presence does not exclude MSA as a clinical diagnosis in patients who have classic symptoms and signs of the disorder [23].

## 2.7 Pathology and pathogenesis

The cause of MSA is unknown. One postulated mechanism involves prion-like spreading of aberrant  $\alpha$ -synuclein from neurons to glia through functionally

connected networks, thereby leading to glial and myelin dysfunction and an inflammatory cascade that promotes secondary neurodegeneration.

Neuronal inclusions of various types also are present in the majority of patients with MSA. Myelin degeneration is characteristic of MSA. A small case-control study found a significantly greater degree of white matter hyperintensities on MRI scans from patients with MSA compared with scans from patients with Parkinson disease and healthy controls. This finding could be related to the loss of myelin or to cerebral hypoperfusion from orthostatic blood pressure fluctuations in MSA [24].

In idiopathic Parkinson disease, positron emission tomography imaging studies have indicated that dysautonomia is caused by peripheral nervous system dysfunction, particularly myocardial sympathetic denervation. In contrast, the peripheral autonomic system appears to be spared in MSA. Some persistence of autonomic tone may be responsible for the frequently observed supine hypertension in MSA.

Motor abnormalities seen in MSA-P are due primarily to neuronal loss and gliosis in the substantia nigra, putamen, caudate, and globus pallidus. One of the features that distinguish MSA and other atypical parkinsonian syndromes from idiopathic Parkinson disease is the lack of dramatic and sustained response to levodopa. The extent of putaminal involvement may determine the poor response to levodopa.

In contrast to MSA-P, the cerebellar ataxia and pyramidal signs that characterize the MSA-C subtype are secondary to degeneration of the cerebellar Purkinje cells, middle cerebellar peduncles, inferior olivary nuclei, basis pontis, and pontine nuclei. However, a majority of patients with MSA-P probably have subclinical loss of nigral neurons based upon findings from SPECT imaging. Loss of cholinergic mesopontine neurons, combined with loss of locus ceruleus neurons and preservation of rostral raphe neurons, may contribute to REM sleep abnormalities often seen in MSA. Respiratory abnormalities may reflect loss of cholinergic neurons in the arcuate nucleus of the ventral medulla. Respiratory stridor, abnormal nocturnal ventilation, and pseudobulbar features are possibly secondary to brainstem pathology, and may involve the nucleus ambiguus [25].

## 2.8 Neuroimaging

Brain MRI in patients with MSA-P and MSA-C may reveal atrophy of the putamen, pons, and middle cerebellar peduncles [25]. On  $T_2$  MRI sequences, signal changes include hypointensity of the posterior putamen, a hyperintense lateral putaminal rim, and hyperintensities of the middle cerebellar peduncles. These changes are supportive of the diagnosis of MSA rather than idiopathic Parkinson disease. However, they are not present in all patients with MSA. Furthermore, they are not specific for differentiating MSA from other atypical parkinsonian syndromes.

The "hot cross bun sign" refers to hyperintense  $T_2$  signal in the shape of a cross within the pons that arises from degeneration of transverse pontocerebellar

fibers. However, this is also a nonspecific finding that has also been described in patients with other causes of parkinsonism [26].

Diffusion weighted MRI in patients with MSA shows increased diffusivity (high apparent diffusion coefficient values) in the putamen, a finding that is sometimes observed in progressive supranuclear palsy. Preliminary data suggest that this technique can be used to monitor disease progression in MSA.

Positron emission tomography using ( $^{18}F$ ) fluorodeoxyglucose in patients with MSA may reveal regional glucose hypometabolism in the striatum, brainstem, and cerebellum, but the true sensitivity and specificity of these findings for differentiating MSA from Parkinson disease is uncertain.

## 2.9 Diagnostic criteria

The diagnosis of MSA is based upon the clinical features. No laboratory or imaging studies are diagnostic, particularly since findings are often normal or equivocal in early disease. Neuroimaging can be helpful in excluding other conditions and may show signs such as putaminal atrophy, slitlike signal change at the posterolateral putaminal margin, and hypointensity of the putamen relative to the globus pallidus [27].

A diagnosis of definite MSA is based upon postmortem pathology showing alpha-synuclein-positive glial cytoplasmic inclusions with neurodegenerative changes in striatonigral or olivopontocerebellar structures [28]. The clinical diagnosis of probable MSA during life requires the following features:

- A sporadic, progressive, adult onset (>30 years old) disease.
- Autonomic failure involving either urinary incontinence (inability to control the release of urine from the bladder, with erectile dysfunction in males) or an orthostatic blood pressure decrease within three minutes of standing by  $\geq 30$  mmHg systolic or  $\geq 15$  mmHg diastolic.
- Either poorly levodoparesponsive parkinsonism (bradykinesia with rigidity, tremor, or postural instability) or a cerebellar syndrome (gait ataxia with cerebellar dysarthria, limb ataxia, or cerebellar oculomotor dysfunction).

## 2.10 Neuroimaging criteria

Neuroimaging correlates of MSA lack sufficient sensitivity and specificity to be used as reliable markers of probable MSA. Nevertheless, current diagnostic criteria regard atrophy of putamen, middle cerebellar peduncle, or pons on MRI as supportive features for possible MSA-C or MSA-P [25].

Additional supportive features for MSA subtypes are as follows:

- In a patient with parkinsonian features but no cerebellar ataxia, hypometabolism of putamen, brainstem, or cerebellum on  $^{18}F$  emission to-

mography (FDG-PET) is considered to be a supportive feature for possible MSA-P.

- In a patient with cerebellar ataxia lacking parkinsonian features, two additional imaging features are considered to be supportive for possible MSA-C:
  - Hypometabolism of the putamen on FDG-PET
  - Presynaptic dopaminergic denervation in the striatum on functional imaging with single photon emission computed tomography (SPECT) or PET

## Chapter 3

# Graph theory

Graph theory is a branch of mathematics that deals with the formal description and analysis of graphs. A graph is defined simply as a set of nodes (vertices) linked by connections (edges), and may be directed or undirected. When describing a real-world system, a graph provides an abstract representation of the system's elements and their interactions.

### 3.1 History of graph theory

The origins of graph theory can be traced to Leonhard Euler who devised in 1736 a problem that came to be known as the "Seven Bridges of Königsberg" (Figure 3.1). The problem originated in the city of Königsberg [30], formerly in Germany but, now known as Kaliningrad and part of Russia, located on the river Pregel. The city had seven bridges, which connected two islands with the main-land via seven bridges.

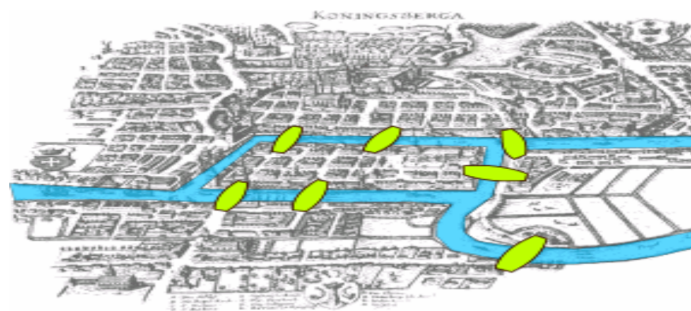


Figure 3.1: The seven bridges of Königsberg

People staying there always wondered whether there was any way to walk

over all the bridges once and only once. Euler came out with the solution in terms of graph theory. He proved that it was not possible to walk through the seven bridges exactly one time. He abstracted the case of Königsberg by eliminating all unnecessary features. He drew a picture (Figure 3.2) consisting of “dots” that represented the landmasses and the line-segments representing the bridges that connected those land masses.

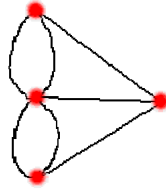


Figure 3.2: Königsberg bridges problem

This simplifies the problem to great extent. Now, the problem can be merely seen as the way of tracing the graph with a pencil without actually lifting it. One can try it in all possible ways, but you will soon figure out, it is not possible. But Euler not only proved that its not possible, but also explained why it is not and what should be the characteristic of the graphs, so that its edge could be traversed exactly once. He came out with the new concept of degree of nodes. The “Degree of Node” can be defined as the number of edges touching a given node. Euler proposed that any given graph can be traversed with each edge traversed exactly once if and only if it had, zero or exactly two nodes with odd degrees. The graph following this condition is called Eulerian circuit or path. We can easily infer this theorem. Exactly two nodes are beginning and end of your trip. If it has even nodes than we can easily come and leave the node without repeating the edge twice or more.

In case of seven bridges of Königsberg, once the situation was presented in terms of graph, the case was simplified as the graph had just 4 nodes, with each node having odd degree. So, Euler concluded that these bridges cannot be traversed exactly once.

Using this theorem, we can create and solve number of problems. Suppose now, we want to make the graph created from bridges of Königsberg, a Euler’s circuit. Now, as per Euler’s theorem we need to introduce a path to make the degree of two nodes even. And other two nodes can be of odd degree out of which one has to be the beginning and the other the endpoint. Suppose we want to start our journey from blue node and end at the yellow node. So, the two nodes can have odd edges. But somehow we need to edit the actual graph by adding another edge to the graph such that the two other nodes have even degree. So, the resulting figure is shown below (Figure 3.3).

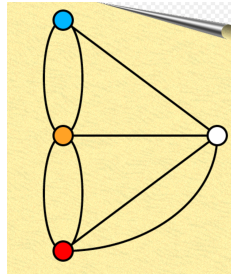


Figure 3.3: Example of final Königsberg bridges problem

## 3.2 Definitions

A graph is an ordered pair  $G = (V, E)$  comprising a set  $V$  of vertices or nodes together with a set  $E$  of edges.

### 3.2.1 The nature of links

An undirected graph (Figure 3.4) is a graph in which edges have no orientation. The edge  $(x, y)$  is identical to the edge  $(y, x)$ . The maximum number of edges in an undirected graph without a loop is  $\frac{n(n-1)}{2}$ .

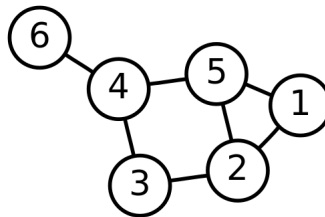


Figure 3.4: Undirected graph

A directed graph (Figure 3.5) is a graph in which edges have orientations. It is written as an ordered pair  $G = (V, A)$ . An arrow  $(x, y)$  is considered to be directed from  $x$  to  $y$ ;  $y$  is called the head and  $x$  is called the tail of the arrow;  $y$  is said to be a direct successor of  $x$  and  $x$  is said to be a direct predecessor of  $y$ . If a path leads from  $x$  to  $y$ , then  $y$  is said to be a successor of  $x$  and reachable from  $x$ , and  $x$  is said to be a predecessor of  $y$ . The arrow  $(y, x)$  is called the inverted arrow of  $(x, y)$ . A directed graph  $G$  is called symmetric if, for every arrow in  $G$ , the corresponding inverted arrow also belongs to  $G$ . A symmetric loopless directed graph  $G = (V, A)$  is equivalent to a simple undirected graph  $G' = (V, E)$ , where the pairs of inverse arrows in  $A$  correspond one-to-one with the edges in  $E$ .

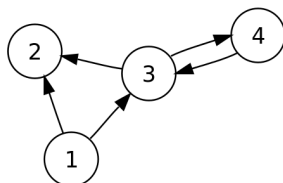


Figure 3.5: Directed graph

In this work we decided to use undirected graph.

### 3.2.2 Multiplicity of links

A simple graph, as opposed to a multigraph, is an undirected graph in which both multiple edges and loops are disallowed. In a simple graph the edges form a set (rather than a multiset) and each edge is an unordered pair of distinct vertices.

A multigraph is a graph which is permitted to have multiple edges. Thus two vertices may be connected by more than one edge. There are two distinct notions of multiple edges:

- Edges without own identity: The identity of an edge is defined solely by the two nodes it connects. In this case, the term "multiple edges" means that the same edge can occur several times between these two nodes.
- Edges with own identity: Edges are primitive entities just like nodes. When multiple edges connect two nodes, these are different edges.

A multigraph (Figure 3.6) is different from a hypergraph, which is a graph in which an edge can connect any number of nodes, not just two.

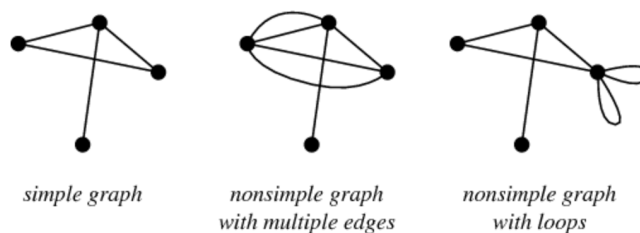


Figure 3.6: Examples of simple, non simple and non simple with loops graphs

In this study we used multigraph without loops.

### 3.2.3 Weighted/unweighted graph

A weighted graph (Figure 3.7) is a graph in which a number (the weight) is assigned to each edge. Such weights might represent for example costs, lengths

or capacities, depending on the problem at hand. Some authors call such a graph a network. Weighted correlation networks can be defined by soft-thresholding the pairwise correlations among variables (e.g. gene measurements).

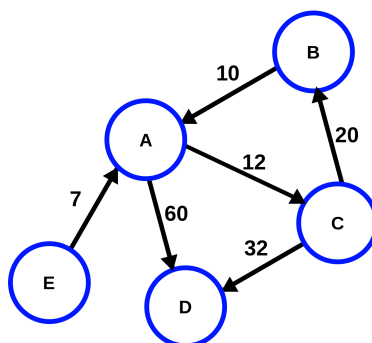


Figure 3.7: Weighted graph

In an unweighted graphs edges have no weight, so they simply show connections between nodes.

For our study we decided to used unweighted graphs.

### 3.3 Applications

Everything in our world is linked: cities are linked by street, rail and flight networks. Pages on the internet are linked by hyperlinks. The different components of an electric circuit or computer chip are connected and the paths of disease outbreaks form a network. Scientists, engineers and many others want to analyze, understand and optimise these networks. And this can be done using graph theory.

Graph theory can be used to analyze whatever is linked. Everything in our world is linked: cities are linked by street, rail and flight networks 3.8. Pages on the internet are linked by hyperlinks. The different components of an electric circuit or computer chip are connected and the paths of disease outbreaks form a network. Neurons in our brain are linked by synapses.

For example, graph theory can be applied to road networks, trying to find a way to reduce traffic congestion. An other useful application is in flight networks. Airlines want to connect cities in the most efficient way, moving the most passengers with the fewest possible trips. One area where speed and the best connections are of crucial importance is the design of computer chips. Integrated circuits (ICs) consist of millions of transistors which need to be connected. In recent years, there has been another important use of graph theory: the internet. Every page in the internet could be a vertex in a graph, and whenever there is a link between two pages, there is an edge between the corresponding vertices.



Figure 3.8: Example of flight networks

### 3.3.1 Complex brain networks

One of the most important applications of graph theory is the study of brain network. There are two main different approaches, one based on structural correlation and another one based on function systems. Both structural and functional brain networks can be explored using graph theory through the following four steps (Figure 3.9):

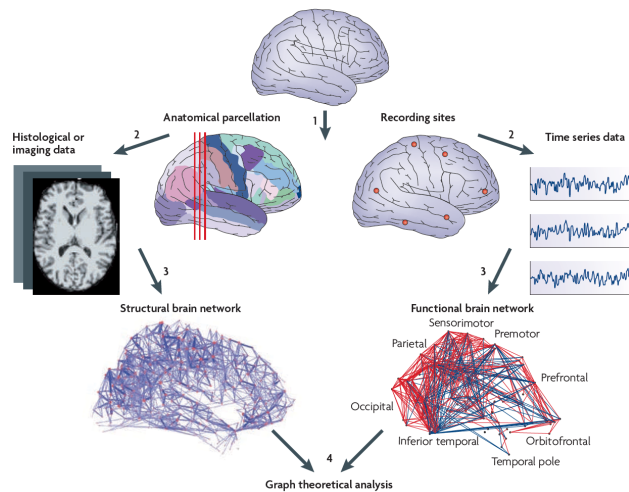


Figure 3.9: Structural and functional brain networks [30]

1. Define the network nodes.
2. Estimate a continuous measure of association between nodes. This could be for example connection probability between two regions of an individual diffusion tensor imaging data set, or the inter-regional correlations in cortical thickness or volume MRI measurements estimated in groups of subjects.
3. Generate an association matrix by compiling all pairwise associations between nodes and usually apply a threshold to each element of this matrix to produce a binary adjacency matrix or undirected graph.
4. Calculate the network parameters of interest in this graphical model of a brain network and compare them to the equivalent parameters of a population of random networks.

Many studies focus upon functional connectivity, using correlation analysis to identify regional connections, either with EEG/MEG or fMRI [34]. There has been a similar boom in studies of structural connectivity. Many groups employ diffusion-weighted imaging and tractography to examine structural connectivity as a white matter phenomenon [35]. In contrast to DWI approaches, there has been a growing interest in brain structure networks based on morphometric measures of GM volume, cortical thickness, and surface area. Graph generated from these different kind of approach have been found to follow a smallworld network organization as suggested by the brain networks of other connectivity modalities [36].

### 3.4 How to construct a brain graph

A brain graph is a model of a nervous system as a number of nodes interconnected by a set of edges. First of all it is necessary to decide which spatial level is considered: microscale, mesoscale or macroscale

- Constructing human brain connectome at microscale levels means that every node corresponds to a neuron and every edge to a synapse. This case is not realistic because of the excessive number, variability and dynamics of these elements. The number of neurons is estimated to be around  $10^{11}$  with about  $10^{15}$  connections between them. Recording and tracing this number of connections is not possible.
- The description of connection pattern at mesoscale level involves structures that generally contain about 100 neurons each and they may represent functional elements that are crucial for cortical information processing.
- The macroscale level is the most feasible organizational level for describing an accurate model of human connectome, with the definition of anatomically distinct brain regions and inter-regional connections. Most current

studies focus on macroscale networks, also because of technical limitations and computational demand.

After the choice of the description level, nodes and edges must be defined: the first ones generally correspond to Regions Of Interest (ROIs) derived from anatomical atlas or appropriate segmentation process, and the edges can be defined as functional or structural association between these ROIs.

### 3.4.1 Nodes and links decisions

According to Bullmore and Basset [32], a node should be a portion of the system that could be separable from the rest of the system. Generally, nodes represent brain regions, which are labelled by a particular atlas. The choice of a template is a very important and delicate step because it determines different network structures and different topological characteristics.

There is not a unified method to choose edge between nodes. They are differentiated on the basis of the type of the connectivity, which could be functional or structural, but also on the fact that they could have weights and directionality.

We focused our attention on structural association between nodes, because we were interested in obtain the structural connectivity between brain regions, and not the functional one. More precisely we considered the correlations between the volume of different brain regions.

### 3.4.2 Correlations and adjacency matrices

Due to create an unweighted graph is necessary to generate an adjacent matrix. In order to create this matrix we have to define the correlation matrix and than apply a threshold to all values of it: if  $a_{ij} \geq \tau$  the corresponding element of the adjacency matrix is set to 1; 0 otherwise.

There are two possible choice for the implementation process to the adjacent matrix:

- to choose an optimal value of threshold to be applied to the correlation matrix and to describe the topological parameters of the network only at that threshold;
- to choose different values of threshold and describe the network properties as a function of threshold (or connection density);

The adjacency matrix so defined corresponds to the final network.

## 3.5 Measures

Once the brain network is constructed it is possible to characterize it using different topological measures. Here we propose only a few of these measures.

In order to understand the graph measures below it is important to define some variable.  $N$  is the set of all nodes in the network, and  $n$  is the number of

nodes.  $L$  is the set of all links in the network, and  $l$  is number of links. With the expression  $(i, j)$  we refer to a link between nodes  $i$  and  $j$ , ( $i, j \in N$ ). In the equations that we can find in this chapter,  $a_{ij}$  is the connection status between  $i$  and  $j$ :  $a_{ij} = 1$  when link  $(i, j)$  exists (when  $i$  and  $j$  are neighbors);  $a_{ij} = 0$  otherwise ( $a_{ii} = 0$  for all  $i$ ). We compute the number of links as  $l = \sum_{ij \in N} a_{ij}$  (to avoid ambiguity with directed links we count each undirected link twice, as  $a_{ij}$  and as  $a_{ji}$ ) [31].

### 3.5.1 Node degree and degree distribution

The degree of a node (Eq.3.1) is the number of connections that link it to the rest of the network.

$$k_i = \sum_{j \in N} a_{ij} \quad (3.1)$$

This one of the most fundamental network measure and most other measures are linked to node degree. In random networks all connections are equally probable, resulting in a Gaussian and symmetrically centered degree distribution. Complex networks generally have non-Gaussian degree distributions, often with a long tail towards high degrees. The degree distributions of scale-free networks follow a power law [31].

### 3.5.2 Shortest path length

Shortest path length (Eq.3.2) is a basis for measuring the integration of the network. It represents the distance between nodes  $i$  and  $j$ .

$$d_{ij} = \sum_{a_{uv} \in g_{i \leftrightarrow j}} a_{uv} \quad (3.2)$$

Where  $g_{i \leftrightarrow j}$  is the shortest path (geodesic) between  $i$  and  $j$ .

### 3.5.3 Connected components

Connected component (or just component) of an undirected graph is a subgraph in which any two vertices are connected to each other by paths, and which is connected to no additional vertices in the super graph. For example, the graph shown in Figure 3.10 has three connected components. A vertex with no incident edges is itself a connected component. A graph that is itself connected has exactly one connected component, consisting of the whole graph.

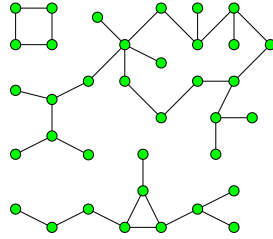


Figure 3.10: A graph with three connected components

This measure is useful to understand when a graph is fully connected because the connected component is equal to 1.

### 3.5.4 Clustering coefficient

If the nearest neighbors of a node are also directly connected to each other they form a cluster. The clustering coefficient (Eq.3.3) quantifies the number of connections that exist between the nearest neighbors of a node as a proportion of the maximum number of possible connections. Random networks have low average clustering whereas complex networks have high clustering (associated with high local efficiency of information transfer and robustness). Interactions between neighboring nodes can also be quantified by counting the occurrence of small motifs of interconnected nodes. The distribution of different motif classes in a network provides information about the types of local interactions that the network can support.

$$C = \frac{1}{n} \sum_{i \in N} \frac{\sum 2t_i}{k_i(k_i - 1)} \quad (3.3)$$

### 3.5.5 Path length and Efficiency

Path Length (Eq.3.4) is the minimum number of edges that must be traversed to go from one node to another. Random and complex networks have short mean path lengths (high global efficiency of parallel information transfer) whereas regular lattices have long mean path lengths. Efficiency is inversely related to path length but it is numerically easier to use to estimate topological distances between elements of disconnected graphs. The average over all pair wise efficiencies is the Global Efficiency of the graph (Eq.3.5); the Local Efficiency (Eq.3.6) is the mean of the efficiencies of all subgraphs  $G_i$  of neighbors of each of the vertices of the graph.

$$L = \frac{1}{n} \sum_{i \in N} \frac{\sum_{j \in N, j \neq i} d_{ij}}{n - 1} \quad (3.4)$$

$$E_{glob} = \frac{1}{N(N-1)} \sum_{i,j \in N} \frac{1}{d_{i,j}} \quad (3.5)$$

$$E_{loc} = \frac{1}{N} \sum_{i \in N} E(G_i) \quad (3.6)$$

### 3.5.6 Hubs, centrality and robustness

Hubs are nodes with high degree, or high centrality. The centrality of a node measures how many of the shortest paths between all other node pairs in the network pass through it. A node with high centrality is crucial to efficient communication. The importance of an individual node to network efficiency can be assessed by deleting it and estimating the efficiency of the ‘lesioned’ network. Robustness refers either to the structural integrity of the network following deletion of nodes or edges or to the effects of perturbations on local or global network states.

### 3.5.7 Modularity

A graph can generally be subdivided or partitioned into subsets or modules of nodes (Figure 3.11). Modularity quantifies the extent to which the network can be decomposed into sub-networks that are more connected within modules than between modules. Several alternative algorithms have been proposed to find the mathematically optimal modular decomposition for a network. In general, the aim is to find the partition that maximizes the ratio of intramodular to inter-modular edges. Thus the nodes in any module will be more densely connected to each other than to nodes in other modules [?].

Popular methods for discovering the modules of a network consists in optimizing modularity, that is to find the partition having the largest value of  $Q$ .

$$Q = \frac{1}{2m} \sum_{C \in P} \sum_{i,j \in C} [A_{ij} - \frac{k_i k_j}{2m}] \quad (3.7)$$

where  $A$  is the adjacent matrix of the network;  $m$  is the total number of edges and  $k_i = \sum_j A_{ij}$  is the degree of the node  $i$ . The indices  $i$  and  $j$  run over the  $N$  nodes of the graph. The index  $C$  runs over the modules of partition  $P$ .

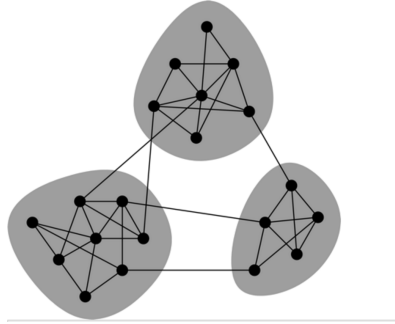


Figure 3.11: Modularity

### 3.5.8 Random, scale-free and small-world networks

In random graphs each pair of nodes has an equal probability,  $p$ , of being connected. Large random graphs have Gaussian degree distributions. It is now known that most graphs describing real-world networks significantly deviate from the simple random-graph model (Figure 3.12) [39].

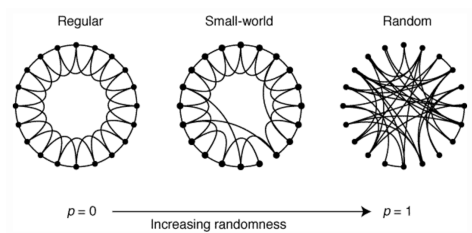


Figure 3.12: Small world

Some networks have degree distributions in the form of a power law: that is, the probability that a node has degree  $k$  is given as  $\text{Prob}(k) \sim k^{-\lambda}$ . In biological systems, the degree exponent  $\lambda$  often ranges between 2 and 3, and the very gradual ('heavy-tail') power law decay of the degree distribution implies that the network lacks a characteristic scale: such networks are called 'scale-free' networks. Barabási and Albert demonstrated that scale-free networks can originate from a process by which each node that is added to the network as it grows, connects preferentially to other nodes that already have high degree [40]. Scale-free networks are unlikely if the attachment of connections is subjected to physical constraints or associated with a cost. Therefore, physically embedded networks, in which nodes have limited capacity for making connections, often do not have pure power law degree distributions but may instead demonstrate exponentially truncated power law degree distributions, which are associated with a lower probability of very high degree nodes.

Originally described in social networks, the ‘small-world’ property combines high levels of local clustering among nodes of a network and short paths that globally link all nodes of the network. This means that all nodes of a large system are linked through relatively few intermediate steps, despite the fact that most nodes maintain only a few direct connections. Small-world organization is intermediate between that of random networks, the short overall path length of which is associated with a low level of local clustering, and that of regular networks or lattices, the high-level of clustering of which is accompanied by a long path length. A convenient single-number summary of small-worldness is thus the ratio of the clustering coefficient to the path length after both metrics have been standardized by comparing their values to those in equivalent random networks. Evidence for small-world attributes has been reported in a wide range of studies of genetic, signaling, communications, computational and neural networks. These studies indicate that virtually all networks found in natural and technological systems have non-random/non-regular architectures. They show small-world architectures and that the ways in which these networks deviate from randomness reflect their specific functionality.

Small-world topology is defined as a network that has  $\sigma \gg 1$  :

$$\sigma = \frac{\frac{C}{C_{rand}}}{\frac{L}{L_{rand}}} = \frac{C_{norm}}{L_{norm}} \quad (3.8)$$

where  $C$  is the Clustering  $C$  of the tested network,  $C_{rand}$  is the Clustering Coefficient of random network,  $L$  represent the Characteristic Path Length of the tested network,  $L_{rand}$  is the Characteristic Path Length of random network.  $C_{norm}$  and  $L_{norm}$  are Normalized Clustering  $C$  and Normalized Characteristic Path Length respectively.

## Chapter 4

# Materials and methods

### 4.1 Participants

Thirty-six MSA patients participated in the study. The group of patient can be furthermore subdivided in 14 MSA with Stridor and 22 No-Stridor. In the group of MSA there are 20 patient with MSA-C variant and 16 affected by MSA-P. A total of 27 healthy controls were selected to match the patient group in age and gender. All subjects gave consent to personal data processing for research purposes and the protocol was approved by the local Ethical Committee. Detailed information are summarized in Table 4.1 and Table 4.2.

The MSA patients included were evaluated at the movement disorders outpatient clinics of the IRCCS Istituto di Scienze Neurologiche of Bologna (IT) and underwent a brain MR scan as part of their diagnostic workup at the Functional MR Unit of the Policlinico S. Orsola – Malpighi in Bologna (IT). Clinical evaluation and diagnosis was performed by neurologists expert in movement disorders and according to current diagnostic criteria. In order to confirm the presence of stridor, all patients underwent a night video polysomnography (VPSG) [41].

	MSA			HC
	TOT	Stridor	No Stridor	-
N(%)	36(100)	14(39)	22(61)	27
AAE(y)[mean±SD]	61±9	62±9	61±10	57±10
range(y)	41-85	48-79	41-85	40-83
sex(M/F)	28/8	10/4	18/4	12/15
DD(y)[mean±SD]	5±3	5±3	5±3	-
MSA-C(%)	20(56)	9(64)	11(50)	-

Table 4.1: General information of No-stridor and Stridor groups. Legend: AAE: age at evaluation; SD: standard deviation, MSA-C: cerebellar variant of MSA; HC: healthy controls; M: male; F: Female; DD: disease duration

	MSA			HC
	TOT	MSA-C	MSA-P	-
N(%)	36(100)	20(56)	16(44)	27
AAE(y)[mean±SD]	61±9	60±9	63±10	57±10
range(y)	41-85	45-85	41-79	40-83
sex(M/F)	28/8	14/6	14/2	12/15
DD(y)[mean±SD]	5±3	5±4	5±2	-
Stridor(%)	14(39)	9(45)	5(31)	

Table 4.2: General information of MSA-C and MSA-P groups. Legend: AAE: age at evaluation; SD: standard deviation; MSA-C: cerebellar variant of MSA; MSA-P: parkinsonism variant of MSA; HC: healthy controls; M: male; F: Female; DD: disease duration

## 4.2 MRI data acquisition

All subjects underwent the same standardized brain MR protocol on a 1.5 Tesla GE Medical Systems Signa HDx 15 system equipped with a quadrature birdcage head coil. Structural imaging included: coronal FLAIR  $T_2$ -weighted (repetition time, TR=8000 ms, inversion time, TI=2000 ms, echo time, TE=93.5 ms, 3 mm slice thickness with no inter-slice gap), and 3D volumetric  $T_1$ -weighted fast spoiled gradient-echo (FSPGR) images with the following parameters:

- TR=12.5 ms
- TE=5.1 ms
- TI=600 ms
- FOV 25.6 cm<sup>2</sup>
- Isotropic voxel 1 mm

An expert neuroradiologist visualized MR images obtained from each subject in order to exclude secondary causes of parkinsonism or other abnormalities.

## 4.3 Data pre-processing

The ultimate goal of pre-processing steps is to evaluate the volumes of all brain regions that will be used to create the graph. A software called Freesurfer [42] is used to calculate the volume of brain regions. Using Freesurfer it is possible to get morphological information about supratentorial and infratentorial regions, but it returns a unique volume value for the whole brainstem region Figure 4.1. We were particularly interested in investigating regions of the brainstem because they are the most impaired in MSA. To do that seven brain regions (Midbrain, Pons, Medulla, Right-SCP, Left-SCP, Right-MCP, Left-MCP) included in the

brainstem were hand drawn on MNI atlas [43] and then registered on subject specific space to evaluate volumes.

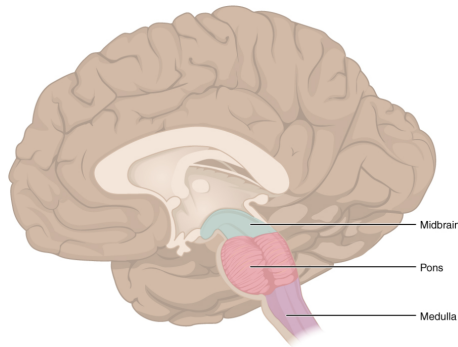


Figure 4.1: Structures of the brainstem

### 4.3.1 Brain Extraction Tool (BET)

Every  $T_1$ -w images were processed with Brain Extraction Tool (provided by FSL [44]) in order to delate non-brain tissue from images of whole head. In Figure 4.2 it is shown how BET works on a brain image.

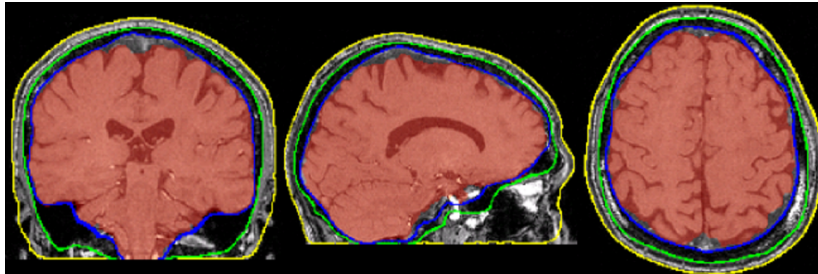


Figure 4.2: Example of BET

This is an obligatory step for the linear registration that will be applied. There were some subjects where BET did not work, so it was necessary to adjust parameters (-f and -g) to get the best results out. The -f option in BET is used to set a fractional intensity threshold which determines where the edge of the final segmented brain is located. The default value is 0.5 and the valid range is 0 to 1. A smaller value for this threshold will cause the segmented brain to be larger and should be used when the overall result from BET is too small (inside the brain boundary). Obviously, larger values for this threshold have the opposite effect (making the segmented brain smaller). The -g option in BET causes a gradient change to be applied to the previous threshold value. That is,

the value of the  $-f$  intensity threshold will vary from the top to the bottom of the image, centered around the value specified with the  $-f$  option. The default value for this gradient option is 0, and the valid range is -1 to +1. A positive value will cause the intensity threshold to be smaller at the bottom of the image and larger at the top of the image. This will have the effect of increasing the estimated brain size in the bottom slices and reducing it in the top slices.

In 25 cases BET worked successfully as it is shown in Figure 4.3. For 7 images we decided to use the skull removal of Freesurfer using the command `-no>skullstrip`. Unfortunately the registration of four brains did not work because the brain extraction in the cerebellum region was not good enough, so we decided to remove the entire cerebellum to do the registration. To do that we created a cerebellum mask (Figure 4.4) and then we subtracted it from the input image. This problem occurs because the fact that cerebellum of MSA patients, in particular MSA-C patient, is really atrophic and cause problems during registrations (Figure 4.5).

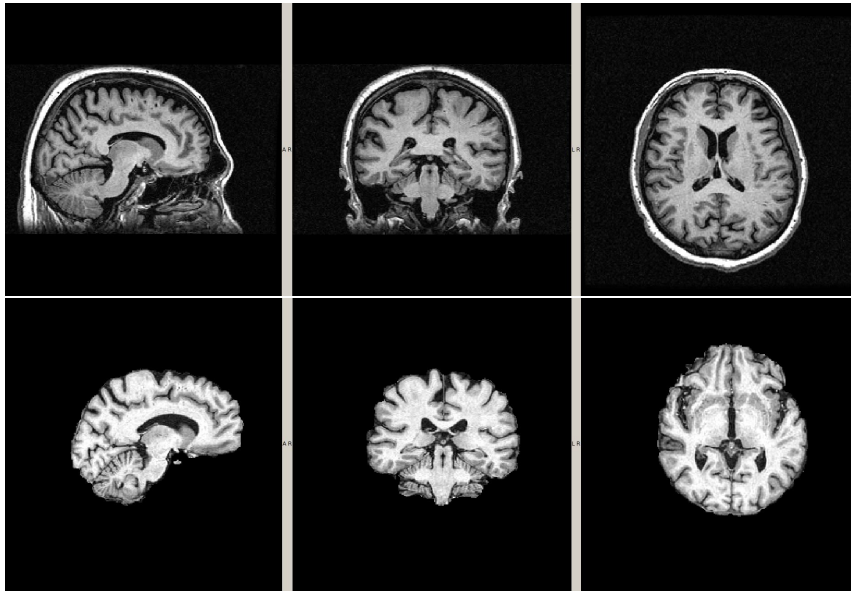


Figure 4.3:  $T_1$ -w image of healthy control where BET procedure works successfully

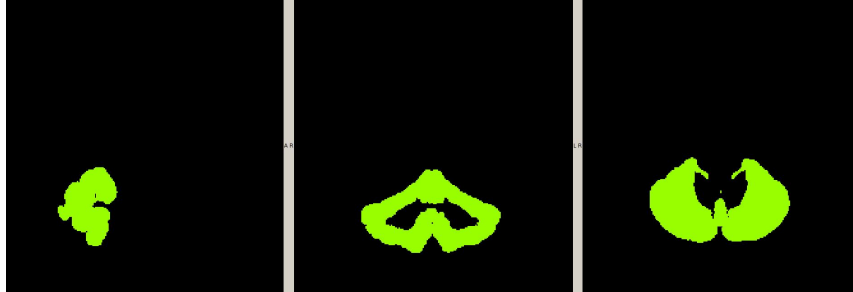


Figure 4.4: Cerebellum mask

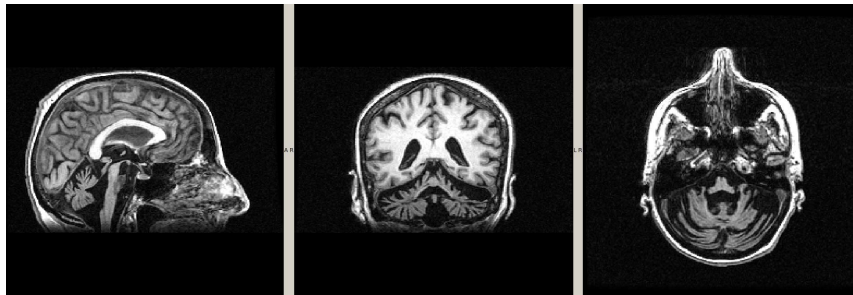


Figure 4.5: Example of atrophic cerebellum in MSA-C patient

### 4.3.2 Lesion Filling (LF)

This process takes a user-defined lesion mask (created manually by a neuro-radiologist on GIMP software [45]) on a structural image  $T_2$ -weighted and then registered on the 3D  $T_1$ -w in order to "fill" the lesion area in the structural image with intensities that are similar to those in the non-lesion neighborhood (restricted to white matter only). It has been shown [46] that using such a method as part of a pre-processing pipeline can improve the registration and segmentation of pathological brains and the resultant volumetric measures of brain tissue [47].

### 4.3.3 Freesurfer

Using the "recon-all" command in Freesurfer, 82 brain region were segmented (Figure 4.6) and volumes were evaluated for the entire dataset on  $T_1$ -w images or on  $T_1$ -w images after lesion filling if it was present. At this point we want to calculate the volume of the 7 different regions in the brainstem that are not segmented automatically by Freesurfer.

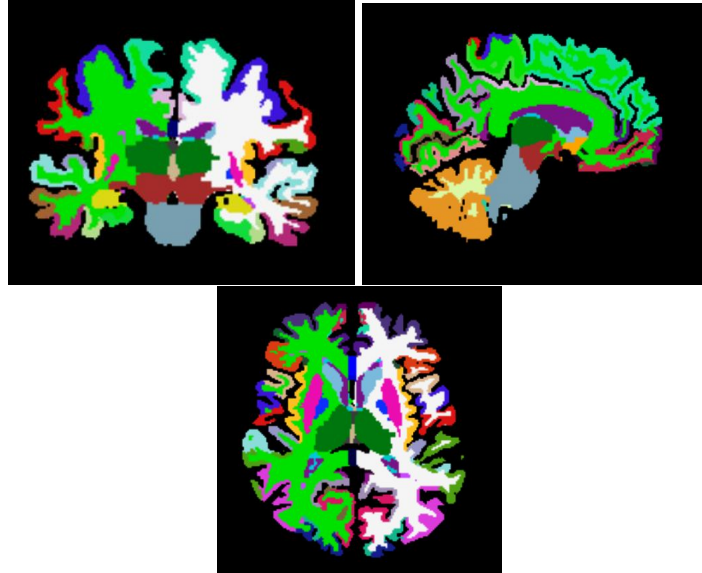


Figure 4.6: Freesurfer segmentation. From left to right: coronal, sagittal and axial view

#### 4.3.4 Brainstem regions

To evaluate the volume of the seven brain regions included in the brainstem described before, a neuroradiologist drew them on the MNI and then all 3D  $T_1$ -w images were registered on MNI (Figure 4.7). Registration algorithms can be divided into linear and non-linear depending on the type of deformations they permit.

The first registration is a linear registration and for this step we used FLIRT (FMRIB's Linear Image Registration Tool). Linear registration means that an image can translate, rotate, zoom and shear to match with another. It uses images without skull, that is why the BET process is so important. The main options are: an input `-in` ( $T_1$ -w images after LF) and a reference `-ref` (MNI) volume; the calculated affine transformation that registers the input to the reference which is saved as a 4x4 affine matrix `-omat`; and the output volume `-out` which is the result obtained transforming the input volume to align with the reference image. For these usages the reference volume must still be specified as this sets the voxel and image dimensions of the resulting volume. For the registration we set 12 degrees of freedom.

The second registration is a non-linear registration, and for this step we used FNIRT (FMRIB's Non-linear Image Registration Tool) that performs non-linear transformations like contraction and dilations in order to have a better registration of images on MNI.

Finally, the transformations were inverted so all the seven regions were registered back on their specific space in order to evaluate their volumes.

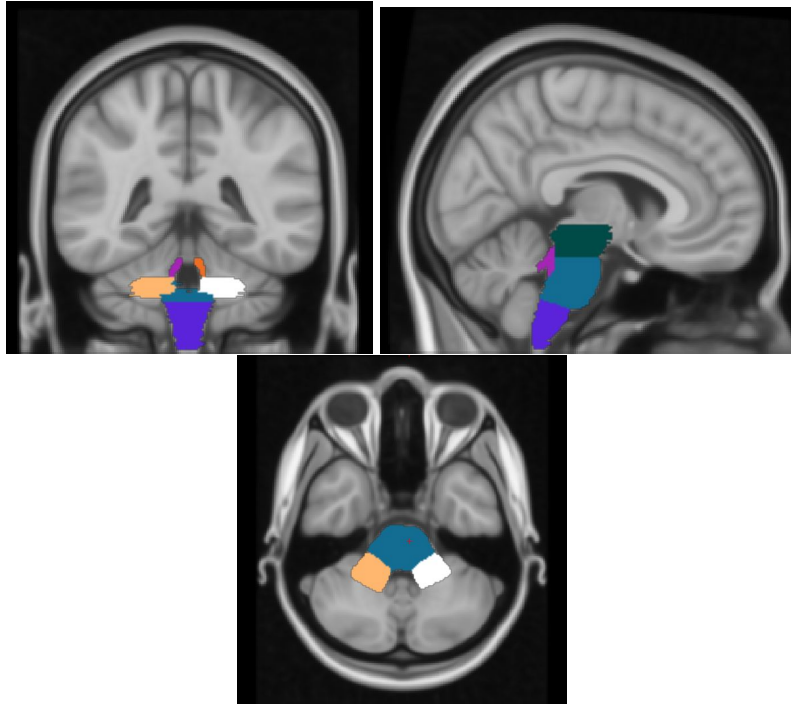


Figure 4.7: Brainstem regions hand drawn. From the left to the right: coronal, sagittal and axial view

## 4.4 Construction of structural correlation network

### 4.4.1 Node decision

We wanted to create a graph for each group of subjects (MSA, Stridor, No-Stridor, Healthy Controls) and then compare them with a statistical analysis.

To do that our correlation matrices were constructed based on pair-wise correlations between ROI pairs (negative correlations were replaced with zero). The structural correlation between a ROI pair of  $i$  and  $j$  was defined as the Pearson correlation coefficient between their mean GM volumes across the subjects within a group.

In order to obtain the volumes of ROIs it is necessary to choose a way to segment our 3D brain  $T_1$ -w images in different regions. To obtain the ROIs in our study we resorted to a specific software, Freesurfer [42], that works with complex segmentation algorithms. Freesurfer is an open source software suite for

processing and analyzing brain MRI images. We performed it for each subject and this allowed us to obtain regions subject-specific, this process takes about 12 hours (depending on the performance of the computer processor). We then obtained all the ROIs that Freesurfer was able to segment, and we chose 82 regions between these covering the entire cortex and deep grey matter. Since MSA disease produces particular changes in volume in brainstem regions, we were particularly interested to study these structures. To do this, some regions were hand drawn in the space of MNI. In particular seven brain regions were hand drawn (Midbrain, Pons, Medulla, Right-SCP, Left-SCP, Right-MCP, Left-MCP). In Table 4.3 Table 4.4 and Table 4.5 subcortical and cortical ROIs are listed. All the regions, i.e. the future nodes, are associated with a number which will make the identification easier.

N	ROI
1	Left-cerebellum-cortex
2	Left-thalamus-proper
3	Left-Caudate
4	Left-Putamen
5	Left-pallidum
6	Left-hippocampus
7	Left-amygdala
8	Left-accumbens-area
9	Right-cerebellum-cortex
10	Right-thalamus-proper
11	Right-caudate
12	Right-putamen
13	Right-pallidum
14	Right-hippocampus
15	Right-amygdala
16	Right-Accumbens-area
17	Left-superiorparietal
18	Left-caudalanteriorcingulate
19	Left-cuneus
20	Left-rostralanteriorcingulate
21	Left-isthmuscingulate
22	Left-pericalcarine
23	Left-transversetemporal
24	Left-caudalmiddlefrontal
25	Left-fusiform
26	Left-parstriangularis
27	Left-temporalpole
28	Left-postcentral
29	Left-superiortemporal
30	Left-middletemporal
31	Left-entorhinal
32	Left-rostralmiddlefrontal
33	Left-parsorbitalis
34	Left-inferiortemporal
35	Left-frontalpole
36	Left-posteriorcingulate
37	Left-medialorbitofrontal
38	Left-lateraloccipital
39	Left-paracentral
40	Left-parahippocampal
41	Left-insula
42	Left-supramarginal

Table 4.3: List of ROIs

N	ROI
43	Left-lingual
44	Left-parsopercularis
45	Left-inferiorparietal
46	Left-precentral
47	Left-superiorfrontal
48	Left-lateralorbitofrontal
49	Left-precuneus
50	Right-superiorparietal
51	Right-caudalanteriorcingulate
52	Right-cuneus
53	Right-rostralanteriorcingulate
54	Right-isthmuscingulate
55	Right-pericalcarine
56	Right-transversetemporal
57	Right-caudalmiddlefrontal
58	Right-fusiform
59	Right-parstriangularis
60	Right-temporalpole
61	Right-postcentral
62	Right-superiortemporal
63	Right-middletemporal
64	Right-entorhinal
65	Right-rostralmiddlefrontal
66	Right-parsorbitalis
67	Right-inferiortemporal
68	Right-frontalpole
69	Right-posteriorcingulate
70	Right-medialorbitofrontal
71	Right-lateraloccipital
72	Right-paracentral
73	Right-parahippocampal
74	Right-insula
75	Right-supramarginal
76	Right-lingual
77	Right-parsopercularis
78	Right-inferiorparietal
79	Right-precentral
80	Right-superiorfrontal
81	Right-lateralorbitofrontal
82	Right-precuneus

Table 4.4: List of ROIs

N	ROI
83	Midbrain
84	Pons
85	Medulla
86	Right-SCP
87	Left-SCP
88	Right-MCP
89	Left-MCP

Table 4.5: List of ROIs

#### 4.4.2 Volume of ROIs

Freesurfer was used to evaluate volumes of each ROI. Then, using the software JMP [49], we verified (only in HC group), if volumes of ROI was correlated with age or total intracranial volume (TIV). So a linear regression was performed to regress out the effect of age and total brain volume.

#### 4.4.3 Definitions of correlations matrices

Thereafter, a correlation matrix R was established for the healthy controls and MSA groups respectively by computing the structural correlation between each pair of ROIs from all the eighty-nine. So in each cell of the correlation matrix there is a number between -1 and 1 that represent the Pearson correlation coefficient between ROI's. The diagonal elements of the constructed correlation matrix are set to zero.

**Context Likelihood of Relatedness algorithm (CLR)** We tried to use this algorithm to estimate the correlation between regions, instead of Pearson correlation coefficient. This method is mainly used in studies of gene expression [60].

The CLR algorithm estimates a likelihood of the mutual information (MI) score for a particular pair of regions,  $i$  and  $j$ , by comparing the MI value for that pair of regions to a background distribution of MI values (the null model). The background distribution is constructed from two sets of MI values:  $\{MI_i\}$ , the set of all the mutual information values for gene  $i$  (in row or column  $i$ ), and  $\{MI_j\}$ , the set of all the mutual information values for gene  $j$  (Figure 4.8). Because of the sparsity of biological regulatory networks, most MI scores in each row of the mutual matrix represent random background MI. We approximate this background MI as a joint normal distribution with  $MI_i$  and  $MI_j$  as independent variables, which provides a reasonable approximation to the empirical distribution of mutual information. The final form of our likelihood estimate becomes  $f(Z_i, Z_j) = \sqrt{Z_i^2 + Z_j^2}$ , where  $Z_i$  and  $Z_j$  are the z-score of  $MI_{ij}$  from the marginal distribution, and  $f(Z_i, Z_j)$  is the joint likelihood measure.



## 4.5 Data analysis

### 4.5.1 Network analysis

The small-worldness of a complex network, as described before, has two key metrics: the clustering coefficient  $C$  and the characteristic path length  $L$  of the network. The clustering coefficient of a node is a measure of the number of edges that exist between its nearest neighbors and is a measure of network segregation. The characteristic path length of a network is the average shortest path length between all pairs of nodes in the network and is the most commonly used measure of network integration [31]. To evaluate the topology of the brain network, these parameters must be compared to the corresponding mean values of a benchmark random graph. So, small-worldness index of a network is obtained as  $\frac{C}{C_{rand}}$  where  $C_{rand}$  and  $L_{rand}$  are the mean clustering coefficient and the characteristic path length of the  $m$  random networks.  $M$  is the number of null networks generated for normalization of Clustering  $C$  and Path Length. We decided to use 100 null networks. In a small-world network, the clustering coefficient is significantly higher than that of random networks ( $\frac{C}{C_{rand}}$  ratio greater than 1) while the characteristic path length is comparable to random networks ( $\frac{L}{L_{rand}}$  ratio close to 1). The benchmark random networks are usually constructed using algorithms that preserve the topology of the graphs; we decided to preserve the degree distribution as the network of interest.

We extracted network measures using the codes developed in the Brain Connectivity Toolbox (BCT) [52]. Several network metrics including measures of network segregation (e.g. clustering), integration (e.g. path length, efficiency), centrality (e.g. nodal betweenness) are quantified. These metrics are quantified at both the network and regional level. We did plots of changes in global network measures as a function of network density. Association and adjacency matrices were also created (thresholded at  $D_{min}$ ) for each group network.

Modularity is a measure of network segregation and is quantified by subdividing the network into groups of regions that have maximal within group connections and minimal between-group links. A particular optimized algorithm called Louvain Method was used to find modular structures within a network. This algorithm is detailed described in the article of Blondel e Co. [53], and implemented in BCT. In order to characterize the degeneracy of the modularity structure adequately, the optimization algorithm runs several times (this number was set to 100). Then, the community structure with highest maximized modularity value is used as the representative modular structure.

**Louvain Method** This algorithm is divided in two main phases that are repeated iteratively (Figure 4.9).

Starting with a network of  $N$  nodes, first a different community is assigned to each node of the network. So, in this initial partition there are as many communities as there are nodes. Then, for each node  $i$  we consider the neighbours  $j$  of  $i$  and we evaluate the gain of modularity that would take place by removing  $i$

from its community and by placing it in the community of  $j$ . The node  $i$  is then placed in the community for which this gain is maximum (in case of a tie we use a breaking rule), but only if this gain is positive. If no positive gain is possible,  $i$  stays in its original community. This process is applied repeatedly and sequentially for all nodes until no further improvement can be achieved and the first phase is then complete. This first phase stops when a local maxima of the modularity is attained (when no individual move can improve the modularity). The second phase of the algorithm consists in building a new network whose nodes are now the communities found during the first phase.

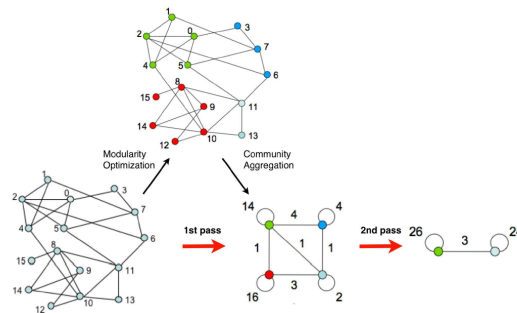


Figure 4.9: Louvain method. Each step is made of two phases: one where modularity is optimized by allowing only local changes of communities; one where the found communities are aggregated in order to build a new network of communities. The steps are repeated iteratively until no increase of modularity is possible.

## 4.5.2 Statistical analysis

### 4.5.2.1 Clinical data

To evaluate any statistical differences in distribution of sex, gender, number of MSA-C, MSA-P, and number of Stridor, No-stridor between groups, ANOVA and chi-square tests were performed depending on the type of variable, continuous or categorical [54].

### 4.5.2.2 Comparison of correlations matrices between groups

To test whether correlation of regional brain volumes was significantly different between groups, correlation coefficients were further converted into  $z$  values by using Fisher's  $r$ -to- $z$  transform [55] (Figure 4.10). This transformation generates values that were approximately normally distributed and a  $Z$  statistic 4.1 was then used to compare these transformed  $z$  values to determine the significance of the between-group differences in correlations.

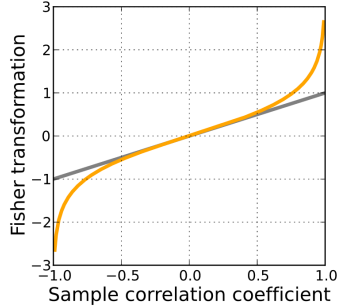


Figure 4.10: A graph of the transformation (in orange). The untransformed sample correlation coefficient is plotted on the horizontal axis, and the transformed coefficient is plotted on the vertical axis. The identity function (gray) is also shown for comparison

Once  $z$  values were obtained Z statistic was applied.

$$z = \frac{\left(\frac{1}{2} \ln \frac{1+r_1}{1-r_1}\right) + \left(\frac{1}{2} \ln \frac{1+r_2}{1-r_2}\right)}{\sqrt{\left(\frac{1}{n_1-3} + \frac{1}{n_2-3}\right)}} \quad (4.1)$$

Finally only the correlation coefficients with a p-value  $< 0.05$  were considered statistically significant.

#### 4.5.2.3 Comparison of network measures between groups

In order to test the statistical significance of the between-group differences in network topology and regional network measures, a nonparametric permutation test with 1000 repetitions is used [56]. In each repetition, the regional data of each participant are randomly reassigned to one of the two groups so that each randomized group had the same number of subjects as the original group. Then, an association matrix is obtained for each randomized group. The binary adjacency matrices are then estimated by applying the same thresholding procedure as described above. The network measures are then calculated for all the networks at each density. The differences in network measures between randomized groups (at each network density) are then calculated resulting in a permutation distribution of difference under the null hypothesis [57]. The actual between-group difference in network measures is then placed in the corresponding permutation distribution and a two-tailed p-value (0.05) is calculated based on its percentile position. For this statistical analysis we used a Matlab toolbox called Graph Analysis Toolbox (GAT) [58] which is based on Brain Connectivity Toolbox (BCT). Using GAT we also compared the areas under a curve (AUC) for each network measure. For this purpose, the curves extracted from thresholding across a range of densities are used.

Finally a module analysis was performed. We extracted different modules of regions from groups using Louvain method.

## 4.6 Network visualization

Network's visualization was performed using a specific tool of Matlab called BrainNet Viewer [59]. Each ROI is represented by one node whose world coordinate has been extracted from AAL atlas.

## Chapter 5

# Results

In this chapter the results for the six evaluated groups are shown: HC, MSA, No-stridor, Stridor, MSA-C and MSA-P. First of all we can see two table where the clinical variability is represented. Successively the results of comparison of correlations matrices between groups and topological parameters are shown.

### 5.1 Clinical variability

As we can see in Table 5.1 there are no significative difference in age, gender and percentage of MSA-C, MSA-P between No-stridor and Stridor groups.

	MSA		HC	ANOVA	chi-square
	Stridor	No-stridor			
n	14	22	27		
AAE (y) mean (SD)	61.6(8.9)	61.4(9.9)	56.7(10.1)	0.170	
SEX(M)	10(71%)	18(81.8%)	12(44.4%)		0.2
MSA-C	9(64.3%)	11(50%)			0.4

Table 5.1: No-stridor and Stridor vs HC clinical variability

In Table 5.2 we can see that there is a significative difference in gender distribution between MSA-C and MSA-P groups.

	MSA		HC	ANOVA	chi-square
	MSA-C	MSA-P			
n	20	16	27		
AAE (y) mean (SD)	60.4(8.7)	62.8(10.3)	56.7(10.1)	0.129	
SEX(M)	14(70%)	14(87.5%)	12(44.4%)		0.014
Stridor	9(45%)	5(31.3%)			0.400

Table 5.2: MSA-C and MSA-P vs HC clinical variability

## 5.2 Comparison of correlations matrices between groups

### 5.2.1 Correlation analysis

Pearson correlation coefficient was used to measure the association between volume of every couple of regions. In Figures 5.1 5.2 5.3, 5.4, 5.5 and 5.6 are shown the distributions of correlation coefficients for the groups considered in this study.

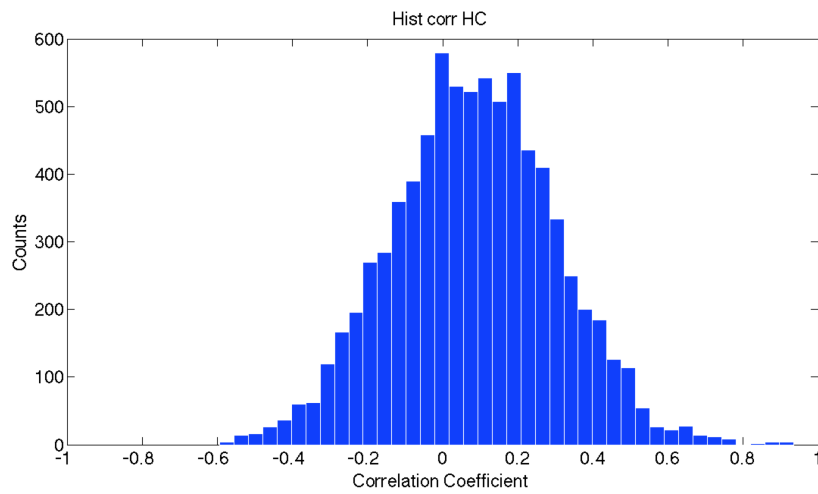


Figure 5.1: Histogram of correlation coefficients for HC group

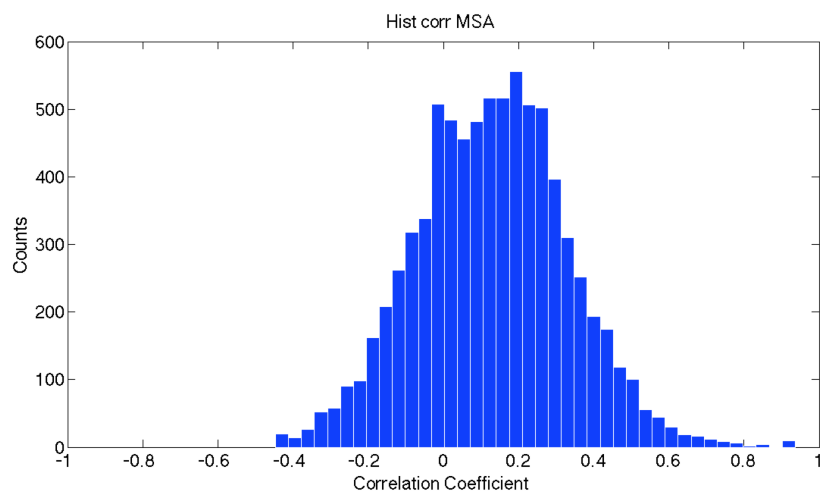


Figure 5.2: Histogram of correlation coefficients for MSA group

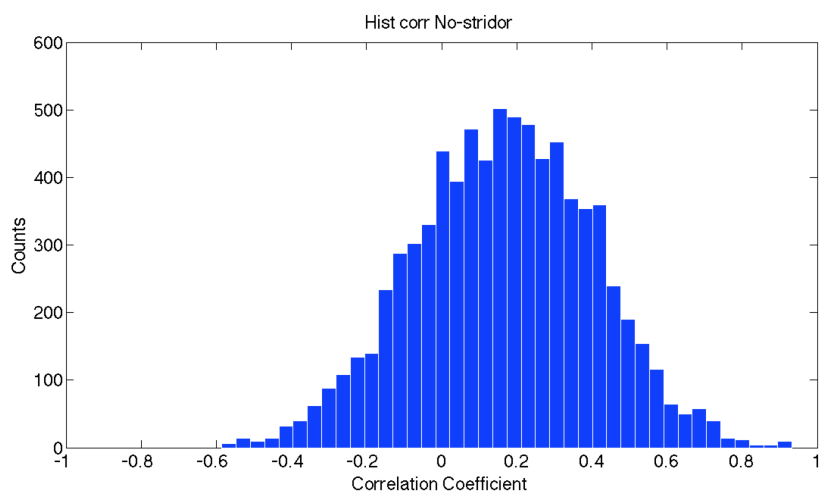


Figure 5.3: Histogram of correlation coefficients for No-stridor group

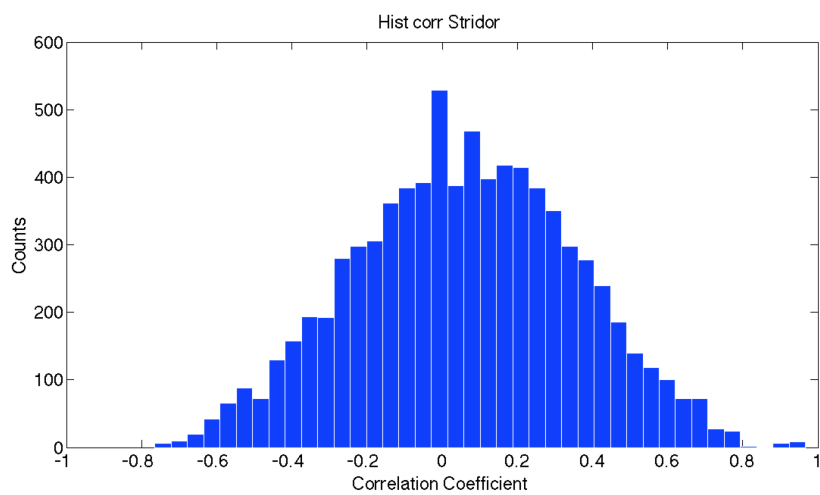


Figure 5.4: Histogram of correlation coefficients for Stridor group

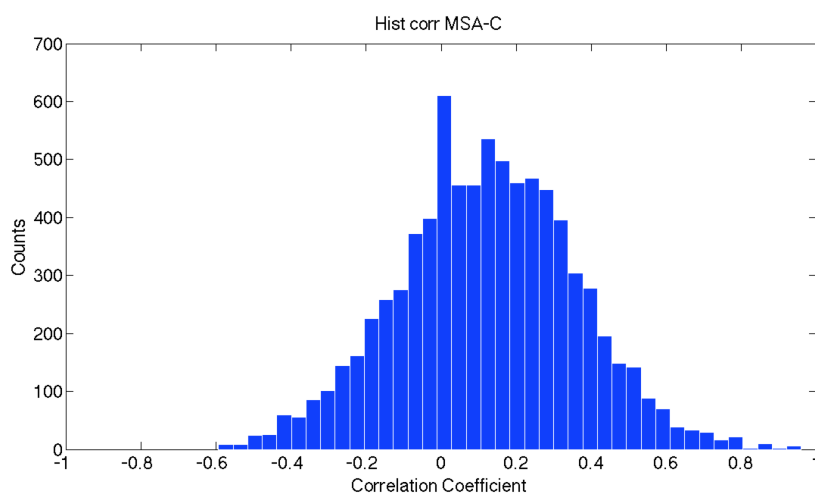


Figure 5.5: Histogram of correlation coefficients for MSA-C group

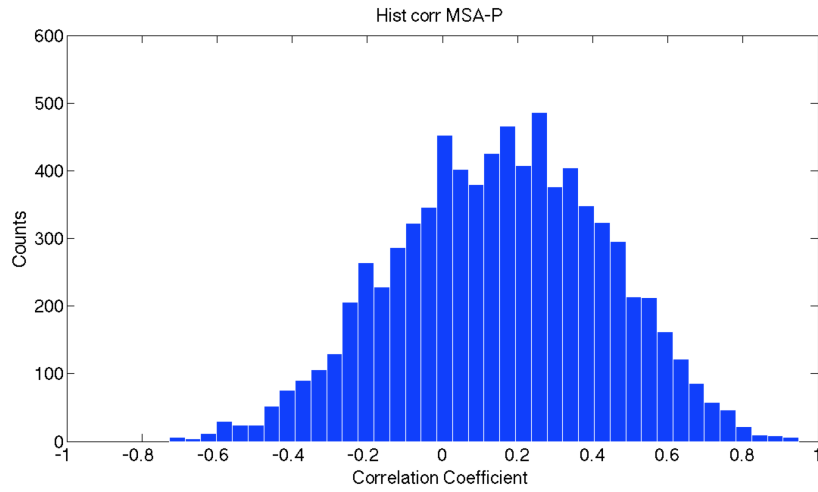


Figure 5.6: Histogram of correlation coefficients MSA-P group

We were also interested in the significance of these correlations, so we analyzed and plotted the distributions of the p values of the correlations seen before. The distribution of p values of the correlation coefficients of groups in the study are shown in Figures 5.7, 5.8, 5.9, 5.10, 5.11 and 5.12.

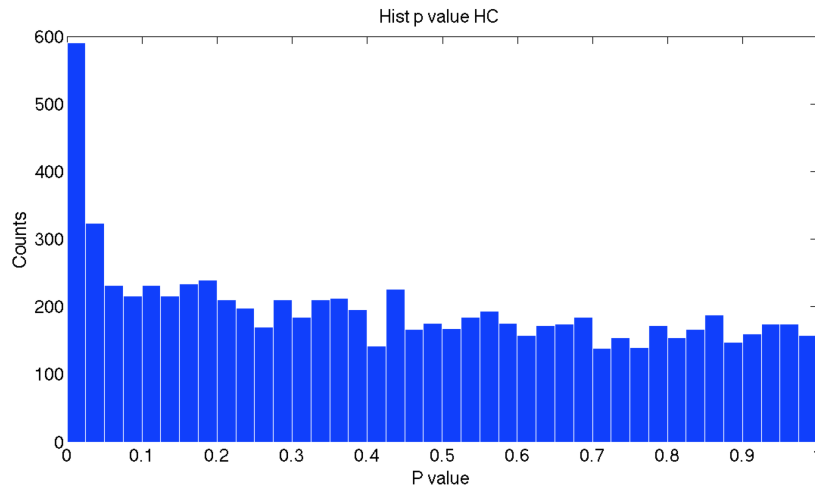


Figure 5.7: Histogram of p values distribution in healthy controls

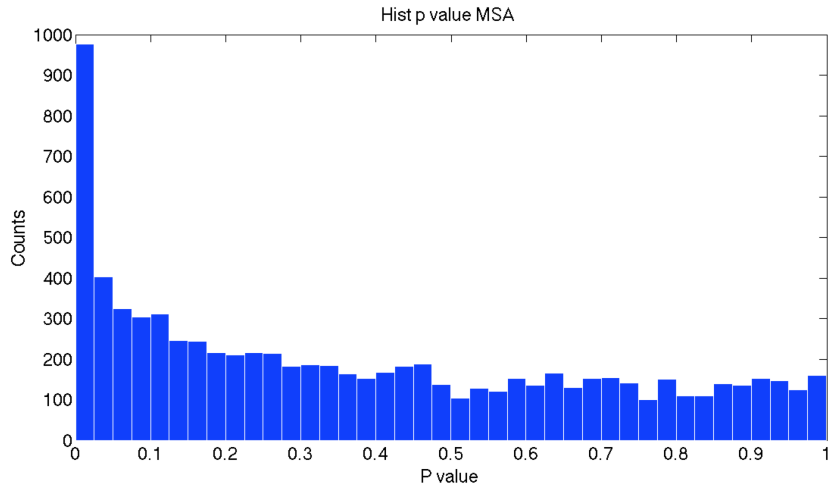


Figure 5.8: Histogram of p values distribution in MSA

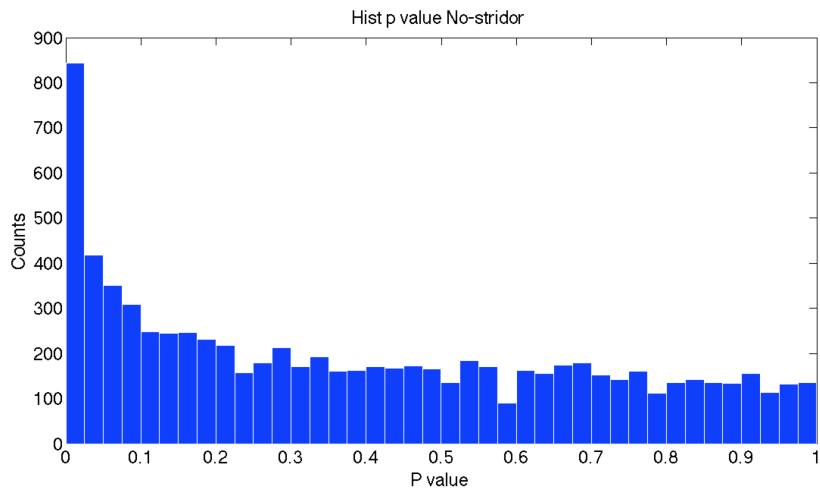


Figure 5.9: Histogram of p values distribution in No-stridor

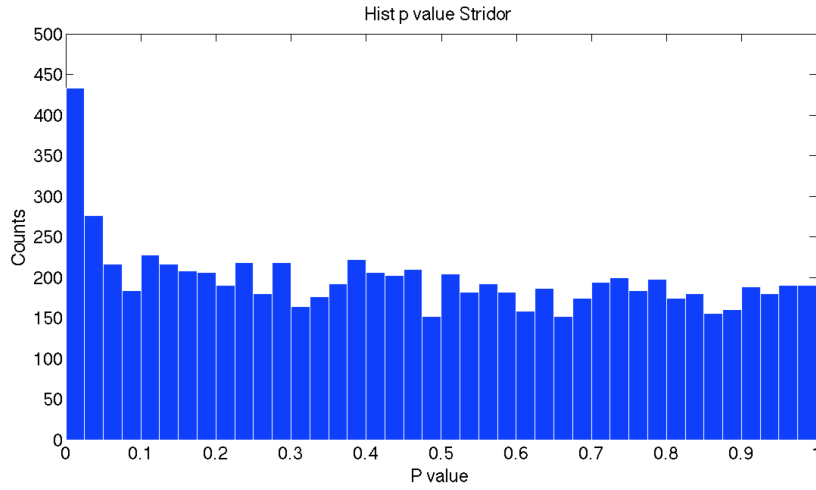


Figure 5.10: Histogram of p values distribution in Stridor

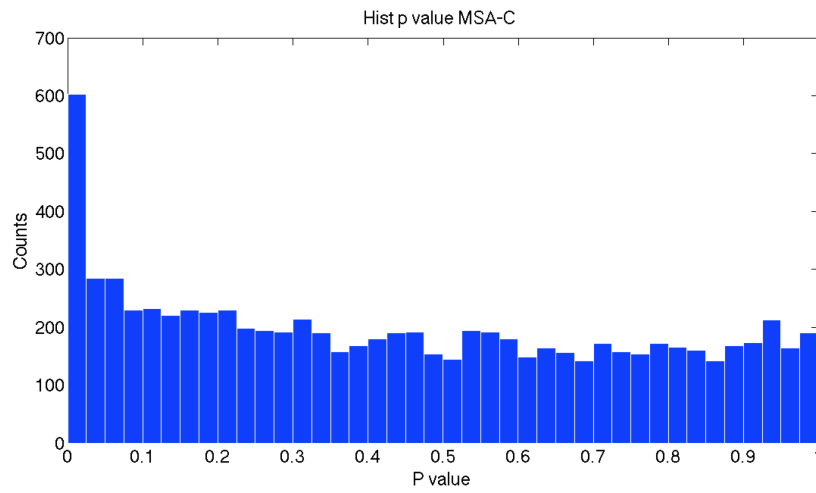


Figure 5.11: Histogram of p values distribution in MSA-C

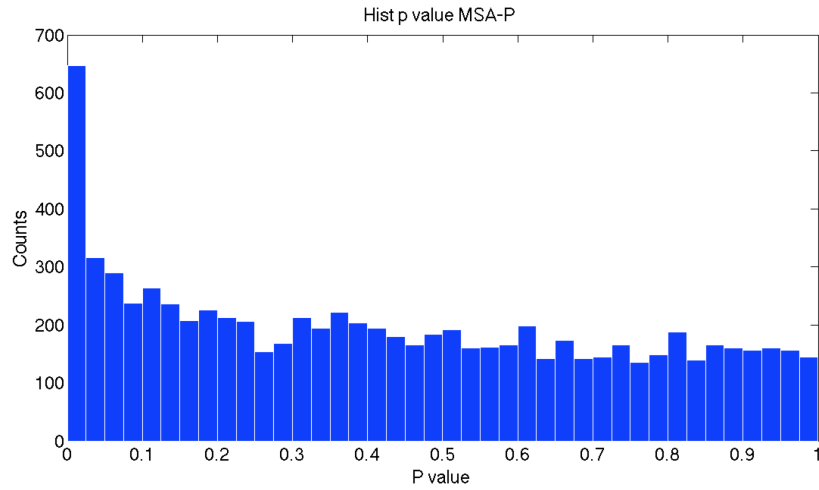


Figure 5.12: Histogram of p values distribution in MSA-P

In Figures 5.13, 5.14, 5.15, 5.16 5.17 and 5.18 matrices of correlation coefficient for the different groups are represented. In every correlation matrices are represented the volumetric correlation between the  $i$ -th and  $j$ -th region segmented. These regions are ordinated from sub-cortical regions to cortical regions and ends with sub-tentorial regions as reported in Tables 4.3, 4.4 and 4.5.

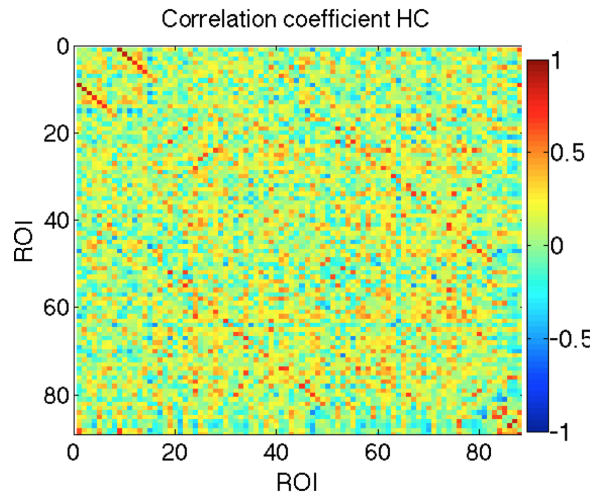


Figure 5.13: Correlation coefficient matrix for HC

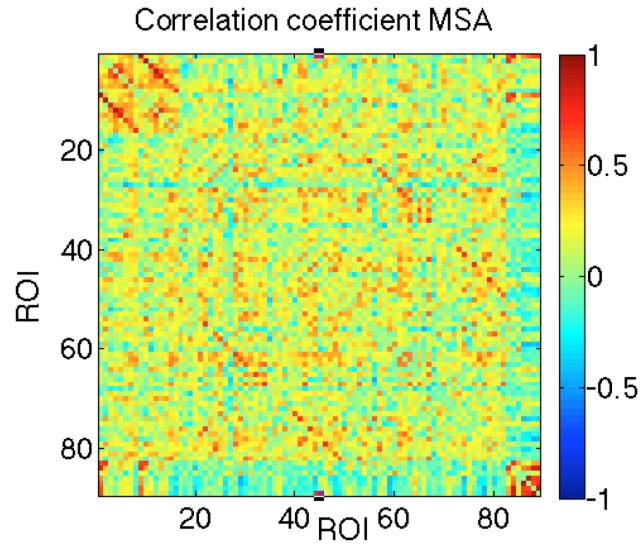


Figure 5.14: Correlation coefficient matrix for MSA

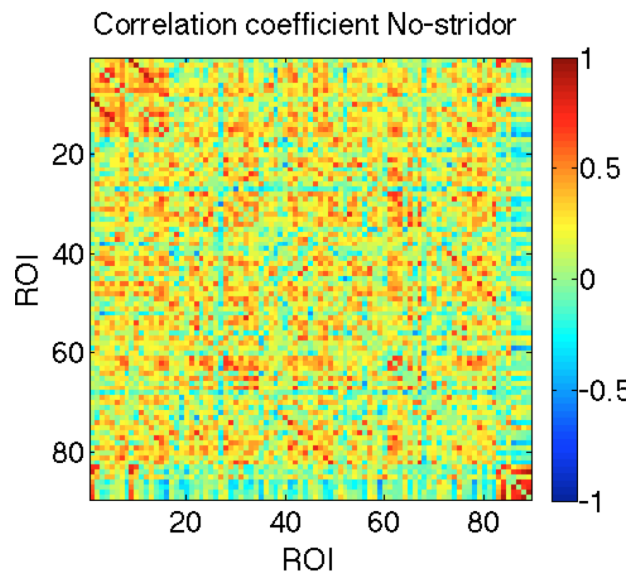


Figure 5.15: Correlation coefficient matrix for No-stridor

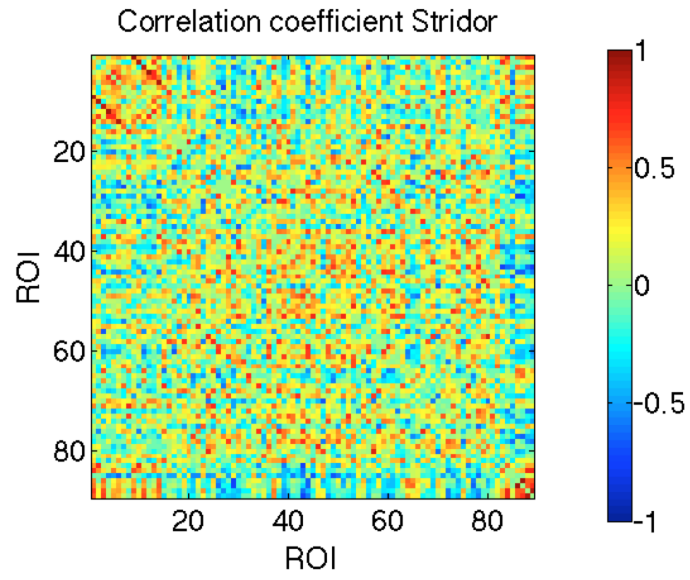


Figure 5.16: Correlation coefficient matrix for Stridor

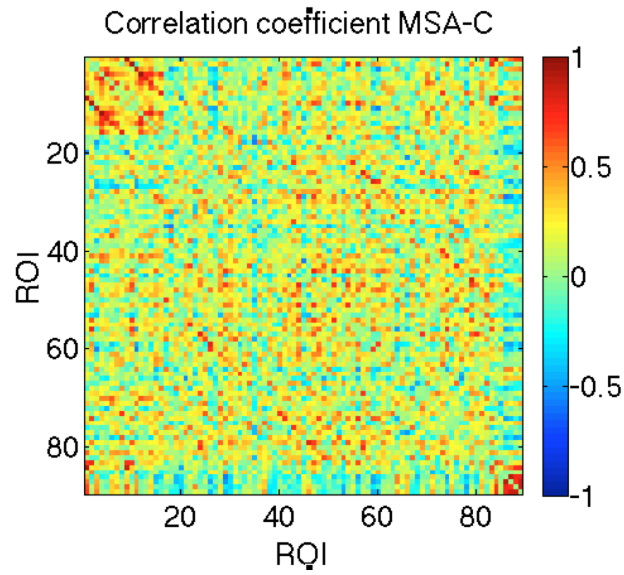


Figure 5.17: Correlation coefficient matrix for MSA-C

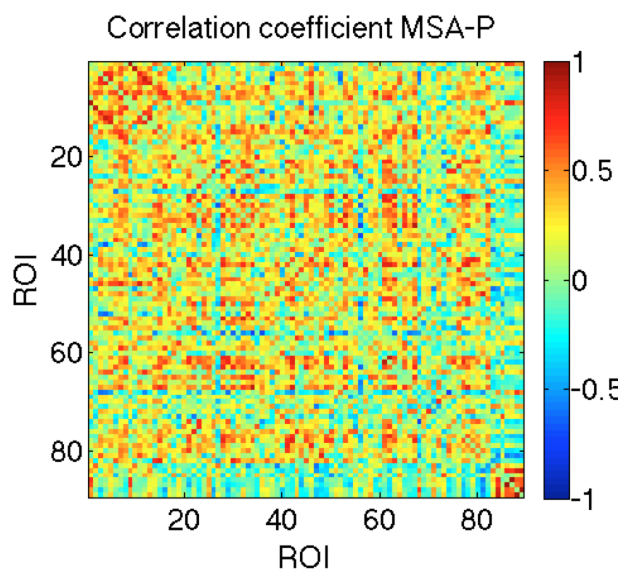


Figure 5.18: Correlation coefficient matrix for MSA-P

From these figures it is possible to see that cells with high correlation are represented by the same regions of both hemisphere, as we expect anatomically.

### 5.2.2 False discovery rate matrices

Successively, we evaluated which regions have a significant correlation coefficient ( $p\text{-value} < 0.05$ ). To adjust for the multiple comparisons, a false discovery rate (FDR) procedure was performed at a  $q$  value of 0.05. Brain regions with significant correlation coefficient are shown as a white cell in the following matrices Figure 5.19, 5.20 and 5.21

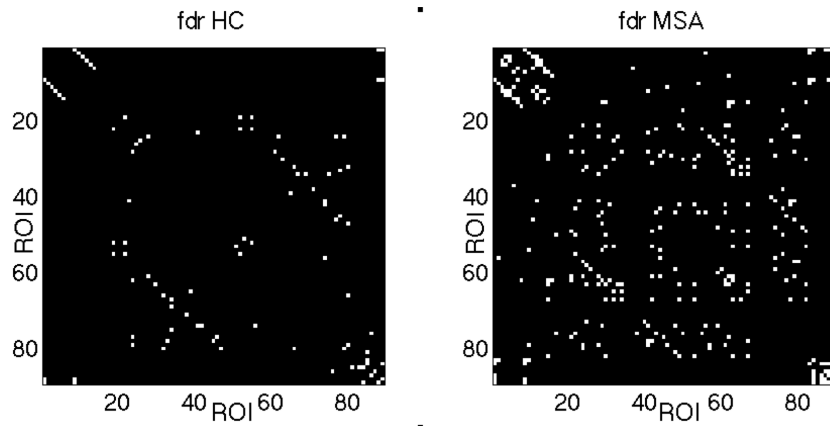


Figure 5.19: Matrices of HC and MSA, white cells represent regions with a significant correlation coefficient after FDR

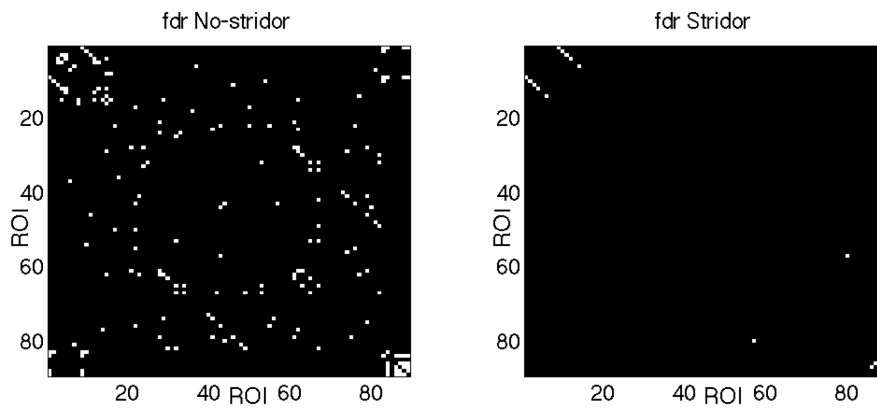


Figure 5.20: Matrices of No-stridor and Stridor groups, white cells represent regions with a significant correlation coefficient after FDR

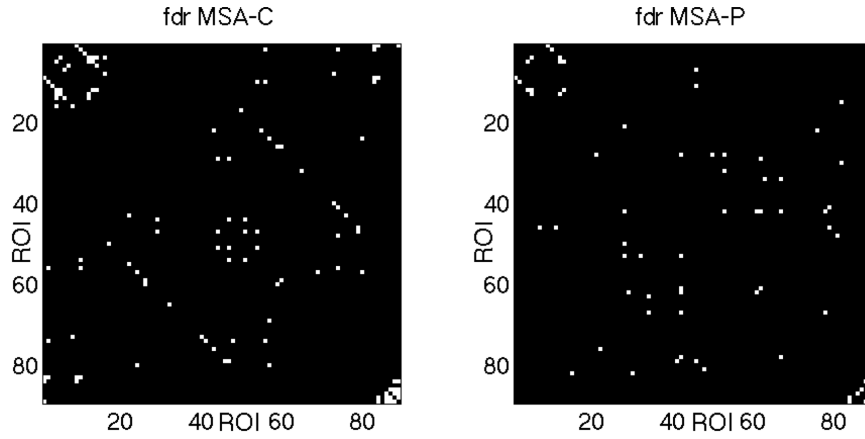


Figure 5.21: Matrices of MSA-C and MSA-P groups, white cells represent regions with a significant correlation coefficient after FDR

A qualitative analysis suggests us that using the correlation coefficient for this study was a good choice. We can assume this by the fact that many regions in the right hemisphere correlate with the same region in the left hemisphere. In Table 5.3 we can see an example of regions of the right hemisphere that correlate with the same region in the left hemisphere in HC.

Regions	
'Right-Cerebellum-Cortex'	'Left-Cerebellum-Cortex'
'Right-Thalamus-Propor'	'Left-Thalamus-Propor'
'Right-Caudate'	'Left-Caudate'
'Right-Putamen'	'Left-Putamen'
'Right-Pallidum'	'Left-Pallidum'
'Right-Hippocampus'	'Left-Hippocampus'
'Right-cuneus'	'Left-cuneus'
'Right-pericalcarine'	'Left-pericalcarine'
'Right-postcentral'	'Left-postcentral'
'Right-middletemporal'	'Left-middletemporal'
'Right-inferiortemporal'	'Left-inferiortemporal'
'Right-lateraloccipital'	'Left-lateraloccipital'
'Right-insula'	'Left-insula'
'Right-inferiorparietal'	'Left-inferiorparietal'
'Right-superiorfrontal'	'Left-superiorfrontal'
'Right-SCP'	'Left-SCP'
'Right-MCP'	'Left-MCP'

Table 5.3: Correlation between regions after FDR in HC

Using the CLR algorithm we lost the correlation between in the right hemisphere with the same region in the left hemisphere. In Figures 5.22, 5.23 and are shown the correlation matrices performed with CLR after FDR correction.

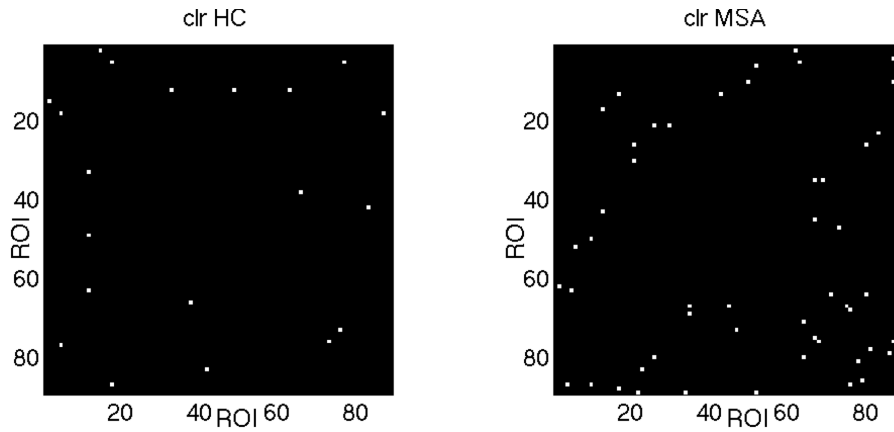


Figure 5.22: Matrices of HC and MSA, white cells represent regions with a significant CLR after FDR

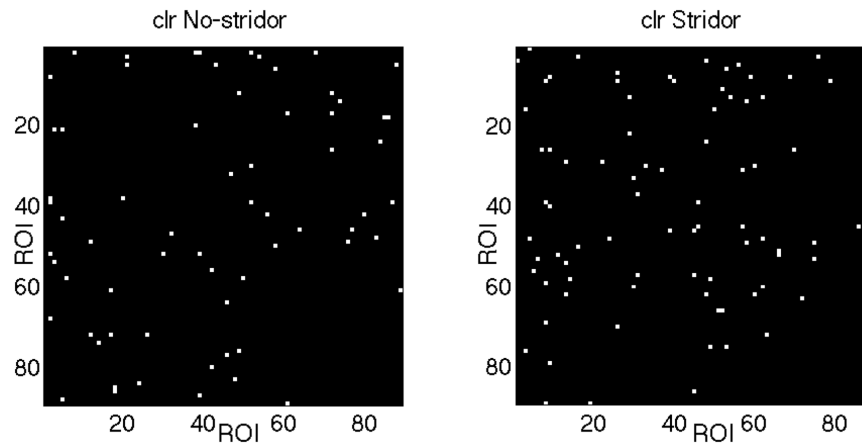


Figure 5.23: Matrices of No-stridor and Stridor groups, white cells represent regions with a significant CLR after FDR

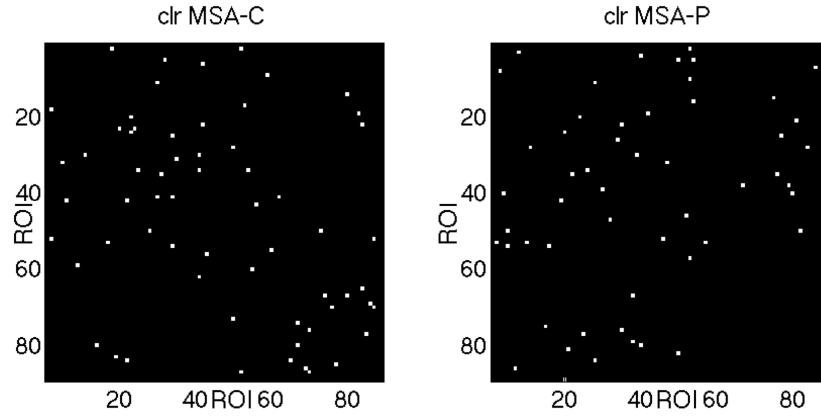


Figure 5.24: Matrices of MSA-C and MSA-P groups, white cells represent regions with a significant CLR after FDR

### 5.2.3 Z-Statistic

No statistical differences between groups in correlation matrices after FDR correction were found.

## 5.3 Topological parameters and group analysis

Topological parameters are divided into two main groups: those related to the entire network and those related to a specific node. We first calculated the number of the connected components for every networks in order to understand which is the minimum density  $D_{min}$  in which all nodes become fully connected in the brain networks. Successively, we started to analyze differences between groups.

### 5.3.1 Connected components

The trend of the connected component for every groups is shown in Figures 5.25, 5.26, 5.27, 5.28, 5.29 and 5.30

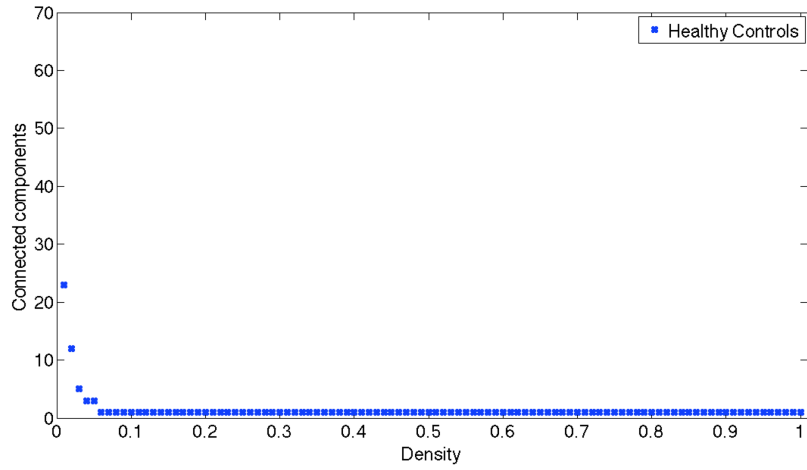


Figure 5.25: Connected components as function of density in healthy controls

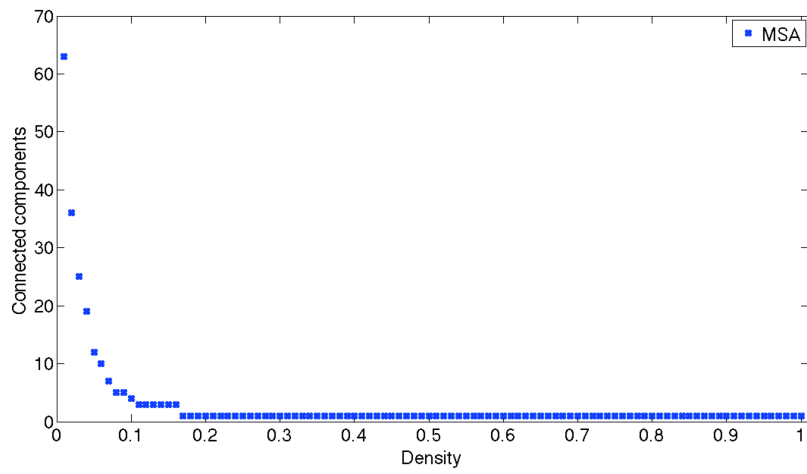


Figure 5.26: Connected components as function of density in MSA

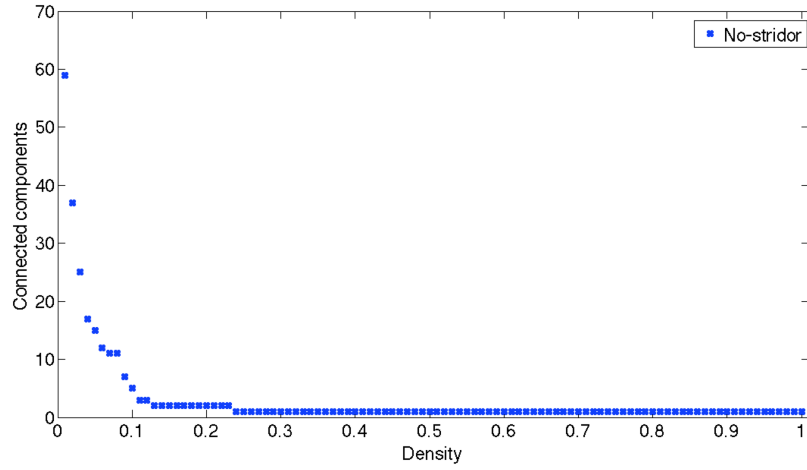


Figure 5.27: Connected components as function of density in No-stridor group

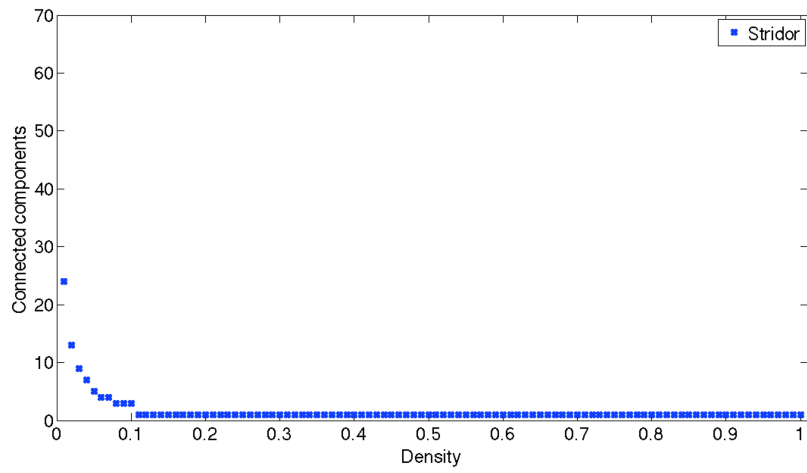


Figure 5.28: Connected components as function of density in Stridor

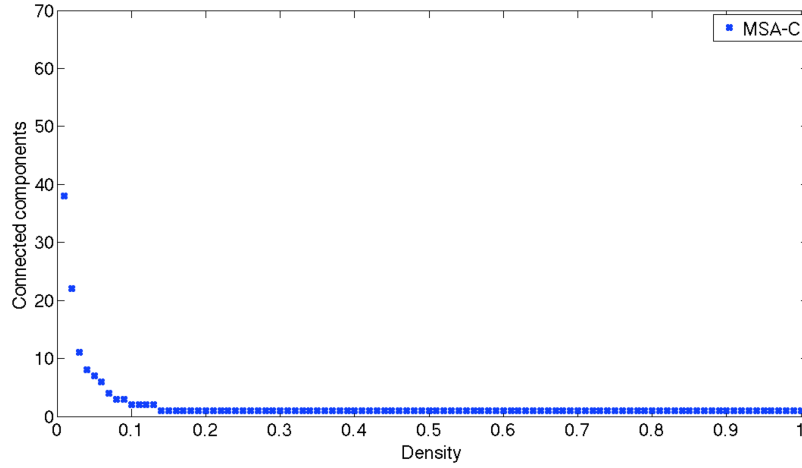


Figure 5.29: Connected components as function of density in MSA-C

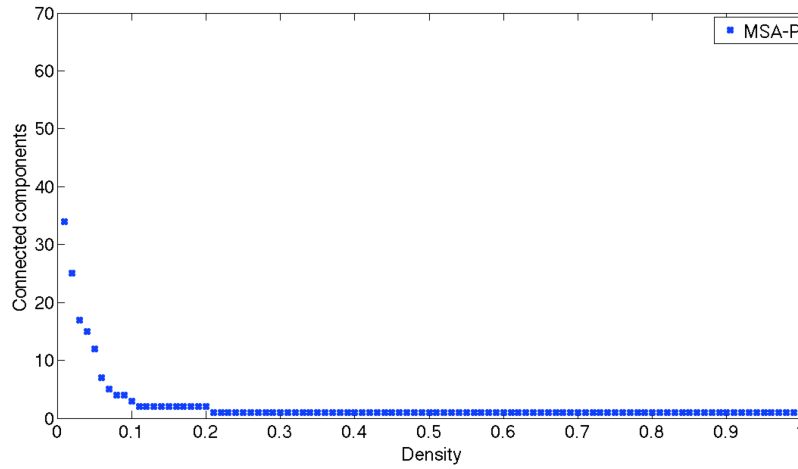


Figure 5.30: Connected components as function of density in MSA-P

We can finally summarize the minimum density in which groups are full connected in the following Table 5.4.

	HC	MSA	No-stridor	Stridor	MSA-C	MSA-P
Density	0.07	0.16	0.22	0.11	0.13	0.21

Table 5.4: Graph density for connected components equal to 1

From these results we decided to choose 0.1 as  $D_{min}$  to perform the analysis across density.

### 5.3.2 Comparison between groups across density

In this section the results of comparison between groups across density from 0.1 to 0.45 as said before are shown. For every group comparison, the values of different topological measures and between group differences with a 95% confidence intervals as a function of network density are plotted.

In Table 5.5 we can see the measures calculated in this study.

Measures
Path L
Clustering C
Normalized Path L
Normalized Clustering C
Small-world
Global Efficiency
Mean Local Efficiency
Mean Node Betweenness
Modularity

Table 5.5: List of measures plotted across density. Lambda is the normalized path length; Gamma is the normalized clustering coefficient; Sigma is the Small-worldness

#### 5.3.2.1 Healthy controls vs MSA

In this section are plotted the comparison between groups across density for HC vs MSA. No statistically significant difference was found in measures calculated.

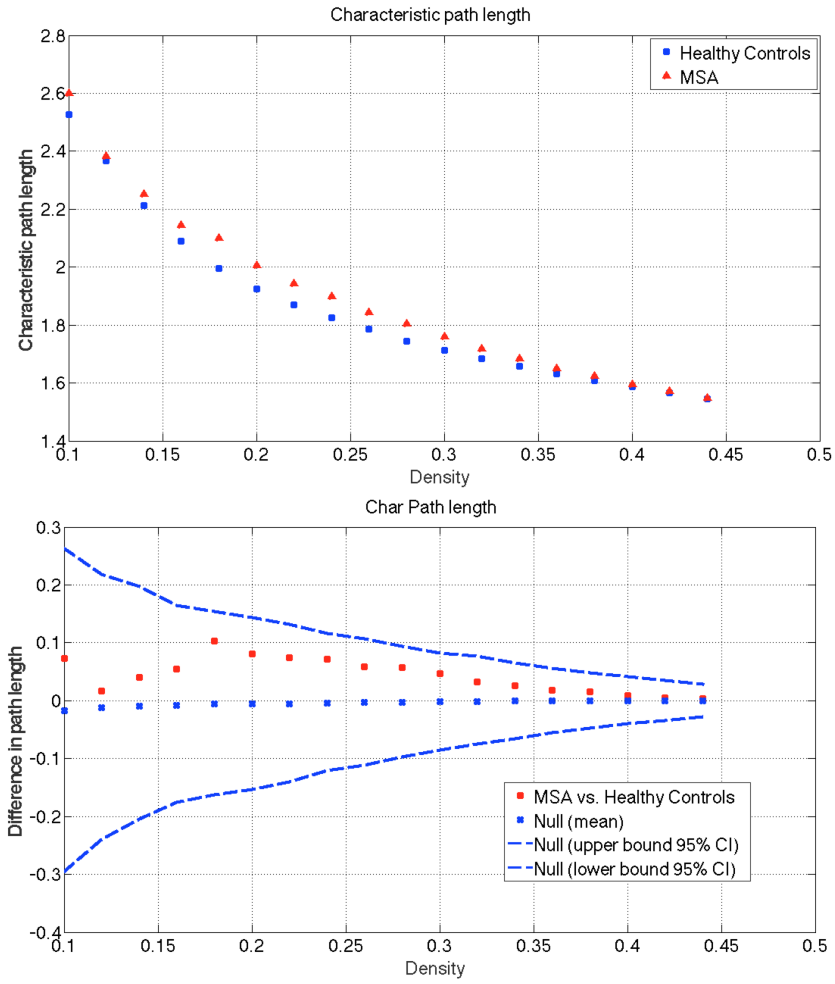


Figure 5.31: Characteristic Path L and difference in Characteristic Path L for HC and MSA groups

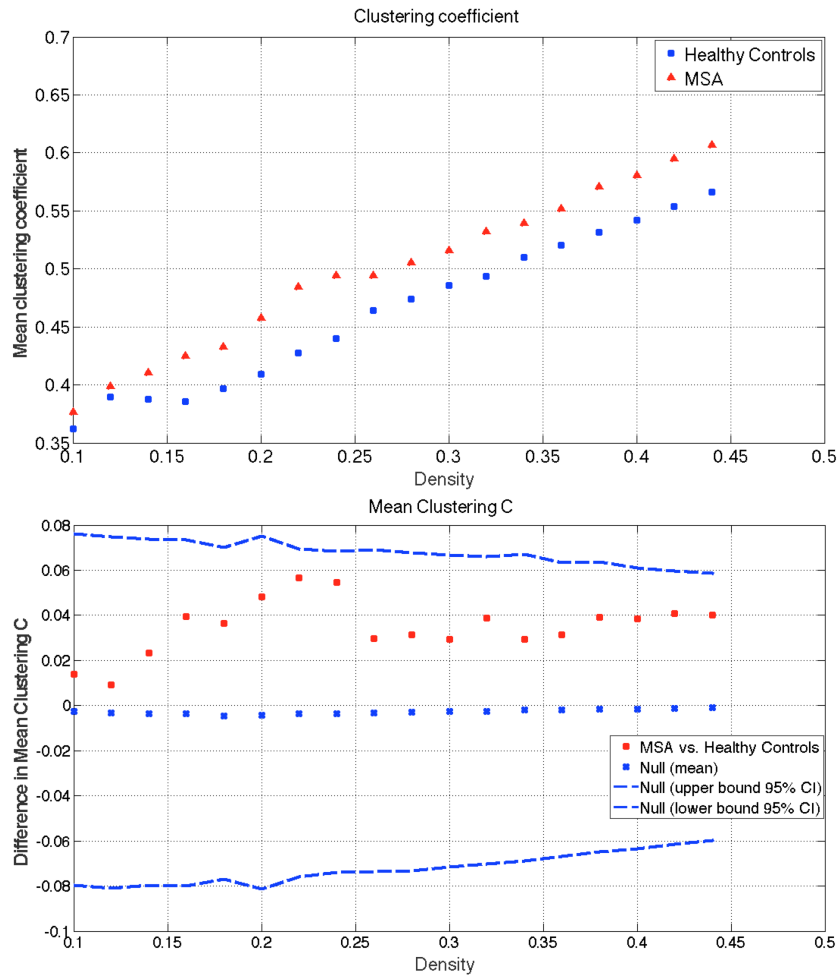


Figure 5.32: Mean Clustering C and difference in Mean Clustering C for HC and MSA groups

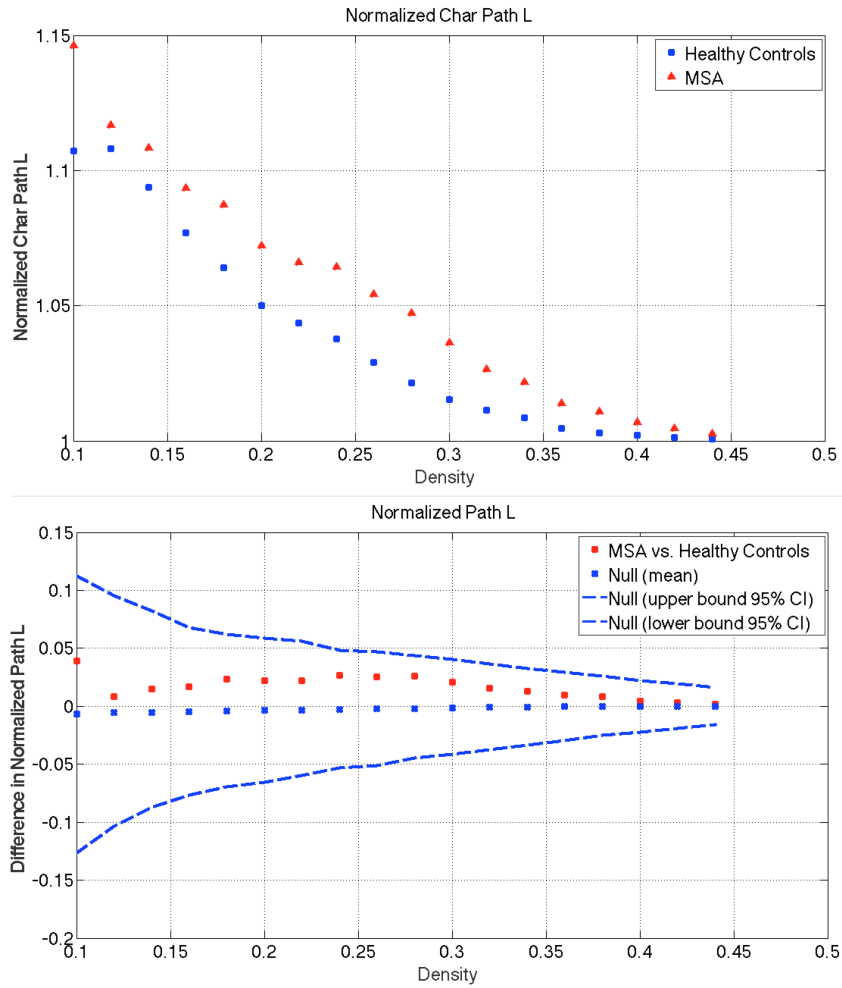


Figure 5.33: Normalized Path L and difference in Normalized Path L for HC and MSA groups

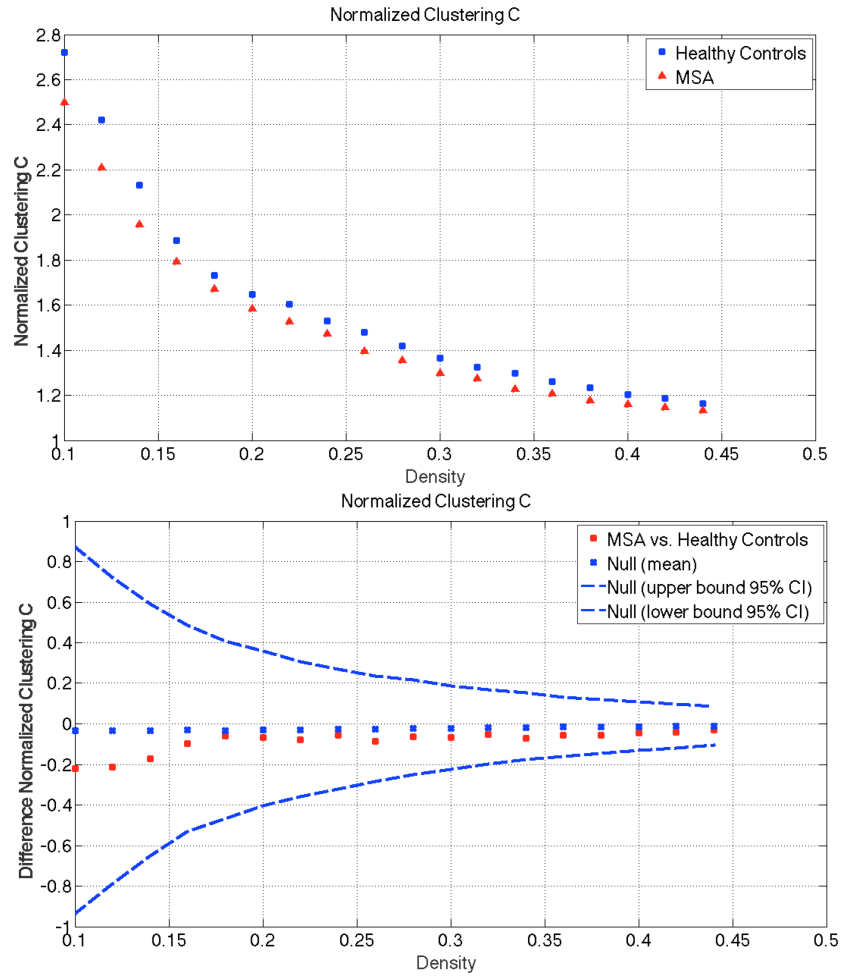


Figure 5.34: Normalized Clustering C and difference in Normalized Clustering C for HC and MSA groups

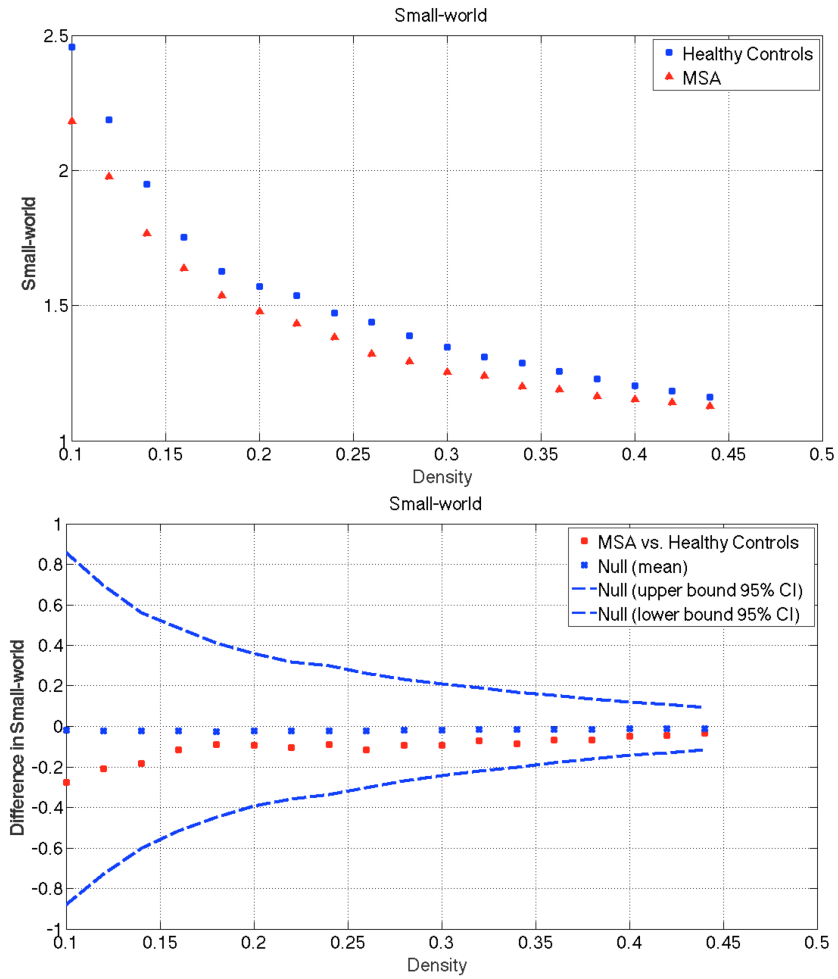


Figure 5.35: Small-world and difference in Small-world for HC and MSA groups

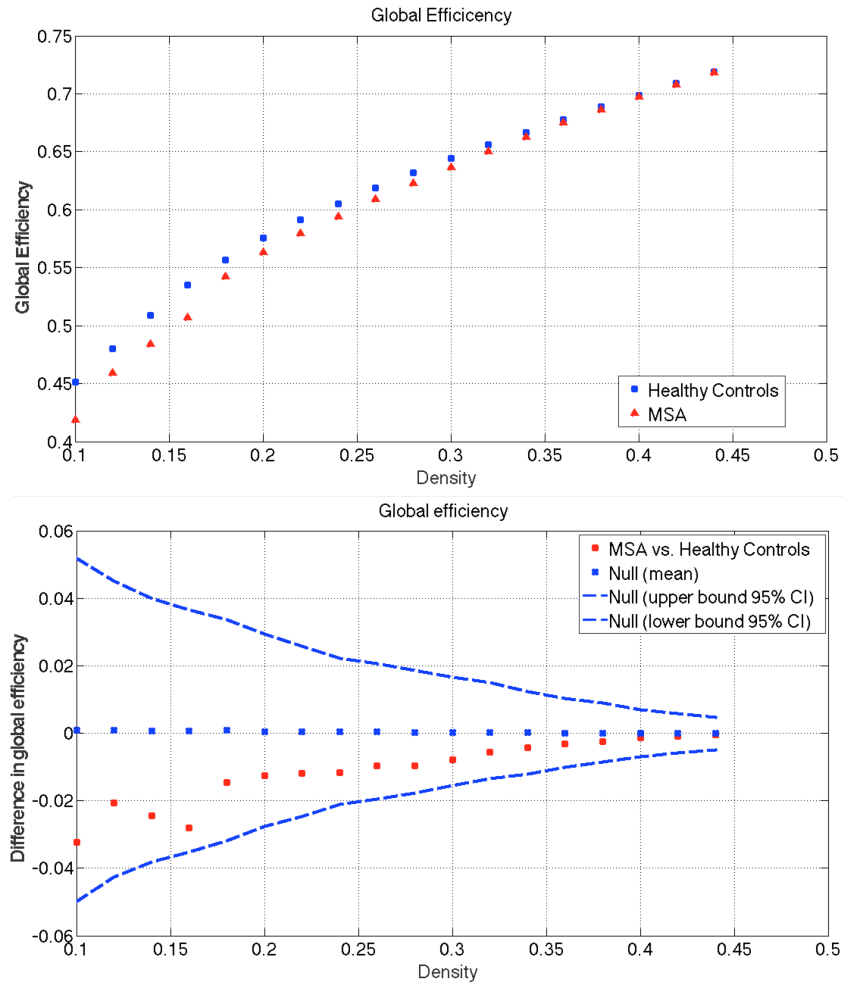


Figure 5.36: Global efficiency and difference in Global efficiency for HC and MSA groups

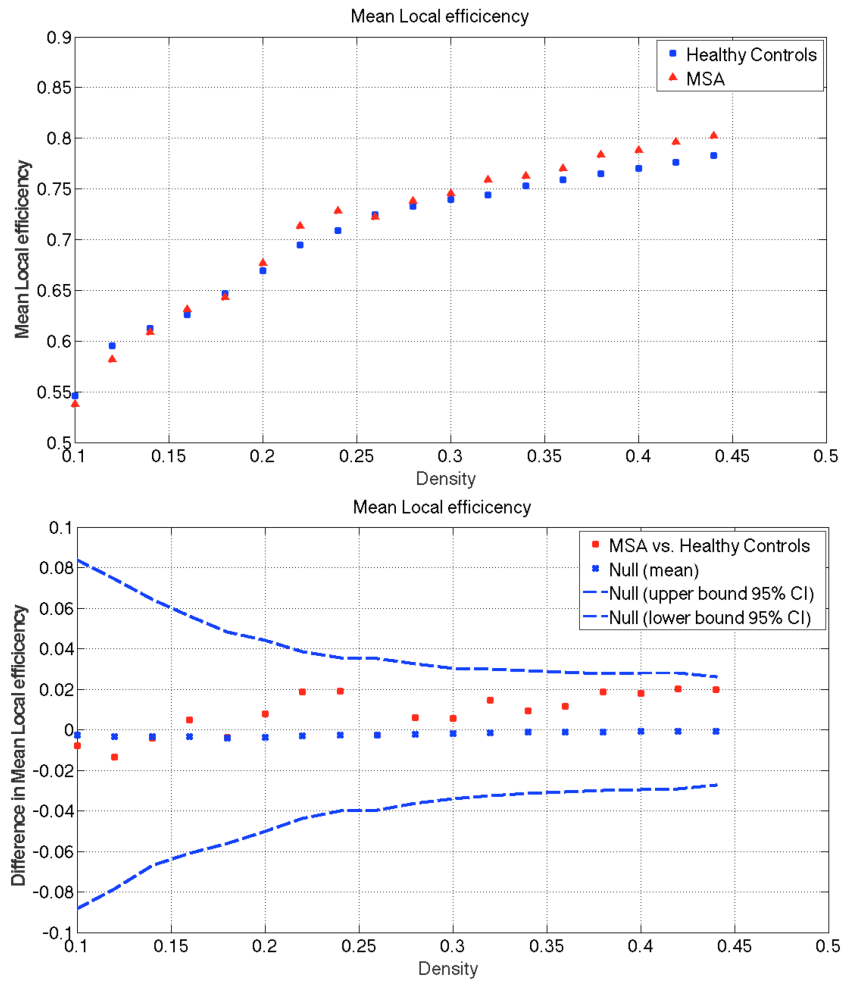


Figure 5.37: Mean Local efficiency and difference in Mean Local efficiency for HC and MSA groups

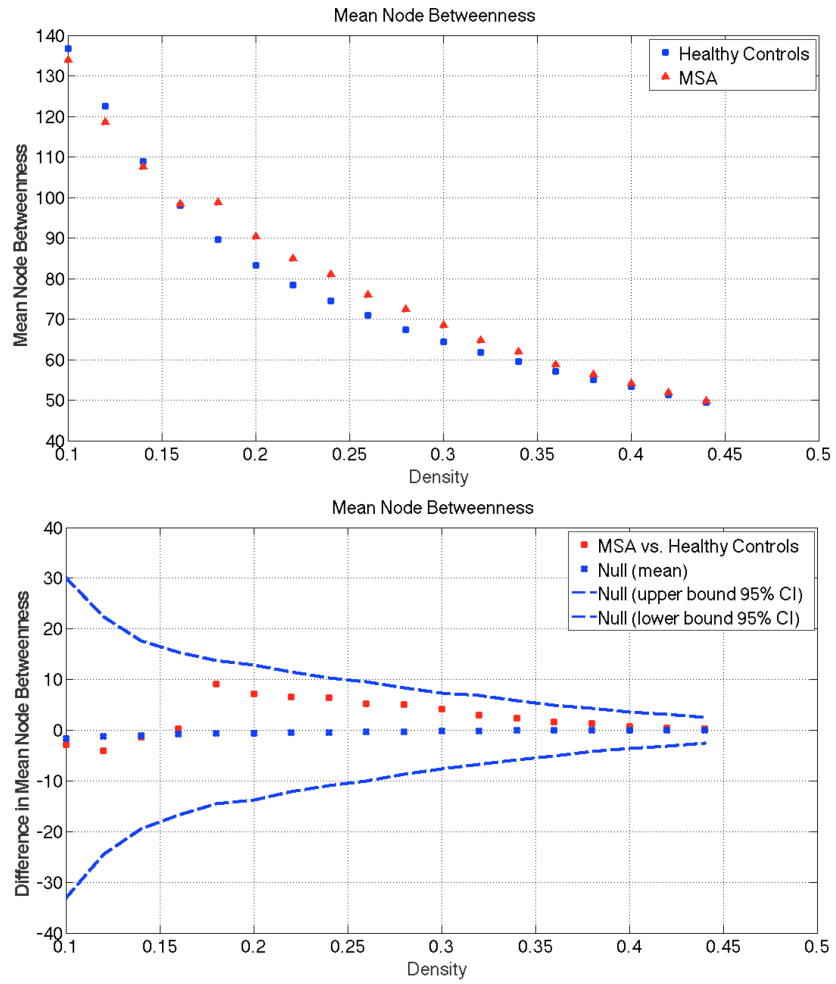


Figure 5.38: Mean Node Betweenness and difference in Mean Node Betweenness for HC and MSA groups

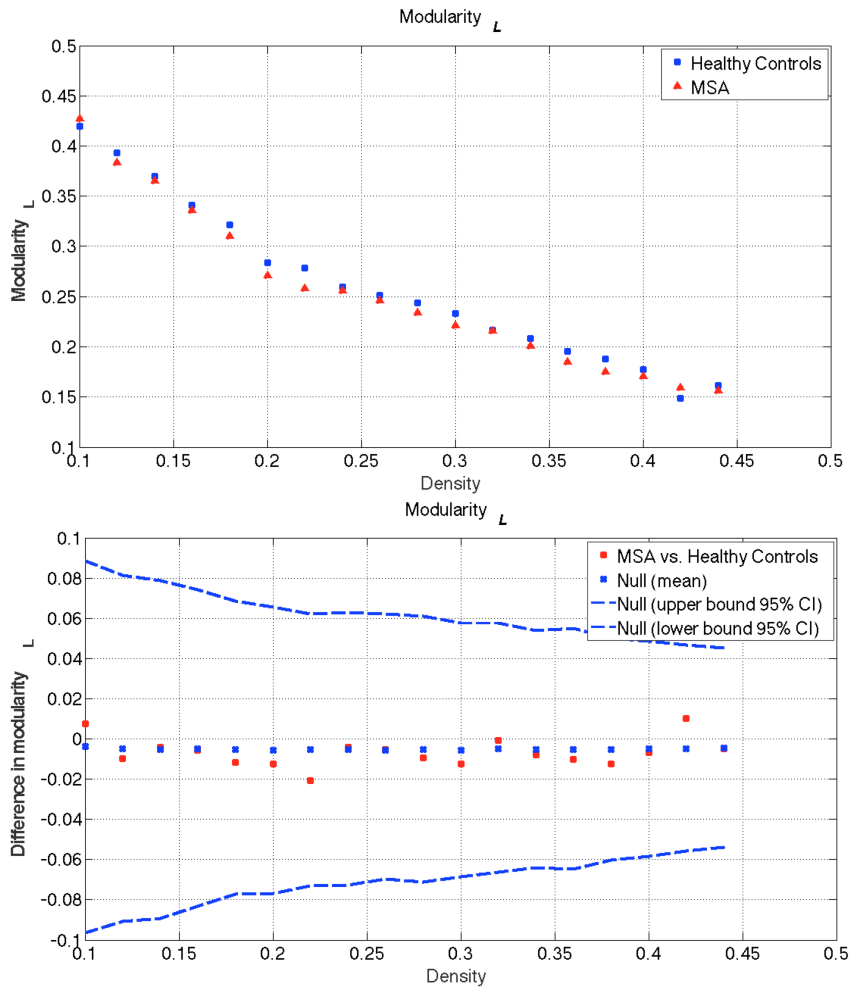


Figure 5.39: Modularity Louvain and difference in Modularity Louvain for HC and MSA groups

### 5.3.2.2 No-stridor vs Stridor

In this section the comparison between groups across density for No-stridor vs Stridor are plotted. No statistically significant difference was found in measures calculated.

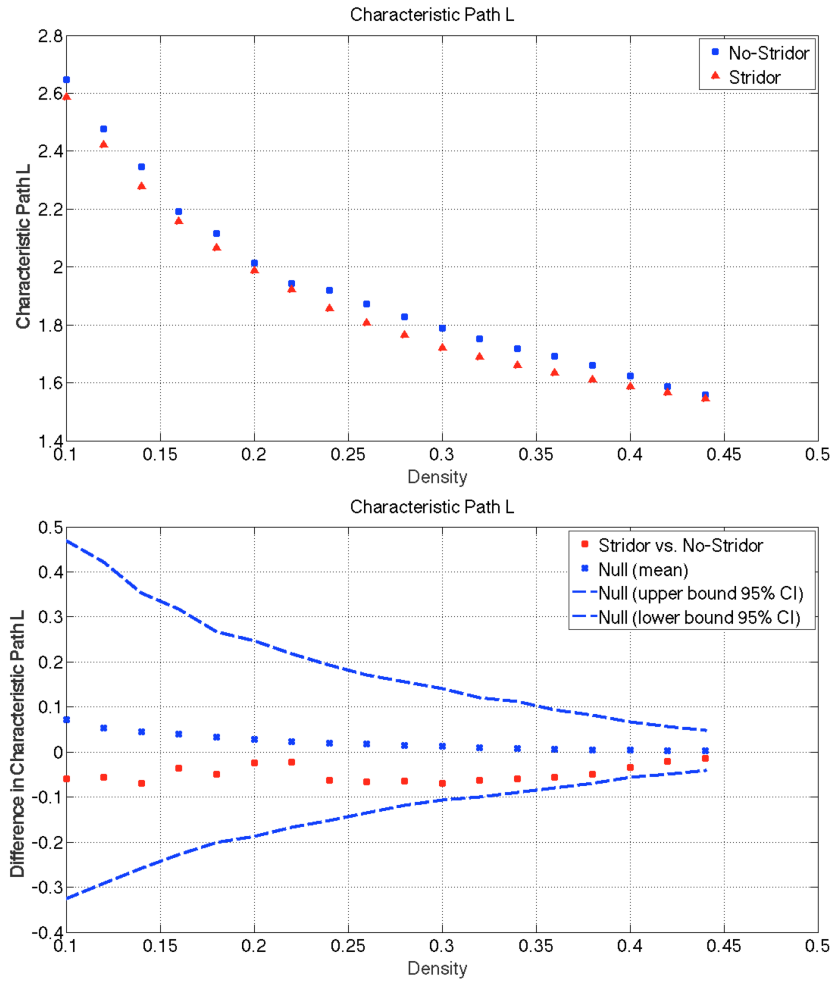


Figure 5.40: Characteristic Path L and difference in Characteristic Path L for No-stridor and Stridor groups

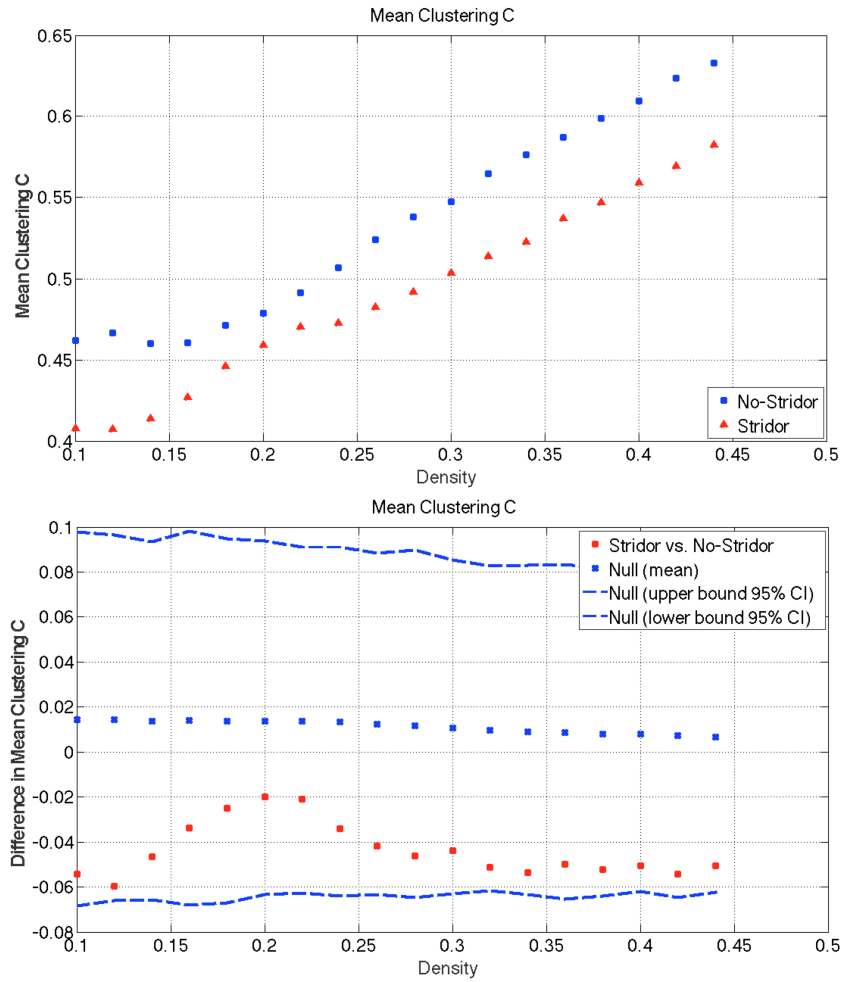


Figure 5.41: Mean Clustering C and difference in Mean Clustering C for No-stridor and Stridor groups

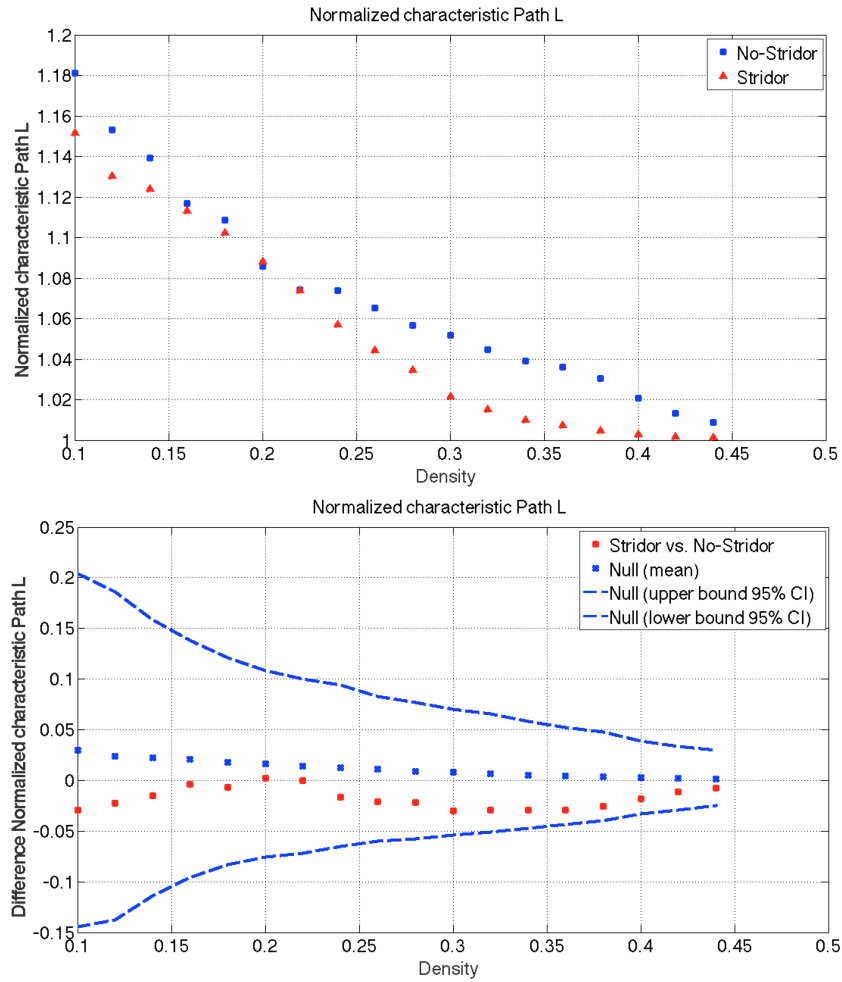


Figure 5.42: Normalized characteristic Path L and difference in Normalized characteristic Path L for No-stridor and Stridor groups

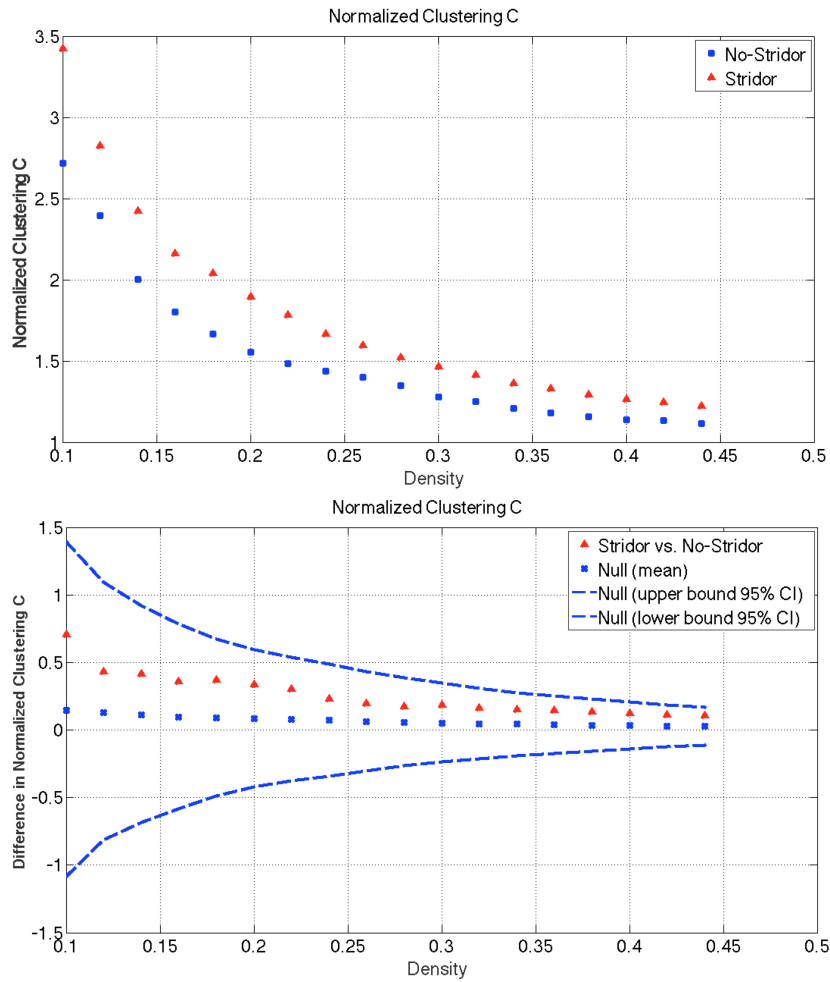


Figure 5.43: Normalized Clustering C and difference in Normalized Clustering C for No-stridor and Stridor groups

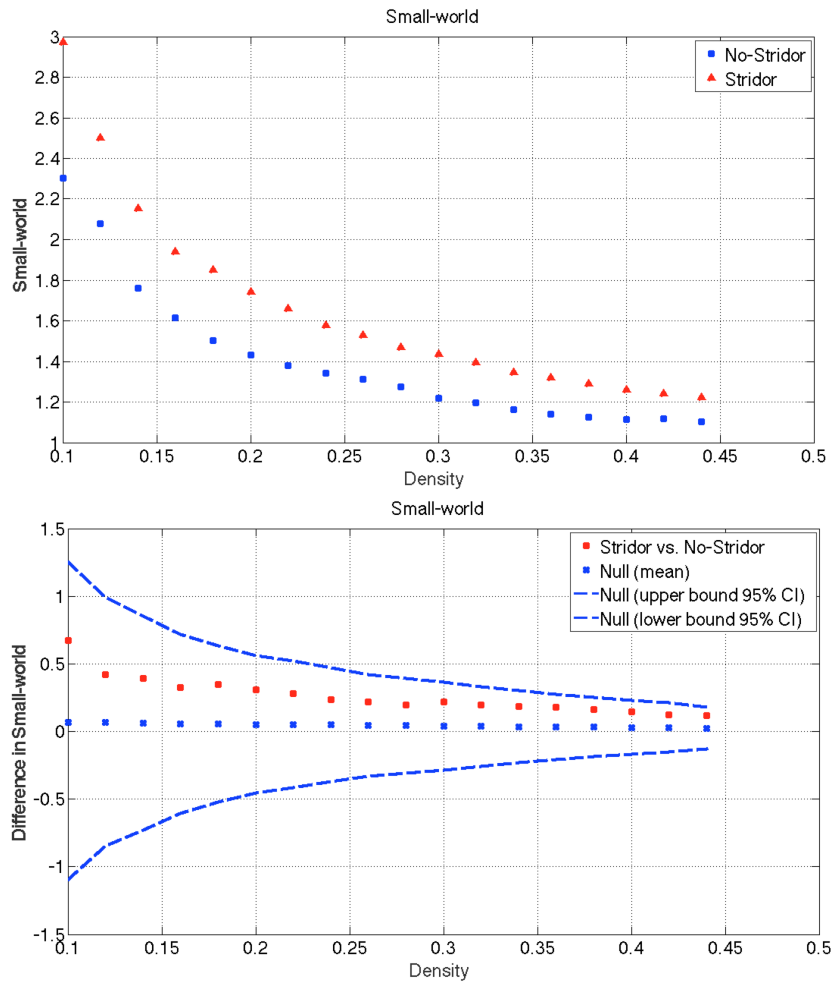


Figure 5.44: Small-world and difference in Small-world for No-stridor and Stridor groups

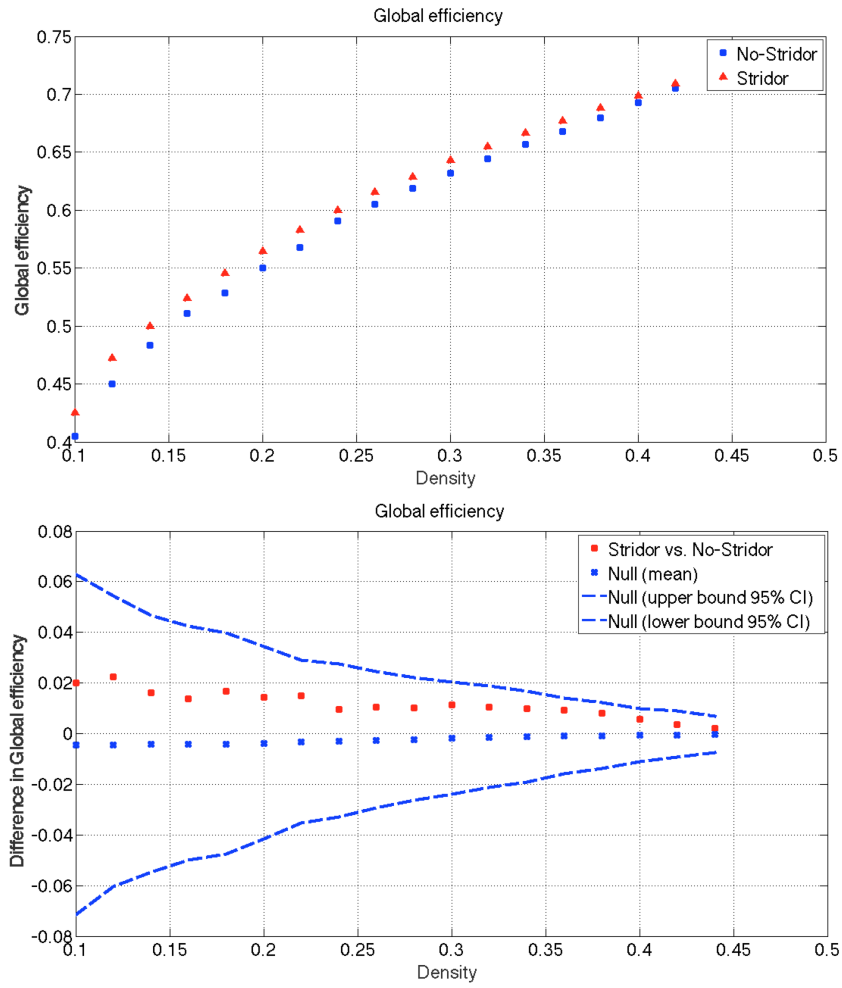


Figure 5.45: Global efficiency and difference in Global efficiency for No-stridor and Stridor groups

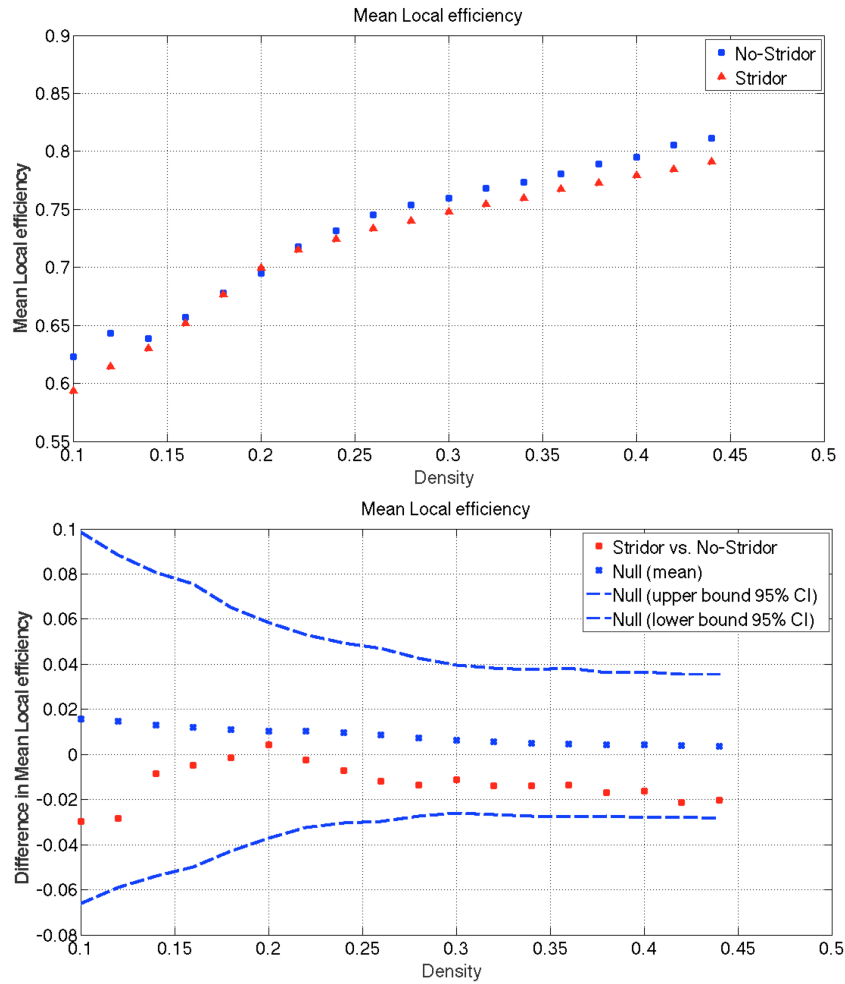


Figure 5.46: Mean Local efficiency and difference in Mean Local efficiency for No-stridor and Stridor groups

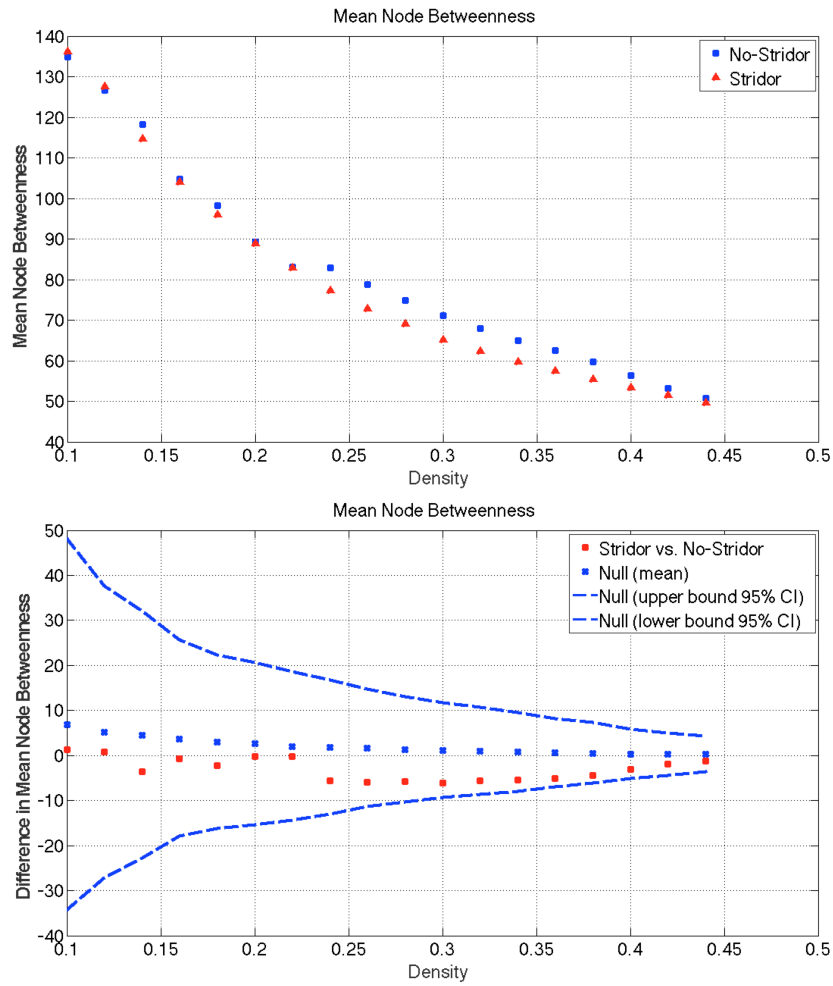


Figure 5.47: Mean Node Betweenness and difference in Mean Node Betweenness for No-stridor and Stridor groups

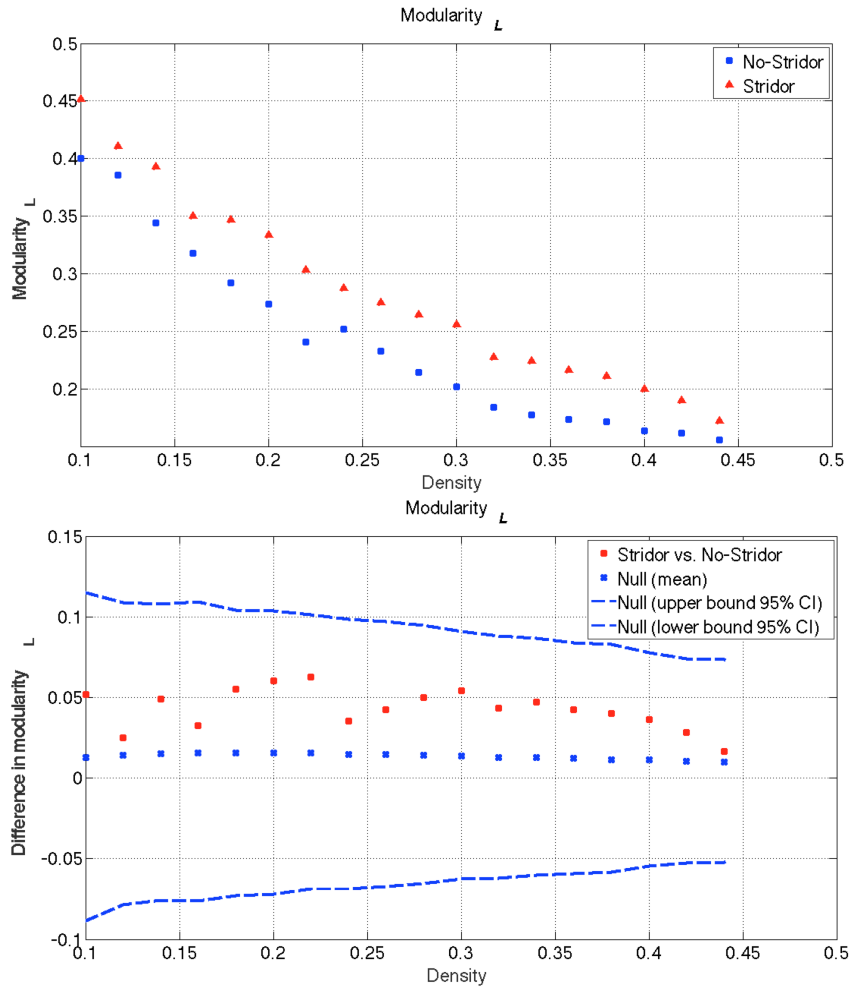


Figure 5.48: Modularity Louvain and difference in Modularity Louvain for No-stridor and Stridor groups

### 5.3.2.3 MSA-C vs MSA-P

In this section the comparison between groups across density for MSA-C vs MSA-P are plotted. No statistically significant differences were found in measures calculated.

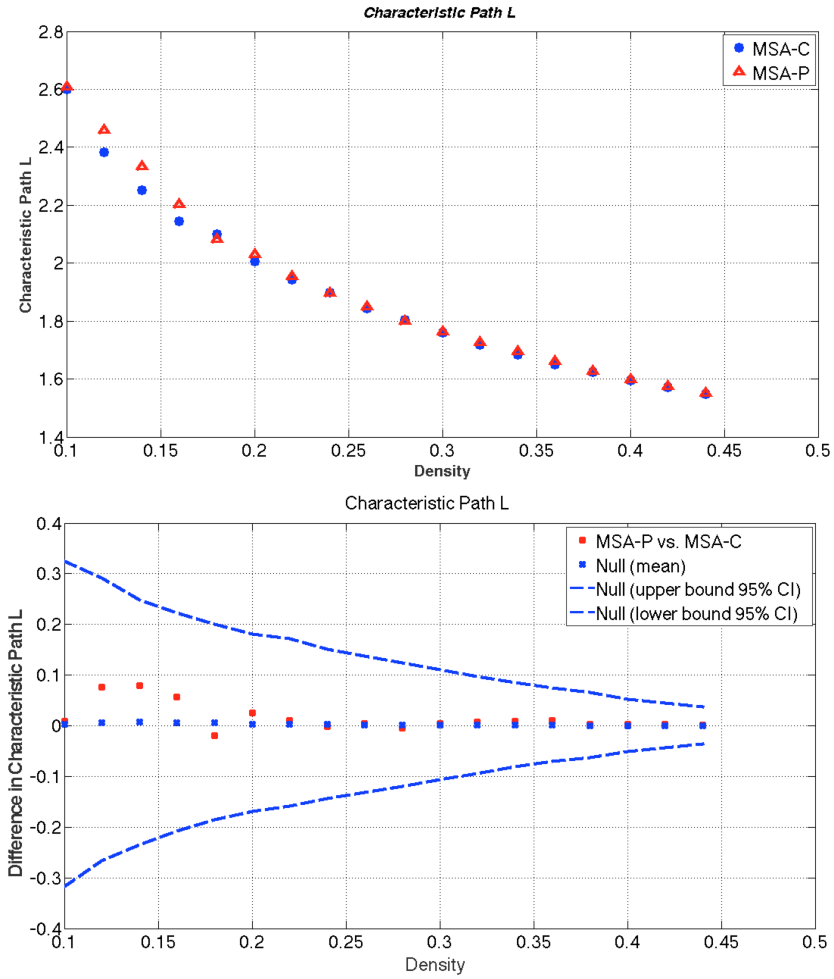


Figure 5.49: Characteristic Path L and difference in Characteristic Path L for MSA-C and MSA-C groups

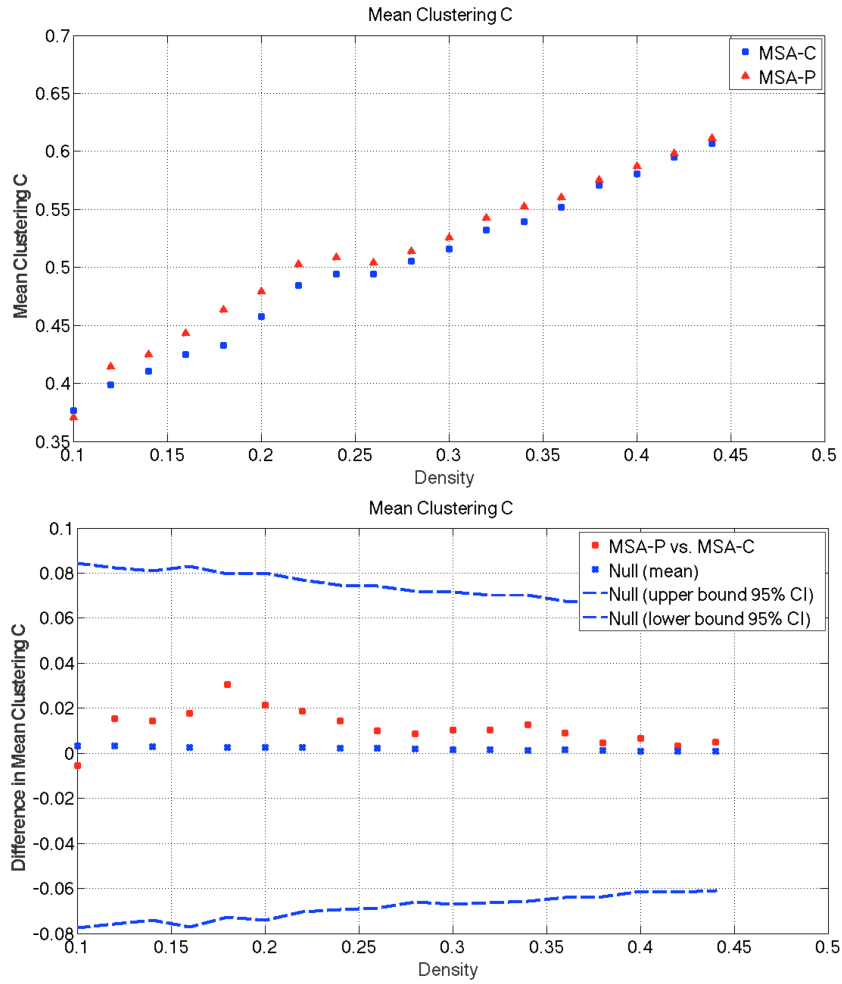


Figure 5.50: Mean Clustering C and difference in Mean Clustering C for MSA-C and MSA-P groups

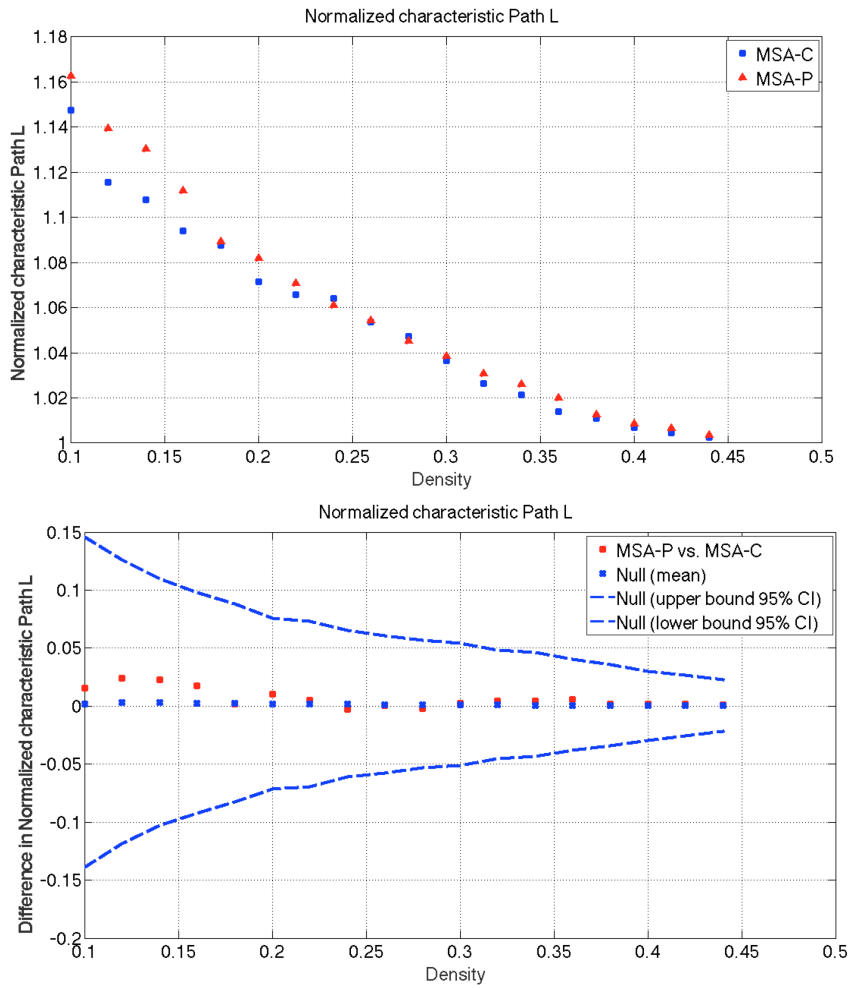


Figure 5.51: Normalized characteristic Path L difference in Normalized characteristic Path L for MSA-C and MSA-P groups

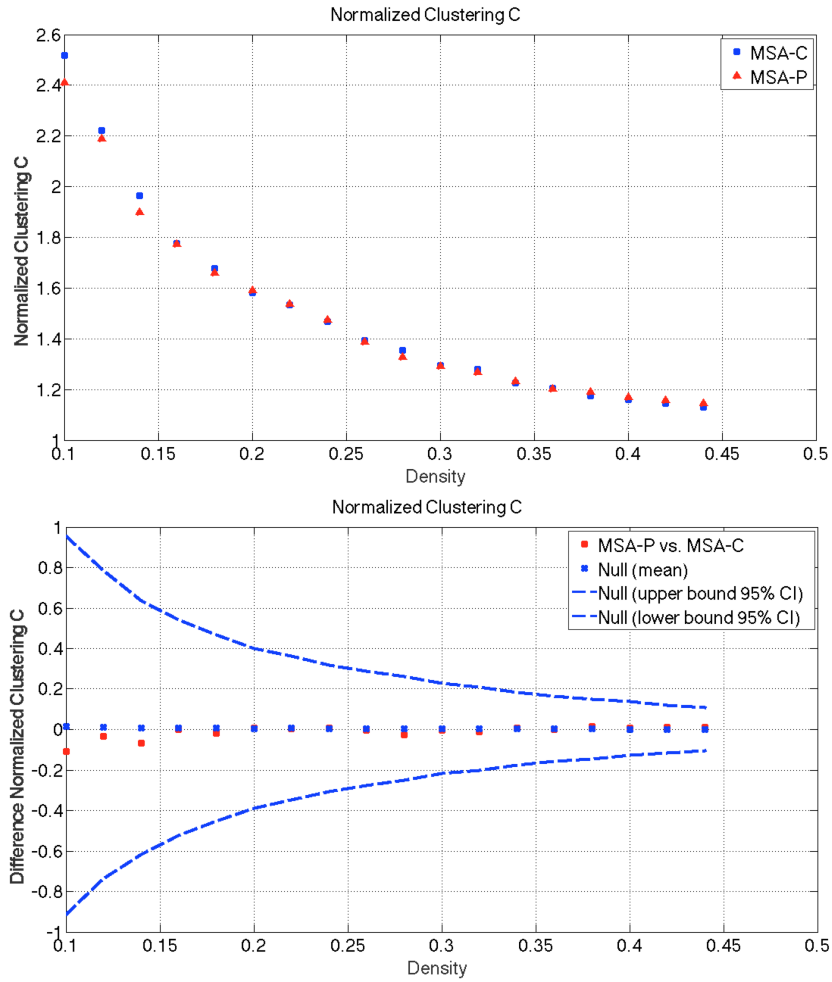


Figure 5.52: Normalized Clustering C and difference in Normalized Clustering C for MSA-C and MSA-P groups

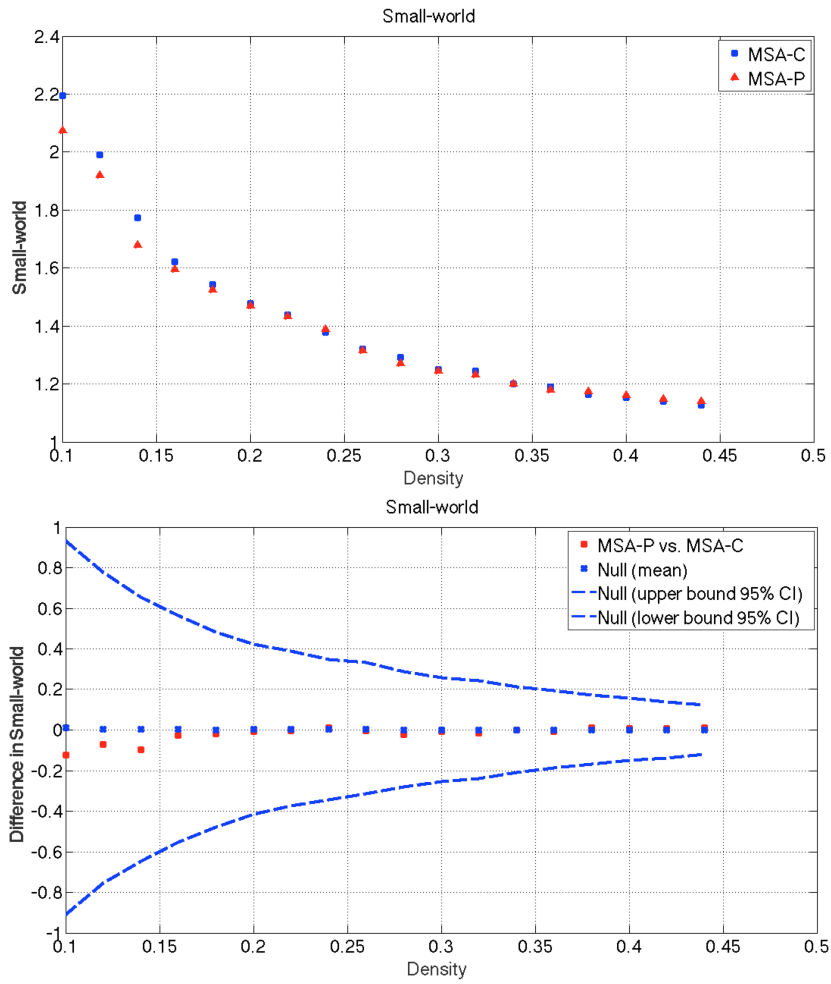


Figure 5.53: Small-world and difference in Small-world for MSA-C and MSA-P groups

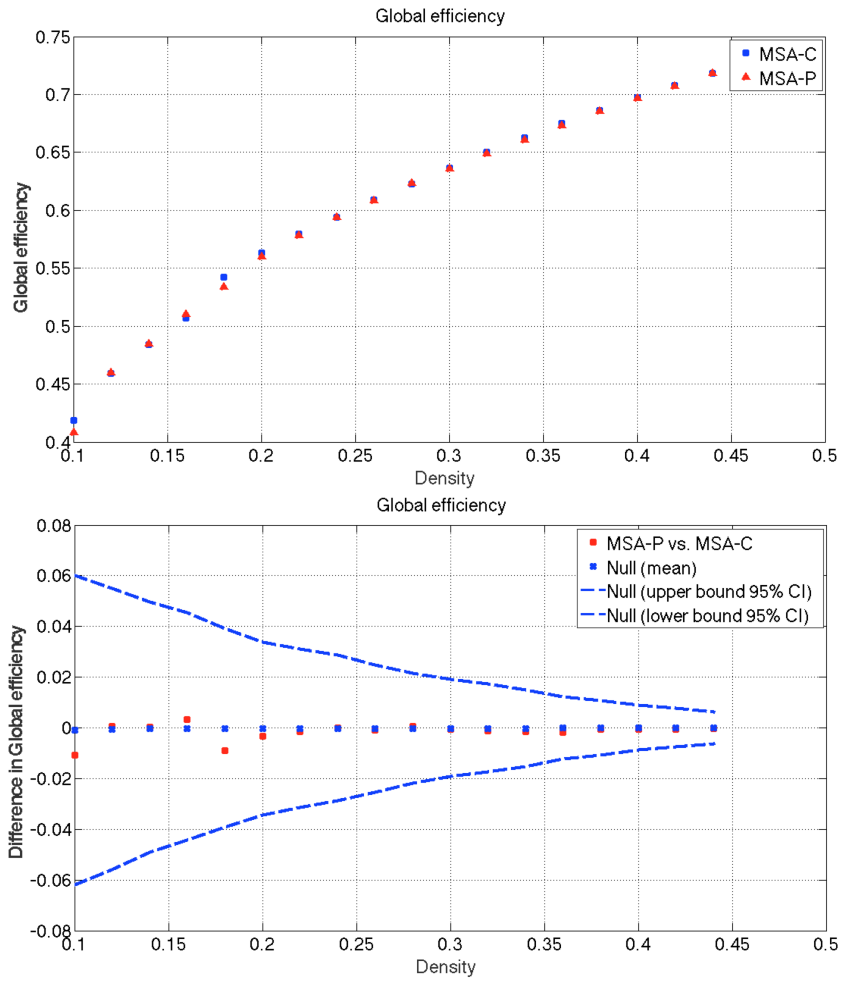


Figure 5.54: Global efficiency and difference in Global efficiency for MSA-C and MSA-P groups

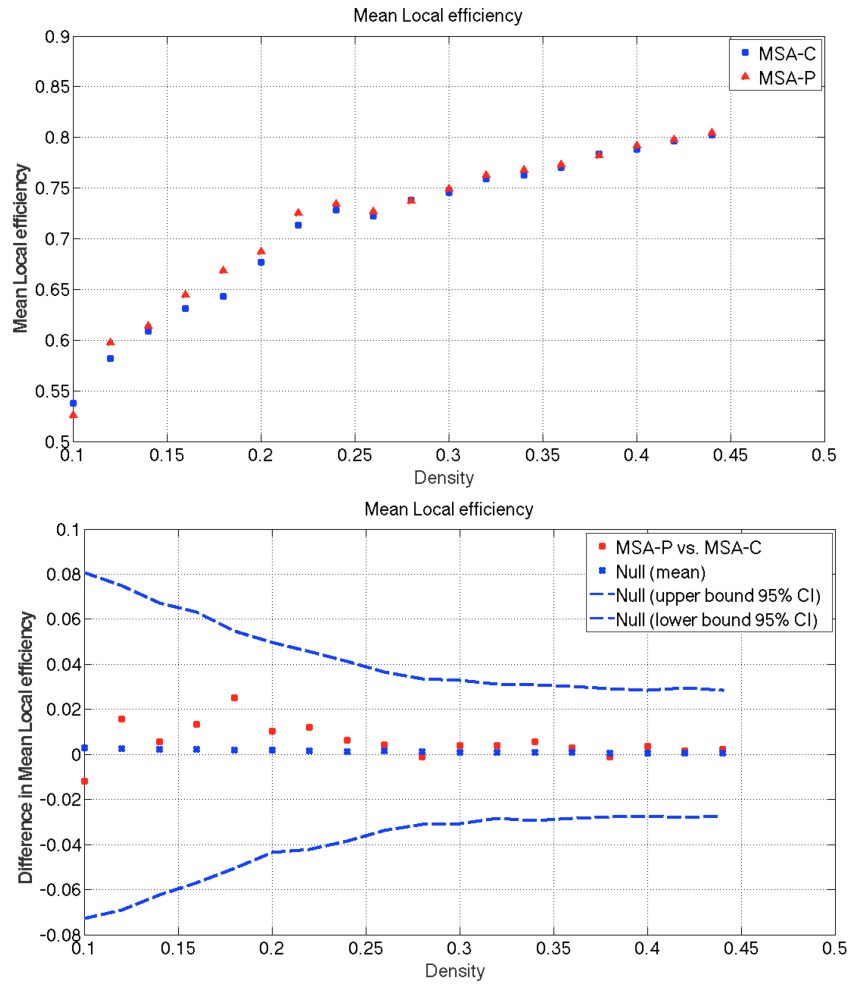


Figure 5.55: Mean Local efficiency and difference in Mean Local efficiency for MSA-C and MSA-P groups

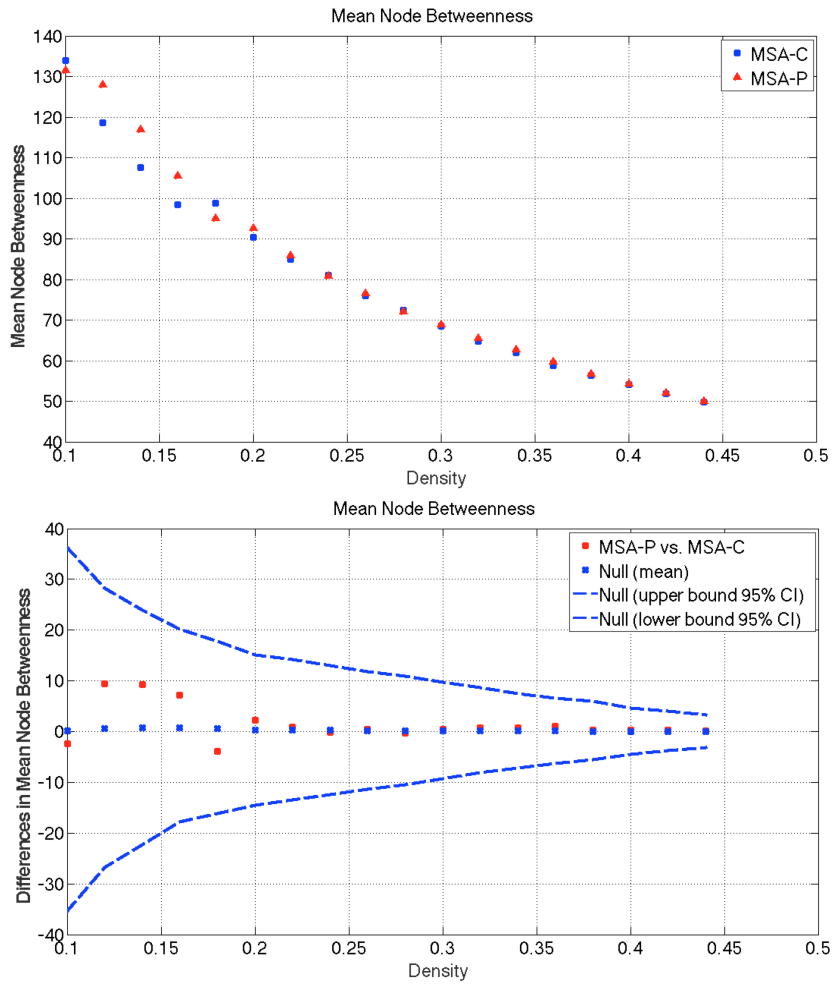


Figure 5.56: Mean Node Betweenness and difference in Mean Node Betweenness for MSA-C and MSA-P groups

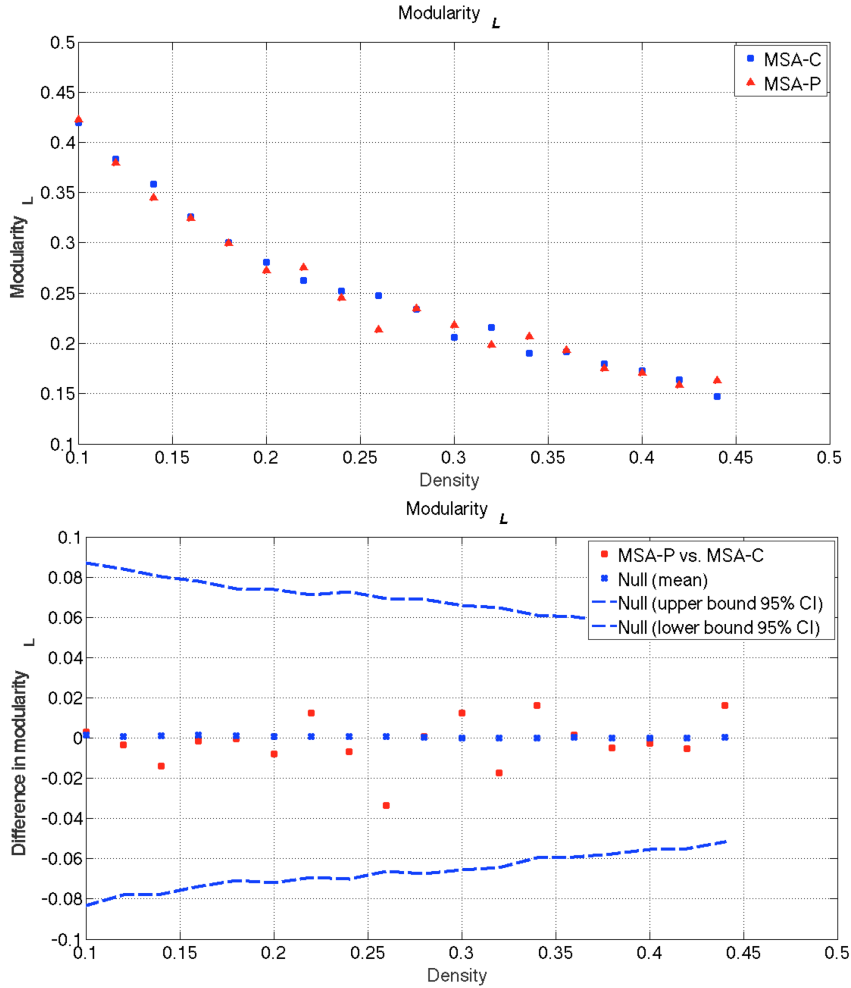


Figure 5.57: Modularity Louvain and difference in Modularity Louvain for MSA-C and MSA-P groups

### 5.3.3 Regional analysis

We investigated between group differences in regional network measures, specifically normalized node betweenness, normalized clustering coefficient and normalized degree distribution on networks thresholded at  $D_{min}$ . All the results for the regional analysis are summarized in Table 5.6.

Regional analysis	HC vs MSA	No-stridor vs Stridor	MSA-C vs MSA-P
Node Betweenness	R-AMY, L-AMY	L-rMF L-MoF R-SM	-
Clustering Coefficient	-	-	-
Node Degree	R-AMY L-AMY R-SM	L-AMY	-

Table 5.6: Results of regional analysis

### 5.3.3.1 Healthy controls vs MSA

Regional network measures of difference in normalized node betweenness between HC and MSA shows significant difference in 2 regions (Figure 5.58): Left-amygdala and Right-amygdala.

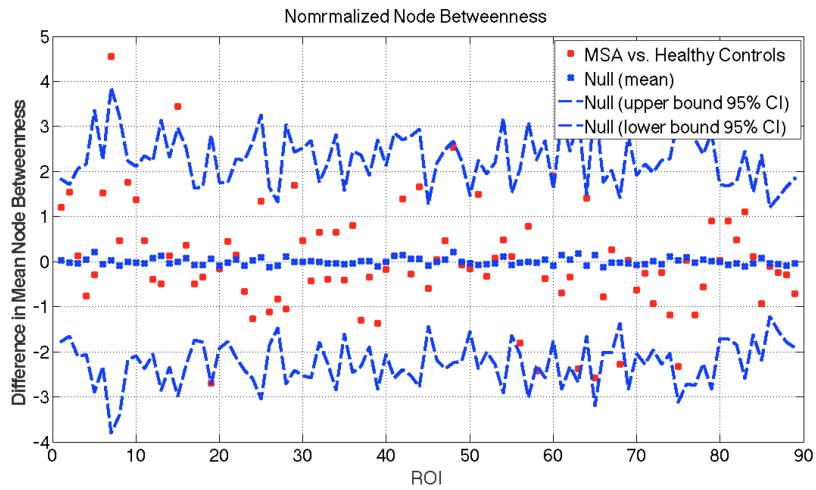


Figure 5.58: Difference in Normalized Node Betweenness for HC vs MSA

Considering the difference in Normalized Clustering C no significant differences were found (Figure 5.59).

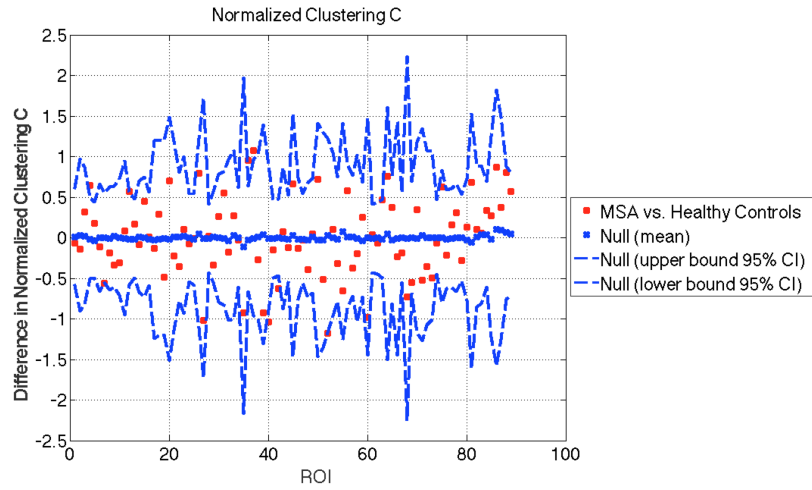


Figure 5.59: Difference in Normalized clustering coefficient for HC vs MSA

Comparisons between difference in Normalized Mean degree show significant differences in Left-amygdala, Right-amygdala and in the Right-supermarginal (Figure 5.60).

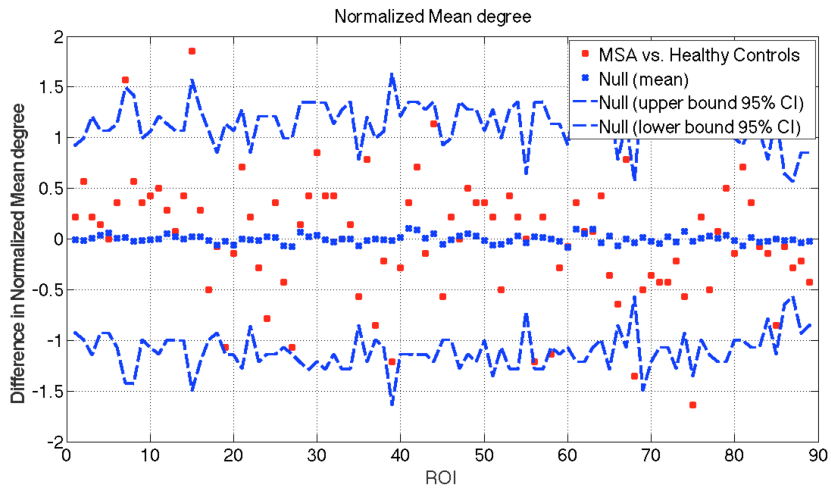


Figure 5.60: Difference in Normalized Mean degree for HC vs MSA

### 5.3.3.2 No-stridor vs Stridor

Regional network measures of difference in normalized Node Betweenness between No-stridor and Stridor show significant difference in 3 regions (Figure 5.61): Left-rostralmiddlefrontal, Left-medial orbitofrontal, Right-supramarginal.

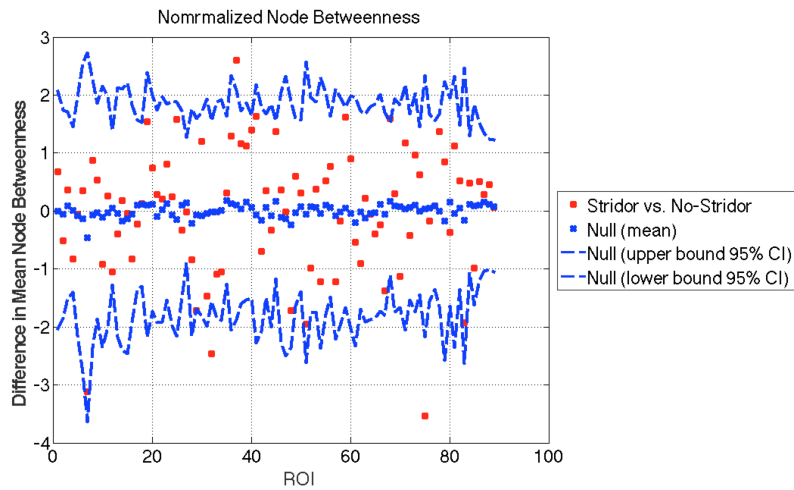


Figure 5.61: Difference in Normalized node betweenness for No-stridor vs Stridor

Considering the difference in normalized clustering coefficient no significant differences were found (Figure 5.62).

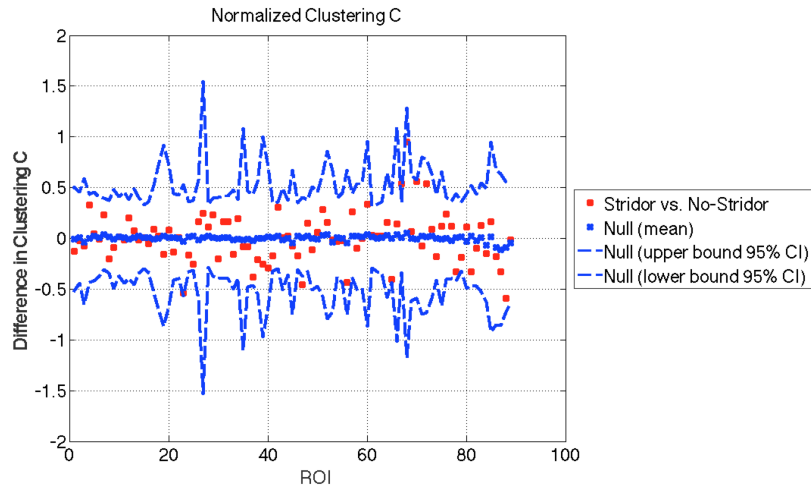


Figure 5.62: Difference in Normalized Clustering C for No-stridor vs Stridor

Comparisons between difference in normalized degree show significant differences only in the Left-amygdala (Figure 5.63).

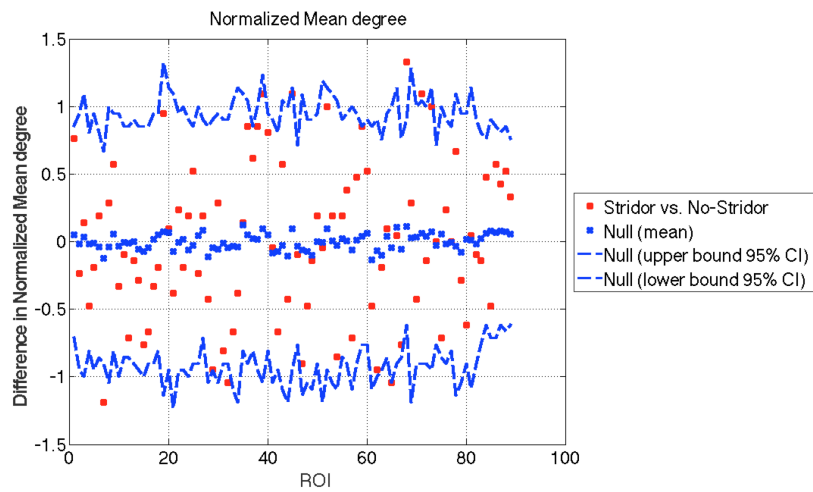


Figure 5.63: Difference in Normalized degree for No-stridor vs Stridor

### 5.3.3.3 MSA-C vs MSA-P

Regional network measures of difference in normalized node betweenness between MSA-C and MSA-P show no significant differences (Figure 5.64).

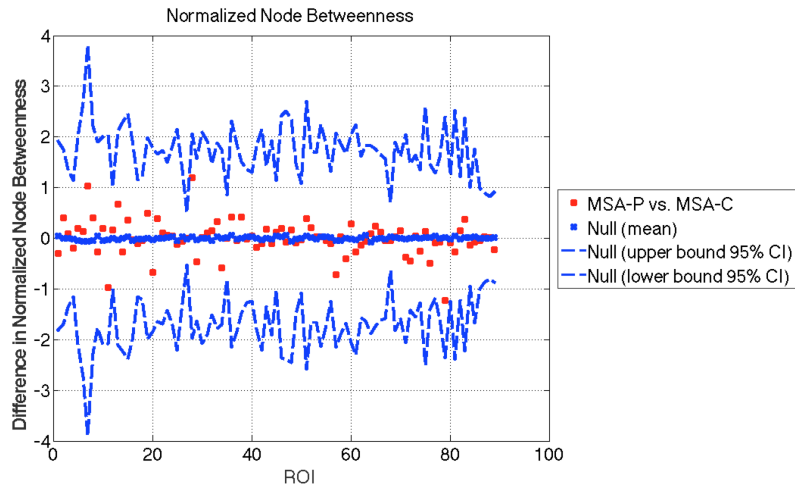


Figure 5.64: Difference in Normalized node betweenness for MSA-C vs MSA-P

Considering the difference in normalized clustering coefficient no significant differences were found (Figure 5.65).

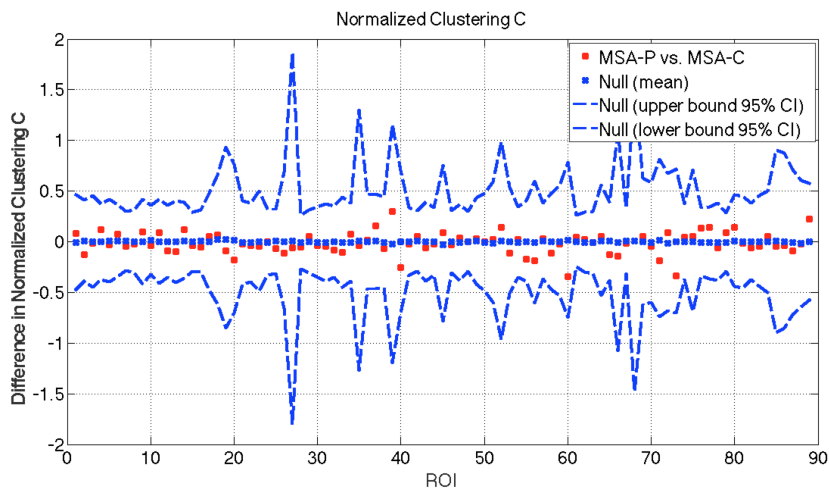


Figure 5.65: Difference in clustering coefficient for MSA-C vs MSA-P

Comparisons between difference in normalized degree shows no significant differences (Figure 5.66).

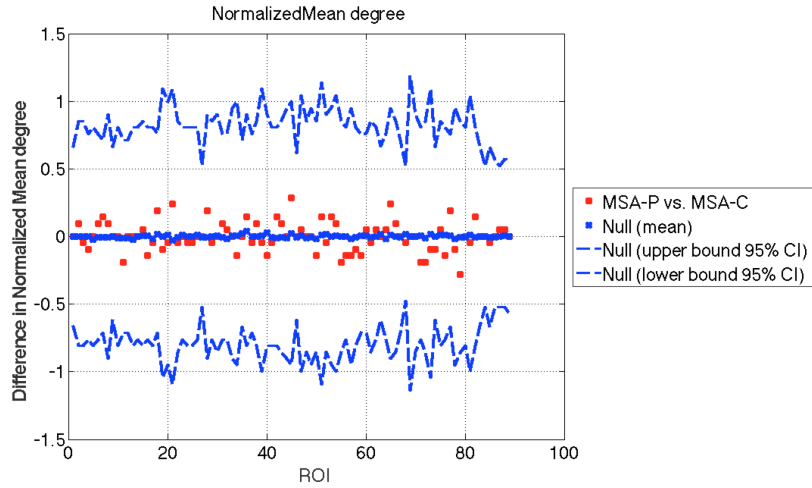


Figure 5.66: Difference in Normalized degree for MSA-C vs MSA-P

### 5.3.4 AUC

In this section the results for the AUC for regional network measure curves between groups are compared. All the result are summarized in Table 5.7.

AUC	HC vs MSA	No-stridor vs Stridor	MSA-C vs MSA-P
Node Betweenness	L-AMY	L-AMY	-
	R-rMF	L-ENTH	
	R-FP	R-SM	
Clustering Coefficient	-	-	-
Node Degree	L-AMY	L-AMY	-
	R-AMY		
	R-FP		
	R-SM		

Table 5.7: Results of AUC analysis

#### 5.3.4.1 Healthy controls vs MSA

AUC analysis of normalized node betweenness between HC and MSA shows significant differences in 3 regions (Figure 5.67): Left-amygdala, Right rostral middle frontal and Right frontal pole.

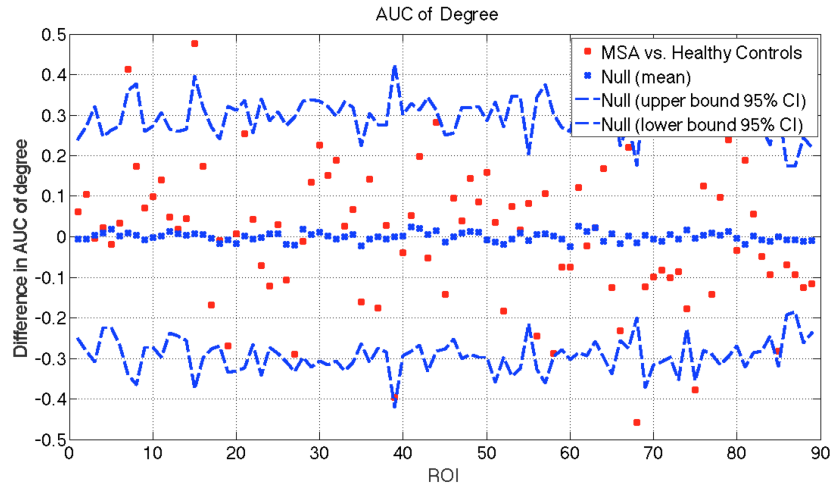


Figure 5.67: Area under the curve (AUC) analysis for HC vs MSA in the regional network properties of normalized betweenness centrality across density

Considering the difference in normalized clustering coefficient performed with AUC analysis, no significant differences between groups were found (Figure 5.68).

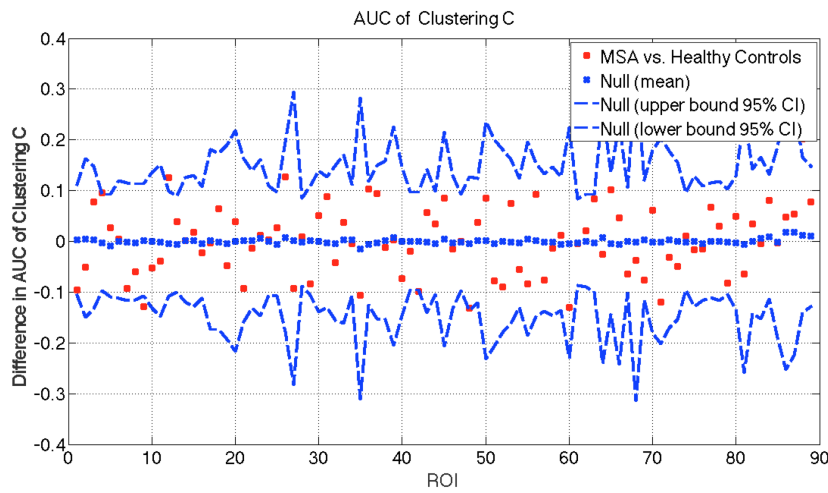


Figure 5.68: AUC analysis for HC vs MSA in the regional network properties of normalized clustering coefficients across density

Comparisons between difference in normalized degree performed with AUC

analysis shows significant differences in four regions (Figure 5.69): Left and Right Amygdala, Right forntal pole and Right supermarginal area.

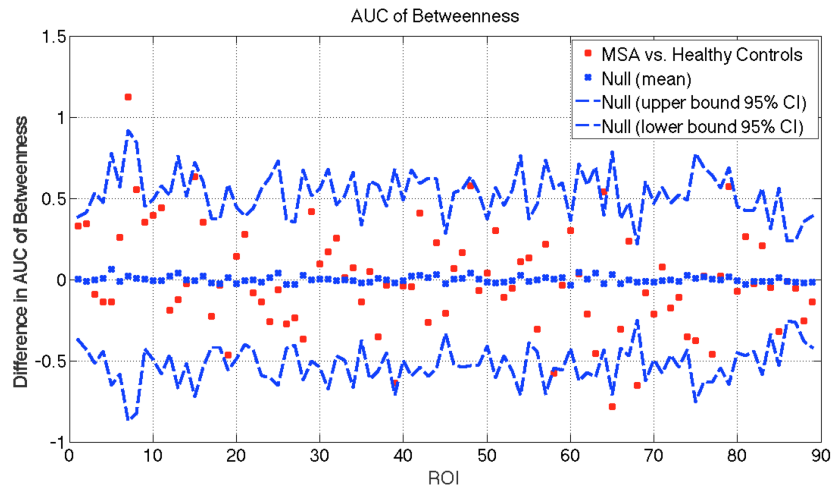


Figure 5.69: AUC analysis of HC vs MSA in the regional network properties of normalized degree across density

#### 5.3.4.2 No-stridor vs Stridor

AUC analysis of normalized node betweenness between No-stridor and Stridor groups shows significant differences in 3 regions (Figure 5.70): Left-amygdala, Left-enthorinal and Right-supramarginal area.

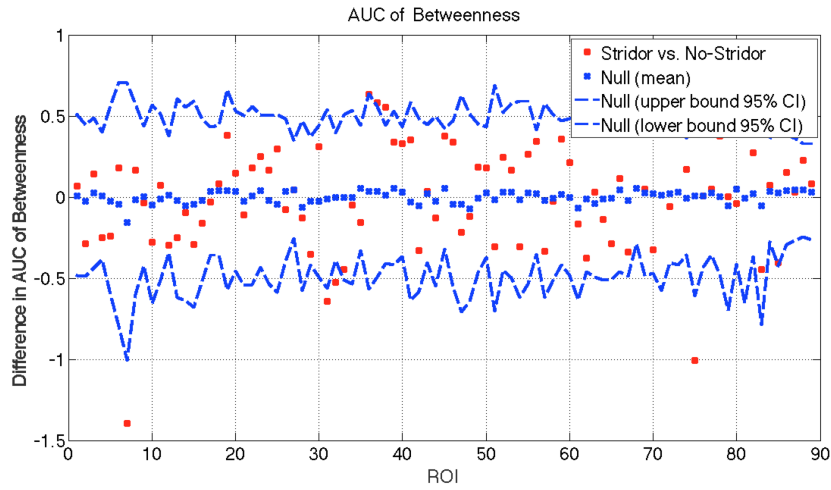


Figure 5.70: AUC analysis for No-stridor vs Stridor in the regional network properties of normalized betweenness centrality across density

Considering the difference in normalized clustering coefficient performed with AUC analysis, no significant differences between groups were found (Figure 5.71).

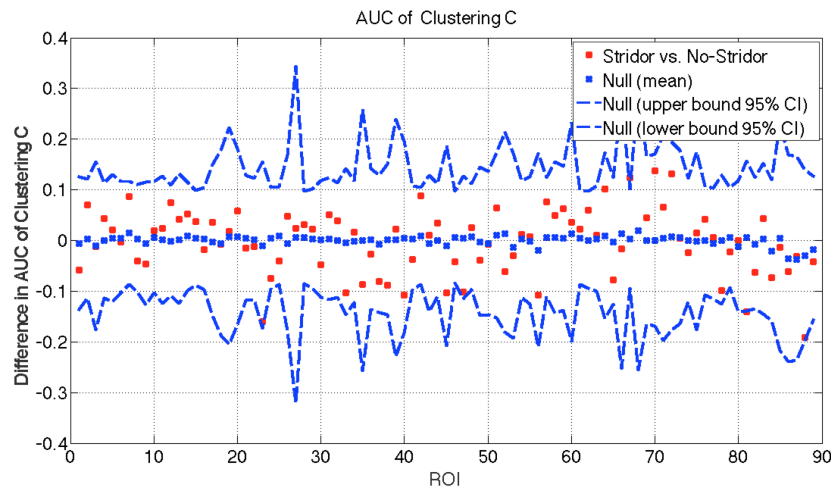


Figure 5.71: AUC analysis for No-stridor vs Stridor in the regional network properties of normalized clustering coefficient across density

Comparison between difference in normalized degree performed with AUC

analysis shows significant differences in only one region (Figure 5.72): Left-amygdala.

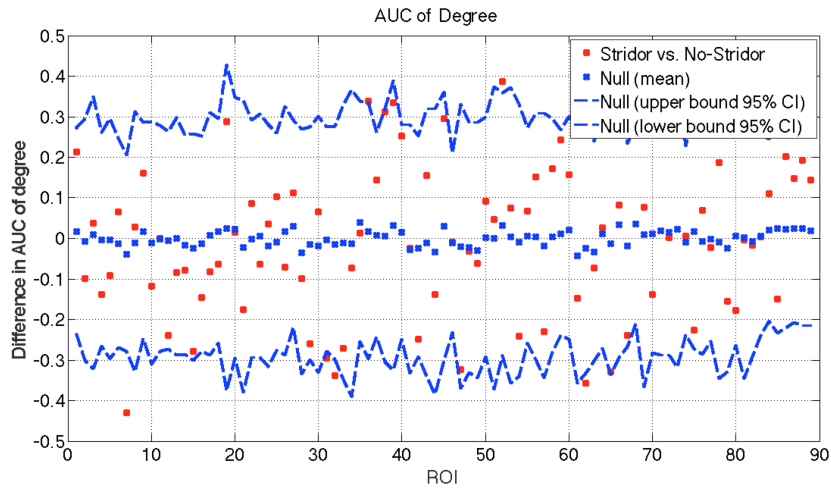


Figure 5.72: AUC analysis for No-stridor vs Stridor in the regional network properties of normalized degree across density

### 5.3.4.3 MSA-C vs MSA-P

AUC analysis of normalized node betweenness between MSA-C and MSA-P shows no significant differences (Figure 5.73).

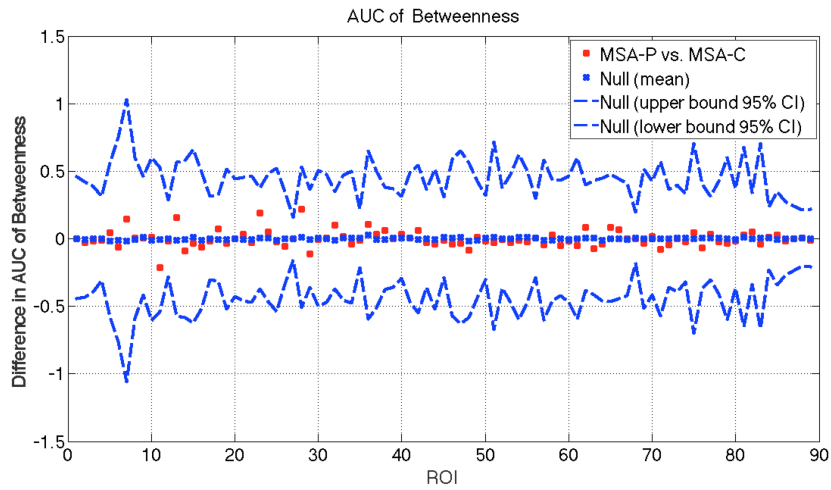


Figure 5.73: AUC analysis for MSA-C vs MSA-P in the regional network properties of normalized betweenness centrality across density

Considering the difference in normalized clustering coefficient performed with AUC analysis, no significant differences between groups were found (Figure 5.74).

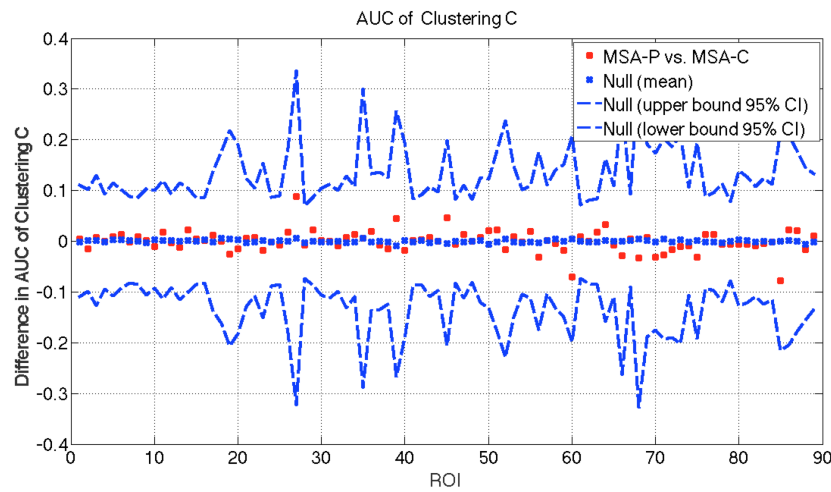


Figure 5.74: AUC analysis for MSA-C vs MSA-P in the regional network properties of normalized clustering coefficient across density

Comparison between difference in normalized degree performed with AUC

analysis shows no significant differences (Figure 5.75).

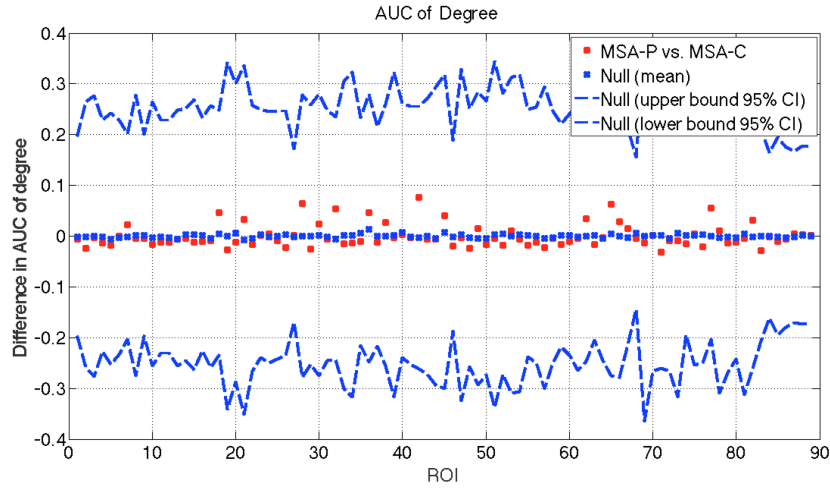


Figure 5.75: AUC analysis for MSA-C vs MSA-P in the regional network properties of normalized degree across density

### 5.3.5 Modularity

In this section the results of modularity analysis are shown.

#### 5.3.5.1 Healthy controls vs MSA

Table 5.8 and Table 5.9 represent how HC network and MSA networks are subdivided respectively in four and five modules.

Modules HC			
Module1	Module2	Module3	Module4
L-CER	L-CAU	L-HIP	L-THA
L-PAL	R-CAU	L-AMY	L-PUT
R-CER	L-parsOP	R-HIP	L-ACC
L-CUN	L-PreCG	R-AMY	R-THA
L-PERIC	R-cMF	L-SP	R-PUT
L-FG	R-PostCG	L-iC	R-ACC
L-FP	R-ENTH	L-TT	L-cAC
L-LOC	R-parsOP	L-cMF	L-rAC
L-PHG	R-PreCG	L-parsTR	L-TP
L-LING	R-PCUN	L-PostCG	L-MT
R-CUN		L-ST	R-rMF
R-PERIC		L-ENTH	R-parsTR
R-LOC		L-IT	R-MT
R-PHG		L-PC	R-rMF
R-LING		L-INS	R-parsOR
MID		L-SM	R-FP
PONS		L-LoF	R-MoF
MED		L-PCUN	R-IP
R-SCP		R-SP	R-SF
L-SCP		R-cAC	
R-MCP		R-iC	
L-MCP		R-TT	
		R-FG	
		R-TP	
		R-ST	
		R-IT	
		R-PC	
		R-ParaC	
		R-INS	
		R-SM	
		R-LoF	

Table 5.8: HC Modules . For abbreviations list refer to Appendix (Table 7.1 and 7.2)

Modules MSA				
Module1	Module2	Module3	Module4	Module5
L-CUN	L-THA	L-SP	L-CAU	L-CER
L-iC	R-THA	L-cAC	L-PUT	R-CER
L-TT	L-parsTR	L-rAC	L-PAL	PONS
L-cMF	L-TT	L-PERIC	L-HIP	R-SCP
L-PostCG	L-ST	L-FG	L-AMY	L-SCP
L-parsOR	L-FP	L-MT	L-ACC	R-MCP
L-PHG	L-ParaC	L-ENTH	R-CAU	LMCP
L-IP	L-parsOP	L-rMF	R-PUT	
L-PreCG	L-LoF	L-IT	R-PAL	
L-SF	R-cAC	L-PC	R-HIP	
R-CUN	R-iC	L-LOC	R-AMY	
R-cMF	R-TT	L-SM	R-ACC	
R-PostCG	R-parsTR	L-LING	L-MoF	
R-ST	R-TP	L-PCUN	L-INS	
R-parsOR	R-INS	R-SP	R-ENTH	
R-FP	MID	R-rAC	R-MoF	
R-PC	MED	R-PERIC	R-LOC	
R-ParaC		R-FG	R-LoF	
R-PHG		R-MT		
R-SM		R-rMF		
R-parsOP.		R-IT		
R-PreCG		R-LING		
R-SF		R-IP		
		R-PCUN		

Table 5.9: MSA Modules

### 5.3.5.2 No-stridor vs Stridor

Table 5.10 and Table 5.11 represent how No-stridor and Stridor networks are subdivided respectively in five and four modules.

Modules No-stridor				
Module1	Module2	Module3	Module4	Module5
L-THA	L-CER	L-CAU	L-iC	R-THA
L-ACC	R-CER	L-PUT	L-cMF	L-SP
R-ACC	L-TP	L-PAL	L-FG	L-cAC
L-CUN	R-TP	L-HIP	L-ST	L-PERIC
L-rAC	R-SM	L-AMY	L-MT	L-PostCG
L-TT	MID	R-CAU	L-ENTH	L-rMF
L-parsTR	PONS	R-PUT	L-IT	L-PC
L-parsOR	MED	R-PAL	L-SM	L-LOC
L-FP	L-SCP	R-HIP	L-SF	L-LING
L-INS	R-SCP	R-AMY	L-PCUN	L-parsOP
L-PreCG	L-MCP	L-MoF	R-rAC	L-IP
R-CUN	R-MCP	L-ParaC	R-FG	R-SP
R-TT		L-PHG	R-PostCG	R-cAC
R-parsTR		L-LoF	R-ST	R-iC
R-parsOR		R-ENTH	R-MT	R-PERIC
R-FP		R-PC	R-rMF	R-cMF
R-INS		R-MoF	R-IT	R-LOC
R-PreCG		R-PHG	R-IP	R-ParaC
R-SF		R-parsOP	R-PCUN	R-LING
		R-LoF		

Table 5.10: No-stridor Modules

Stridor			
Module1	Module2	Module3	Module4
L-ACC	L-THA	L-rAC	L-CER
R-AMY	R-THA	L-cMF	L-CAU
L-SP	L-cAC	L-PostCG	L-PUT
L-CUN	L-ISTH	L-rMF	L-PAL
L-PERIC	L-parsTR	L-PreCG	L-HIP
L-FG	L-TP	R-cMF	L-AMY
L-MT	L-SP	R-rMF	R-CER
L-ENTH	L-parsOP	R-parsOR	R-CAU
L-IT	L-SF	R-PC	R-PUT
L-PC	L-LoF	R-ParaC	R-PAL
L-LOC	R-cAC	R-PreCG	R-HIP
L-ParaC	R-ISTH	R-SF	R-ACC
L-PHG	R-TT		L-TT
L-SM	R-parsTR		L-parsOR
L-LING	R-TP		L-FP
L-IP	R-PostCG		L-MoF
L-PCUN	R-INS		L-INS
R-SP	R-parsOP		R-PERIC
R-CUN			R-ENTH
R-rAC			R-MoF
R-FG			R-LOC
R-ST			L-SM
R-MT			R-LoF
R-IT			MID
R-FP			PONS
R-PHG			MED
R-LING			R-SCP
R-IP			L-SCP
R-PCUN			R-MCP
			L-MCP

Table 5.11: Stridor Modules

### 5.3.5.3 MSA-C vs MSA-P

Table 5.12 and Table 5.13 represent how MSA-C and MSA-P networks are subdivided respectively in five and four modules.

MSA-C				
Module1	Module2	Module3	Module4	Module5
L-THA	L-SP	L-CAU	L-ACC	L-CER
R-THA	L-cAC	L-PUT	L-TT	R-CER
L-CUN	L-rAC	L-PAL	L-cMF	R-ENTH
L-parsTR	L-ISTH	L-HIP	L-PostCG	PONS
L-TP	L-PERIC	L-AMY	L-parsOR	L-MCP
L-ST	L-FG	R-CAU	L-ParaC	R-MCP
L-FP	L-MT	R-PUT	L-IP	L-SCP
L-parsOP	L-ENTH	R-PAL	L-PreCG	R-SCP
L-LoF	L-rMF	R-HIP	L-SF	
R-cAC	L-IT	R-AMY	R-cMF	
R-CUN	L-postCG	R-ACC	R-PostCG	
R-ISTH	L-LOC	L-MoF	R-ST	
R-TT	L-SM	L-PHC	R-parsOR	
R-parsTR	L-LING	L-INS	R-PC	
R-TP	L-PCUN	L-PERIC	R-ParaC	
R-FP	R-SP	R-MoF	R-SM	
R-INS	R-rAC	R-LOC	R-ParsOP	
MID	R-FG	R-PHG	R-PreCG	
MED	R-MT	R-LoF	R-SF	
	R-rMF			
	R-IT			
	R-LING			
	R-IP			
	R-PCUN			

Table 5.12: MSA-C Modules

MSA-P				
Module1	Module2	Module3	Module4	Module5
L-CAU	L-SP	L-THA	L-ACC	L-CER
L-PUT	L-cAC	R-THA	L-CUN	R-CER
L-PAL	L-rAC	L-ISTH	L-cMF	MID
L-HIP	L-PERIC	L-TT	L-PostCG	PONS
L-AMY	L-FG	L-parsTR	L-parsOR	L-SCP
R-CAU	L-MT	L-TP	L-ParaC	R-SCP
R-PUT	L-ENTH	L-ST	L-preCG	L-MCP
R-PAL	L-rMF	L-FP	L-SF	R-MCP
R-HIP	L-IT	L-parsOP	R-CUN	
R-AMY	L-PC	L-LoF	R-cMF	
R-ACC	L-LOC	R-ISTH	R-PostCG	
L-MoF	L-LING	R-TT	R-parsOR	
L-PHG	L-IP	R-parsTR	R-FP	
L-INS	L-PCUN	R-TP	R-PC	
L-SM	R-SP	R-ST	R-ParaC	
R-PERIC	R-cAC	R-INS	R-SM	
R-ENTH	R-rAC	R-parsOP	R-PreCG	
R-MoF	R-FG	MED	R-SF	
R-PHG	R-MT			
R-LoF	R-rMF			
	R-IT			
	R-LOC			
	R-LING			
	R-IP			
	R-PCUN			

Table 5.13: MSA-P Modules

#### 5.3.5.4 Modularity visualization

Four major modules were found for HC, but five for MSA, MSA-C and MSA-P. One module is analogous for the three patient groups: it includes the bilateral cerebellum cortex, and bilateral superior and medial peduncles. We focused on the cortical-subcortical motor network, which includes the bilateral motor and sensorimotor cortex, the paracentral cortex, the basal ganglia and the infratentorial structures. It is segregated in the patient groups, with cortical, subcortical and infratentorial structures belonging to three different modules (Figure 5.77), while this segregation is not observed for HC (Figure 5.76). The segregation of this network was the same for MSA, MSA-C and MSA-P.

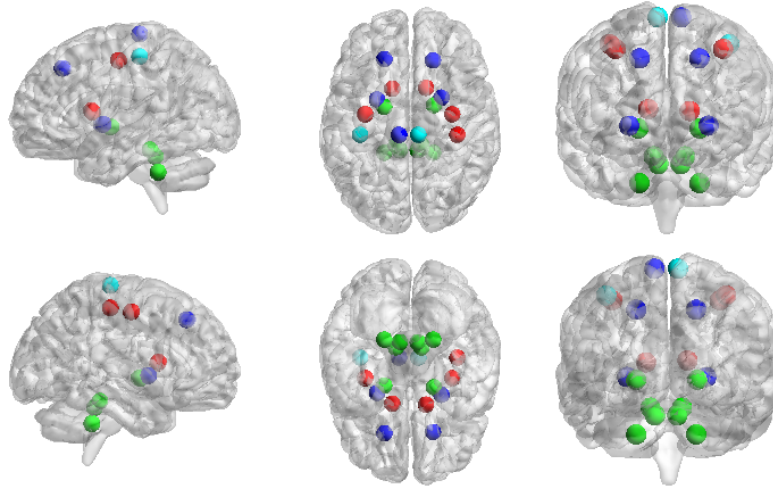


Figure 5.76: HC Modularity of the cortical-subcortical motor network. Different colors belong to different network.

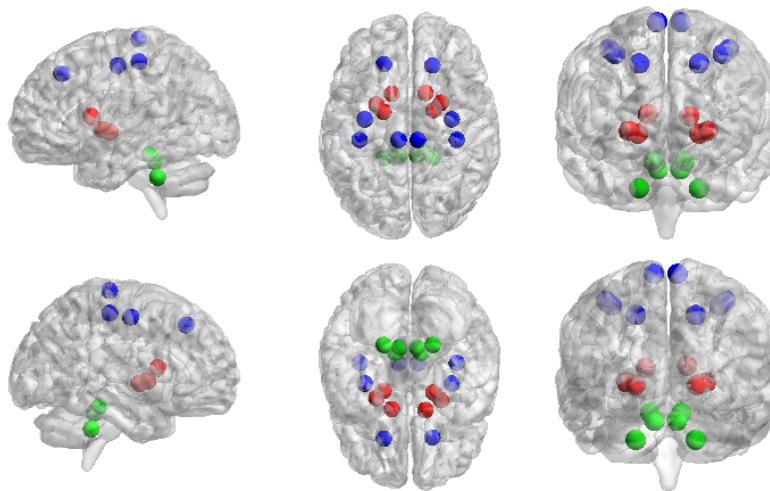


Figure 5.77: MSA Modularity of the cortical sub-cortical motor network. Different colors belong to different networks.

## Chapter 6

# Discussion

In this study, a structural correlation network based on GM volume was constructed for each group: HC, MSA, MSA-C, MSA-P, No-stridor, Stridor respectively. A key part of the thesis was the choice of the ROIs for the construction of the network targeted to the study of MSA patients. For this reason, in addition to the brain regions of the supratentorial area and to the cerebellum cortex, we have chosen to add seven ROIs belonging to the infratentorial area, whose volumes have been estimated by a semi-automatically procedure. To our knowledge, this is the first application of such approach for brain parcelling to be applied to analyze volume covariance. Although the procedure required a manual drafting of infratentorial ROIs, it has been automated by registering them back onto the original 3D space of each individual subject.

In order to construct the network for every group, we evaluated the adjacency matrices based on the Pearson's correlation coefficient. We tried to explore also another kind of comparison between nodes, using the Context Likelihood of Relatedness (CLR) [60]. Using the Pearson's correlation coefficient, as physiologically expected, we found many regions in the right hemisphere that correlated with the corresponding region in the left hemisphere. Using the CLR method we lost this kind of information and this fact suggested us that the use of Pearson's correlation coefficient was the best choice. This is also supported by the fact that many articles concerning brain structural connectivity evaluated the Pearson's correlation coefficient [57] instead of CLR which is mainly used in the study of gene expression.

To quantitatively evaluate any statistical difference between group correlation matrices, successively we performed a Z-statistic, based on Fisher's r-to-z transform. No statistical differences between groups were found likely because of the small sample size.

Moreover, we performed the comparison between groups using graph analysis and calculating several global proprieties across density of the network. No differences were found in: Global Efficiency, Mean Local Efficiency, Path Length, Mean Clustering Coefficient, Small-worldness, between HC vs MSA, No-stridor vs Stridor and MSA-C vs MSA-P. This result suggests that the brain networks

have no alteration in global properties and in the small-world organization.

Regional analysis of Node Betweenness and Node Degree in HC and MSA revealed alterations in the Left-Amygdala and in the Right-Amygdala, regions that belong to the central autonomic network which is known to be impaired in MSA. This alteration could underpin to the altered autonomic and behavioral integration. Moreover differences in regional parameters in some frontal and parietal regions (the Rostral middle frontal area, Supramarginal and Medialorbitofrontal area), as well as in the Amygdala, were evident between MSA patients with and without Stridor. Overall structural and functional alterations in these regions have been demonstrated in patients with other forms of laryngeal dystonia i.e. spasmodic dysphonia [61] which are pathologies characterized by an impairment of the involuntary muscle control in the same area (larynx) affected in the Stridor. No differences were found between MSA-C and MSA-P, probably due to the low sample number.

We found differences in modular organization. Four major modules were found for HC and Stridor while five for MSA, No-stridor, MSA-C and MSA-P. The fifth module was analogous for all patient groups: it included the bilateral cerebellum cortex, the bilateral superior and medial peduncles. Concerning HC modularity, a cortical-subcortical motor network including the bilateral motor and sensorimotor area, the paracentral cortex, the basal ganglia and the infratentorial structure was found to be not segregated as in patient groups.

To summarize, the investigation of modular organization of the different groups, which allowed to explore the network properties that underlie the functionality of complex systems such as brain, has shown a segregation in the cortical-subcortical motor network, in line with the pathophysiology of MSA and it may underpin both the typical parkinsonian and cerebellar features of the disorder.

## Chapter 7

# Conclusions and future directions

In conclusion, in this thesis we investigated the differences in global and regional topological properties and the modular organization of brain networks derived from anatomical covariance of structural MRI between MSA patients (subdivided in the variants MSA-C, MSA-P and patients with and without Stridor) and healthy controls. No differences were found in global and small-worldness measures between MSA and HC or between MSA-C and MSA-P or between No-stridor and Stridor. The study of regional proprieties between HC and MSA reveal alterations in regions that belong to the central autonomic network which is know to be impaired in MSA. This investigation could underpin to the altered autonomic and behavioral integration. The investigation of modular organization between MSA and HC, which reflects differences in properties that underlie the functionality of the brain, has shown a segregation in a cortical-subcortical motor network in patient groups, which may underpin both the typical parkinsonian and cerebellar features of the disorder.

As far as our analysis is concerned, possible future deepening and development could be suggested by the results obtained so far. First of all it could be interesting to investigate more detailed the modular and hierarchically modular organization of these networks.

A module is topologically defined as a subset of highly inter-connected nodes which are relatively sparsely connected to nodes in other modules. In brain networks, topological modules are often made up of anatomically neighboring and/or functionally related cortical regions, and inter-modular connections tend to be relatively long distance. Moreover, brain networks and many other complex systems demonstrate the property of hierarchical modularity, or modularity on several topological scales: within each module there will be a set of sub-modules, and within each sub-module a set of sub-sub-modules, etc. Once an optimally modular partition has been found, it is possible to assign roles to the individual nodes which characterize their significance for intra and inter-

modular transfer of information [62].

There are several general advantages to modular and hierarchically modular network organization, including greater robustness, adaptivity, and evolvability of network function.

It could be interesting to test these proprieties by performing a targeted attack analysis. This technique repetitively removes the network nodes in the order of their importance (betweenness centrality, degree, etc.) and calculates the size of the remaining largest component of the network (or diameter, efficiency, etc, of the remaining network).

Another interesting measure to do could be a random failure analysis. This procedure repetitively removes the network nodes in random order and calculates the size of the remaining largest component of the network. It performs the same procedure on the randomly generated networks to see if the observed between-group difference in robustness to random failure is significant [63].

# Appendix

Brain region	Abbreviation
Accumbens	ACC
Amygdala	AMY
Cerebellum Cortex	CER
Hippocampus	HIP
Pallidum	PAL
Putamen	PUT
Thalamus	THA
Caudalanteriorcingulate	cAC
Caudalmiddlefrontal	cMF
Cuneus	CUN
Entorhinal	ENTH
Frontalpole	FP
Fusiform	FG
Inferioparietal	IP
Insula	INS
Isthmuscingulate	iC
Lateraloccipital	LOC
Lateralorbitofrontal	LoF
Lingual	LING

Table 7.1: Brain region abbreviation legend

Brain region	Abbreviation
Medialorbitofrontal	MoF
Middletemporal	MT
Paracentral	paraC
Parahippocampal	PHG
Parsopercularis	parsOP
Parsorbitalis	parsOR
Parstriangularis	parsTR
Pericalcarine	PERIC
Postcentral	PostCG
Posteriorcingulate	PC
Precentral	PreCG
Precuneus	PCUN
Rostralanteriorcingulate	rAC
Rostralmiddlefrontal	rMF
Superiorfrontal	SF
Superiorparietal	SP
Superiortemporal	ST
Superiomarginal	SM
Temporalpole	TP
Transverse temporal	TT

Table 7.2: Brain region abbreviation legend

# Bibliography

- [1] R.H Hashemi and W.J. Bradley Jr. "MRI the basics". Lippincott Williams & Wilkins, 2004.
- [2] R.G. Henderson. "Nuclear magnetic resonance imaging;a review." Journal of the Royal Society of medicine, 1983.
- [3] N. Bloembergen, E. M. Purcell, and R. V. Pound. "Relaxation Effects in Nuclear Magnetic Resonance Absorption", 1947
- [4] Twieg D "The k-trajectory formulation of the NMR imaging process with applications in analysis and synthesis of imaging methods". Medical Physics, 1983.
- [5] Twieg, D. "Acquisition and accuracy in rapid NMR imaging methods". Magnetic Resonance in Medicine, 1985, 2:437.
- [6] Bruxton RB, Edelman RR, Rosen BR et al. "Contrast in rapid MR imaging: T1- and T2 -weighted imaging." J Comput Assist Tomogr 1987, 11:7.
- [7] Elster AD. "Gradient echo imaging: techniques and acronyms". Radiology 1993, 186:1.
- [8] Blondel VD, Guillaume JL, Lambiotte R, Lefebvre E. "Fast unfolding of communities in large networks". Jorurnal of Statistical Mechanics, 2008.
- [9] Dejerine J, Thomas A. "L'atrophie olivopontocérébelleuse." Nouvelle iconographie de la Salpêtrière 1900, 13:330.
- [10] Bradbury S, Eggleston C. "Postural hypotension: a report of three cases". American Heart Journal 1925, 1:73.
- [11] Shy M, Drager G. "A neurological syndrome associated with orthostatic hypotension: a clinicalpathologic study". Arch Neurol 1960, 2:511.
- [12] Gilman S, Low PA, Quinn N, et al. "Consensus statement on the diagnosis of multiple system atrophy". J Neurol Sci 1999, 163:94.
- [13] Gilman S, Wenning GK, Low PA, et al. "Second consensus statement on the diagnosis of multiple system atrophy". Neurology 2008, 71:670.

- [14] Wenning GK, Geser F, Krismer F, et al. "The natural history of multiple system atrophy: a prospective European cohort study". *Lancet Neurol* 2013, 12:264.
- [15] Tison F, Yekhlef F, Chrysostome V, Sourgen C. "Prevalence of multiple system atrophy". *Lancet* 2000, 355:495.
- [16] Hohler AD, Singh VJ. "Probable hereditary multiple system atrophy-autonomic (MSA-A) in a family in the United States". *J Clin Neurosci* 2012, 19:479.
- [17] Stefanova N, Bücke P, Duerr S, Wenning GK. "Multiple system atrophy: an update". *Lancet Neurol* 2009, 8:1172.
- [18] Köllensperger M, Geser F, Ndayisaba JP, et al. "Presentation, diagnosis, and management of multiple system atrophy in Europe: final analysis of the European multiple system atrophy registry". *Mov Disord* 2010, 25:2604.
- [19] Watanabe H, Saito Y, Terao S, et al. "Progression and prognosis in multiple system atrophy: an analysis of 230 Japanese patients". *Brain* 2002, 125:1070.
- [20] Wenning GK, Colosimo C, Geser F, Poewe W. "Multiple system atrophy". *Lancet Neurol* 2004, 3:93.
- [21] Iranzo A, Santamaría J, Rye DB, et al. "Characteristics of idiopathic REM sleep behavior disorder and that associated with MSA and PD". *Neurology* 2005, 65:247.
- [22] Moreno López C, Santamaría J, Salamero M, et al. "Excessive daytime sleepiness in multiple system atrophy (SLEEMSA study)". *Arch Neurol* 2011, 68:223.
- [23] Kawai Y, Suenaga M, Takeda A, et al. "Cognitive impairments in multiple system atrophy: MSA-C vs MSA-P". *Neurology* 2008, 70:1390.
- [24] Matsuo A, Akiguchi I, Lee GC, et al. "Myelin degeneration in multiple system atrophy detected by unique antibodies". *Am J Pathol* 1998, 153:735.
- [25] Benarroch EE. "Brainstem in multiple system atrophy: clinicopathological correlations". *Cell Mol Neurobiol* 2003, 23:519.
- [26] Massano J, Costa F, Nadais G. "Teaching neuroImage: MRI in multiple system atrophy: hot cross bun sign and hyperintense rim bordering the putamina". *Neurology* 2008, 71:e38.
- [27] Brooks DJ, Seppi K. "Neuroimaging Working Group on MSA. Proposed neuroimaging criteria for the diagnosis of multiple system atrophy". *Mov Disord* 2009, 24:949.

- [28] Gilman S, Wenning GK, Low PA, et al. "Second consensus statement on the diagnosis of multiple system atrophy". *Neurology* 2008, 71:670.
- [29] Harary, Frank. "Graph Theory". Reading, MA: Addison-Wesley, 1968.
- [30] Ed Bullmore and Olaf Sporns "Complex brain networks: graph theoretical analysis of structural and functional systems" *Nature* 2009, 10:186.
- [31] M. Rubinov and O. Sporns. "Complex network measures of brain connectivity: Uses and interpretations". *NeuroImage* 2010, 52:1059.
- [32] E.T. Bullmore and D.S. Bassett. "Brain Graphs: Graphical Models of the Human Brain Connectome". *Annu. Rev. Clin. Psychol.* 2011, 7:113.
- [33] Stanley, Matthew L. et al. "Defining Nodes in Complex Brain Networks." *Frontiers in Computational Neuroscience* 2013, 7:169.
- [34] Honey C, J. Sporns, O. Cammoun, et al. "Predicting human resting-state functional connectivity from structural connectivity". *PNAS* 2009, 106:2035.
- [35] Le Bihan, D. Johansen-Berg, "Diffusion MRI at 25: exploring brain tissue structure and function". *NeuroImage* 2012, 61:324.
- [36] J. Wang, L. Wang, Y. Zang, et al "Parcellation-dependent small-world brain functional networks: a resting-state fMRI study" *Human Brain Mapping* 2009, 30:1511.
- [37] Stanley, Matthew L. et al. "Defining Nodes in Complex Brain Networks." *Frontiers in Computational Neuroscience* 2013, 7:169.
- [38] Matthew L. Stanley, Malaak N. Moussa, Brielle M. Paolini et al. "Defining nodes in complex brain networks". *Front Comput Neurosci* 2013, 7:169.
- [39] Bernhardt BC, Chen Z, He Y, Evans AC, Bernasconi N. "Graph-theoretical analysis reveals disrupted small-world organization of cortical thickness correlation networks in temporal lobe epilepsy". *Cereb Cortex* 2011, 21:2147.
- [40] Albert-Laszl Barabasi, Reka Albert, Hawoong Jeong. "Mean-eld theory for scale-free random networks". *Physica* 1999, 272:173.
- [41] Bowman TJ. "Review of Sleep Medicine". Boston: Butterworth Heinemann 2003.
- [42] [www.freesurfer.net/fswiki](http://www.freesurfer.net/fswiki)
- [43] <https://fsl.fmrib.ox.ac.uk/fsl/fslwiki/Atlases>
- [44] <http://fsl.fmrib.ox.ac.uk/fsl/fslwiki/>
- [45] <https://www.gimp.org/>

- [46] M. Battaglini, M. Jenkinson, and N. De Stefano. "Evaluating and reducing the impact of white matter lesions on brain volume measurements". *Human Brain Mapping* 2012, 33:2062.
- [47] Valverde S, Oliver A et al. "A white matter lesion-filling approach to improve brain tissue volume measurements" *Neuroimage Clin* 2014, 6:86.
- [48] Matthew L. Stanley, Malaak N. Moussa, Brielle M. Paolini et al. "Defining nodes in complex brain networks". *Front Comput Neurosci* 2013, 7:1692013.
- [49] <http://www.jmp.com/>
- [50] Benjamini, Yoav, Hochberg, Yosef. "Controlling the false discovery rate: a practical and powerful approach to multiple testing". *Journal of the Royal Statistical Society* 1995, 55:289.
- [51] Kaiser M, Hilgetag CC. "Nonoptimal component placement, but short processing paths, due to long-distance projections in neural systems". *PLoS Comput Biol*, 2006 2:95.
- [52] <http://brain-connectivity-toolbox.net>
- [53] Blondel VD, Guillaume JL, Lambiotte R, Lefebvre E. "Fast unfolding of communities in large networks". *Jorurnal of Statistical Mechanics*, 2008.
- [54] Paolo Baldi, "Calcolo delle probabilità e statistica". Milano, McGraw-Hill, 1998.
- [55] Fisher, R. A. "Frequency distribution of the values of the correlation coefficient in samples of an indefinitely large population". *Biometrika* 1915, vol 10, 4:507.
- [56] He Y, Chen Z, Evans A. "Structural insights into aberrant topological patterns of large-scale cortical networks in Alzheimer's disease". *J Neurosci* 2008, 28: 4756.
- [57] Yun-gang Luo, Defeng Wang et al. "Brain Structure Network Analysis in Patients with Obstructive Sleep Apnea" *PlosOne* 2015, 10:1371.
- [58] Hosseini, S.M.H., Hoefft, F., Kesler, S.R. "GAT: a graph-theoretical analysis toolbox for analyzing between-group differences in large-scale structural and functional brain networks". *PlosOne* 2012, 7:40709.
- [59] <http://www.nitrc.org/projects/bnv/>
- [60] Jeremiah J. Faith, Boris Hayete, "Large-Scale Mapping and Validation of Escherichia coli Transcriptional Regulation from a Compendium of Expression Profiles". *Plos Biology* 2007, 10:1371.
- [61] Benarroch EE. "The central autonomic network: functional organization, dysfunction, and perspective". *Mayo Clin Proc.* 1993, 68:988.

- [62] Guimerà R., Amaral L. “Functional cartography of complex metabolic networks”. *Nature* 2005, 433:895.
- [63] David Meunier, Renaud Lambiotte and Edward T. Bullmore “Modular and Hierarchically Modular Organization of Brain Networks” *Front Neurosci*, 2010 4: 200.

## Ringraziamenti

Innanzitutto desidero ringraziare la mia relatrice, la Dott.ssa Claudia Testa, lavorare con lei è stata un'esperienza molto piacevole ed interessante. Mi ha sempre seguito in tutto quello che facevo, aiutandomi, dandomi consigli e spiegandomi tutto ciò che non capivo. Mi è stata vicina in tutti i mesi della tesi e si è mostrata senza dubbio una persona dalle doti professionali ed umane fuori dal comune. Ringrazio la Prof.essa Paola Fantazzini e il Prof. Daniel Remondini per i preziosi consigli che mi hanno dato durante l'impostazione del lavoro. Voglio ringraziare anche tutti membri del DIBINEM: il direttore Raffaele Lodi, Caterina Tonon, David Neil Manners, Claudio Bianchini, Stefania Evangelisti, Lorenzo Cirignotta. Un gruppo stupendo che ha saputo stimolarmi tantissimo. Un grazie particolare va al dott. Stefano Zanigni che mi insegnato molto e mi ha accompagnato durante tutto il lavoro. Grazie Alice e Elisabetta, fedelissime compagne per i pranzi al S.Orsola. Grazie a Lia per l'aiuto quotidiano, gli sfoghi, le risate e tutti i momenti passati assieme. Sei stata una compagna fin dall'inizio e sei diventata, con il passare del tempo, una amica vera.

Il ringraziamento più grande lo voglio fare ai miei genitori, a cui dedico questo lavoro. Con questa tesi concludo il mio percorso di studio universitario che non sarebbe stato possibile senza il loro enorme supporto e aiuto. Fin da quando ero bambino mi hanno insegnato ad essere curioso e ad amare tutto ciò che mi sta intorno, mi hanno supportato in ogni mia decisione e hanno sempre creduto in me. Non avrei potuto chiedere di più dalla mia famiglia. Sono felice della persona che sono diventato e questo dipende principalmente da loro, quindi grazie di cuore veramente.

Grazie a tutti i miei amici. Canna e Gazzo che considero come fratelli, Elia e Manu gli amici di sempre, Tommy, MissFano e Tibo per quanto mi sono sempre vicini. Grazie a tutti i compagni di Fisica in particolare Cata e Zan perché sono amici veri, che mi mancano molto. Grazie alla Crew per tutti i momenti bellissimi passati in moto e le risate. Grazie ai ragazzi dello Spingitondo, perché senza le nostre partite sarebbero stati troppo lunghi questi anni. Grazie a tutta la 5a C del Cope, ai Mariani e ai Bolliti per le mille serate passate assieme. Ringrazio poi tutte le persone che non ho nominato esplicitamente ma che hanno avuto un ruolo, anche piccolo, nella mia vita. I ricordi di tutti voi li porterò sempre con me.

Infine, le ultime parole di ringraziamento le voglio dedicare alla mia ragazza Jlenia. La sua vicinanza mi ha aiutato a superare i momenti più difficili e mi ha stimolato a raggiungere i miei obiettivi. Sono veramente molto fortunato ad avere una persona così bella al mio fianco e non vedo l'ora di vivere ancora tantissimi momenti stupendi assieme.

Grazie.